A Study of Spiral Structure and Lopsidedness in LEGUS Disk Galaxies

Faiezeh Shabani

Dissertation
submitted to the
Combined Faculties of the Natural Sciences and Mathematics
of the Ruperto-Carola-University of Heidelberg. Germany
for the degree of
Doctor of Natural Sciences

Put forward by
Faiezeh Shabani
born in: Khodabandeh, Zanjan (Iran)
Oral examination: 12 November 2019

A Study of Spiral Structure and Lopsidedness in LEGUS Disk Galaxies

Referees: Prof. Dr. Eva K. Grebel

Priv. Doz. Dr. Sabine Reffert

Abstract

We present a detailed study of spiral structure and lopsidedness in four LEGUS disk galaxies. We first search for a possible age gradient of star clusters across the spiral arms, as predicted by the spiral density wave theory. We find a clear age sequence across the grand-design arms of NGC 1566, indicating that the density wave theory is the primary mechanism for the formation of spiral arms in this galaxy. In contrast, we find no offset in the location of star clusters with different ages in M51a and NGC 628, suggesting that tidal interactions and swing amplification theory might be the dominant scenarios to generate spiral patterns in these galaxies, respectively.

Later, we search for a link between the asymmetric distribution of the star clusters along the spiral arms and the physical properties of NGC 3344, NGC 1566, NGC 628, and M51a. For this purpose, we construct 2D spatially resolved stellar mass and SFR surface density maps of the galaxies applying a pixel-by-pixel spectral energy distribution fitting technique. We do not observe any lopsidedness in the distribution of stellar mass surface density of the two arms in our target galaxies. On the contrary, our derived resolved SFR surface density maps of NGC 3344, NGC 1566, and the inner regions of M51a confirm the presence of lopsidedness between the two arms in a similar fashion to the distribution of the young star clusters. In the case of NGC 628, we do not observe any correlation between the lopsidedness in the distribution of star clusters and its SFR surface density.

Zusammenfassung

Wir stellen eine detaillierte Studie der Spiralstruktur und Schlagseite von vier LEGUS Scheibengalaxien vor. Zunächst suchen wir nach einem möglichen, von der Dichtewellentheorie für Spiralgalaxien vorhergesagten Altersgradienten von Sternhaufen über die Spiralarme. Wir finden eine klare Altersse-quenz über die Grand-Design-Arme von NGC 1566, was darauf hindeutet, dass die Dichtewellentheorie der primäre Mechanismus für die Ausbildung von Spiralarmen in dieser Galaxie ist. Hingegen finden wir keinen Versatz in der Position von Sternhaufen unterschiedlichen Alters in M51a und NGC 628. Dies weist auf Gezeitenwechselwirkungen und Schwingverstärkungstheorie als dominierende Szenarien zur Erzeugung von Spiralstrukturen in diesen Galaxien hin.

Später suchen wir nach einer Verbindung zwischen der asymmetrischen Verteilung von Sternhaufen entlang der Spiralarme und der physikalischen Eigenschaften von NGC 3344, NGC 1566, NGC 628 und M51a. Zu diesem Zweck konstruieren wir zweidimensionale, räumlich aufgelöste Sternmassen- und SFR-Flächendichtekarten der Galaxien, indem wir Pixel für Pixel eine Technik anwenden, die die spektrale Energieverteilung anpasst. Wir beobachten keinerlei Schlagseite in der Verteilung der Sternmassenflächendichte der beiden Arme unserer Galaxien. Im Gegensatz dazu bestätigen unsere aufgelösten SFR-Flächendichtekarten von NGC 3344, NGC 1566 sowie der inneren Regionen von M51a das Vorhandensein einer Schlagseite zwischen den beiden Armen in einer ähnlichen Art und Weise wie in der Verteilung der jungen Sternhaufen. Im Fall von NGC 628 beobachten wir keine Korrelation zwischen der Schlagseite in der Verteilung von Sternhaufen und der SFR-Flächendichte.

To my parents

for all your sacrifices to give me the life I love today

To Zdeněk

for your endless support and encouragement

And to my teachers

without you, none of my success would have been possible

Contents

List of figures

List of tables

1

Introduction

In this thesis, I study the spiral structures in four nearby spiral galaxies selected from the Legacy ExtraGalactic UV Survey (LEGUS, GO–13364, PI: D. Calzetti)[1] observations. The work presented in this thesis can be divided into two main projects. In the first project (Chapter 2 and Shabani et al. 2018), I use the young star clusters as a tool to investigate whether the observed spiral patterns in three galaxies, NGC 1566, NGC 628, and M51a, are produced through the mechanism described by the spiral density wave theory. The second project (Chapter 3 and Chapter 4, Shabani et al. 2019), focuses on finding a correlation between the observed asymmetric distribution of star clusters in the primary spiral arms of four spiral galaxies, NGC 3344, NGC 1566, NGC 628, and M51a, with the physical properties of the galaxies such as star formation rate (SFR) and stellar mass surface density on sub-kpc scales.

The structure of this chapter follows the main division. After a general introduction on galaxy classification, I will give an overview of the theories of the formation and evolution of spiral patterns in disk galaxies (Section 1.2), to provide the reader with a general understanding of its main scenarios. Subsequently, in Section 1.3, I introduce lopsided galaxies, mainly focusing on the possible mechanisms to generate lopsidedness in galaxies. Finally, in Section 1.4, I present the LEGUS survey, aiming mostly at describing the physical properties of the young star clusters that we use in this work.

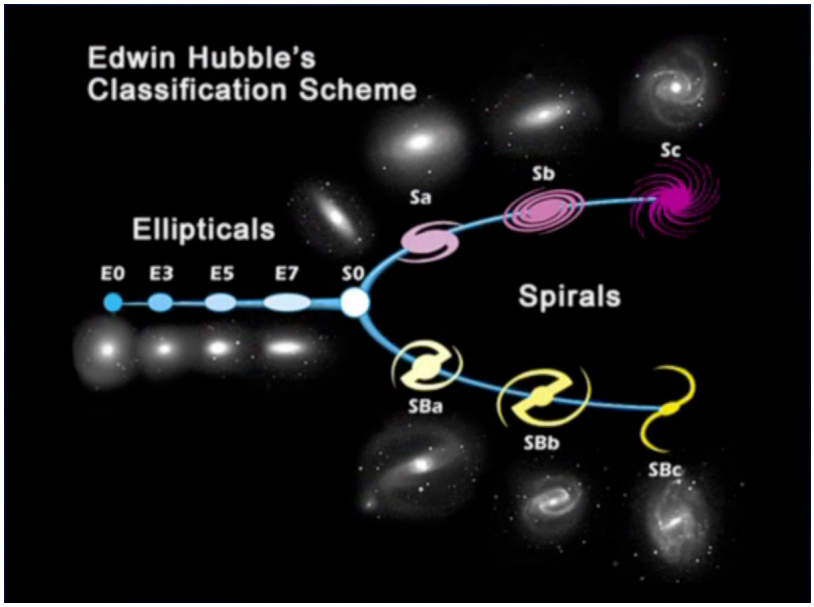

Figure 1.1.1: The Hubble's tunning fork classification scheme. Image credit: http://www.spacetelescope.org/

1.1 Classification of Spiral Galaxies

In the observable universe, galaxies appear in different shapes and sizes in various stages of their evolution. Since the first evidence that galaxies or *nebulae* lie outside the Milky Way (Hubble 1926), astronomers began to categorize galaxies into several classes based on their shape, morphology, and structure. Pioneers like Edwin Hubble and Gérard de Vaucouleurs outlined the scheme of galaxy classification as it is known today. A morphological classifications of galaxies based on their optical appearance was done by Hubble (1926). The Hubble Sequence (Fig. 1.1.1) divides galaxies into three categories, i.e., ellipticals (Es), spirals (Ss), and irregulars (Irrs). Elliptical galaxies are located on the left side of the Hubble scheme and are categorized based on their apparent ellipticity. The apparent ellipticity of an elliptical galaxy is defined as $\epsilon = 1 - b/a$, where a and b stand for the major and minor apparent axis, respectively. Elliptical galaxies with an apparent ellipticity of ϵ are called as "En", where $n = 10\epsilon$. For instance, ellipticals with $\epsilon = 0.5$ are labeled as E5. Elliptical galaxies with $\epsilon > 0.7$ (E7) are not known (Carroll and Ostlie 2006). Spiral galaxies are divided into two types based on the presence of a bar, S and SB for normal unbarred and barred galaxies (top and bottom fork of the diagram, respectively). Further, spirals are classified according to the degree of winding of spiral arms and bulge-to-disk luminosity ratio from Sa to Sd or SBa to SBd. The "a" notation stands for the most tightly wound arms while the "d" label corresponds the most open arms. As moving toward the "d" classification in the sequence, the bulge-to-disk luminosity ratio decreases. Lenticulars or S0 galaxies, a transition between the elliptical and spiral galaxies, are lens-shaped disk galaxies with no obvious spiral structures.

[1] https://archive.stsci.edu/prepds/legus/

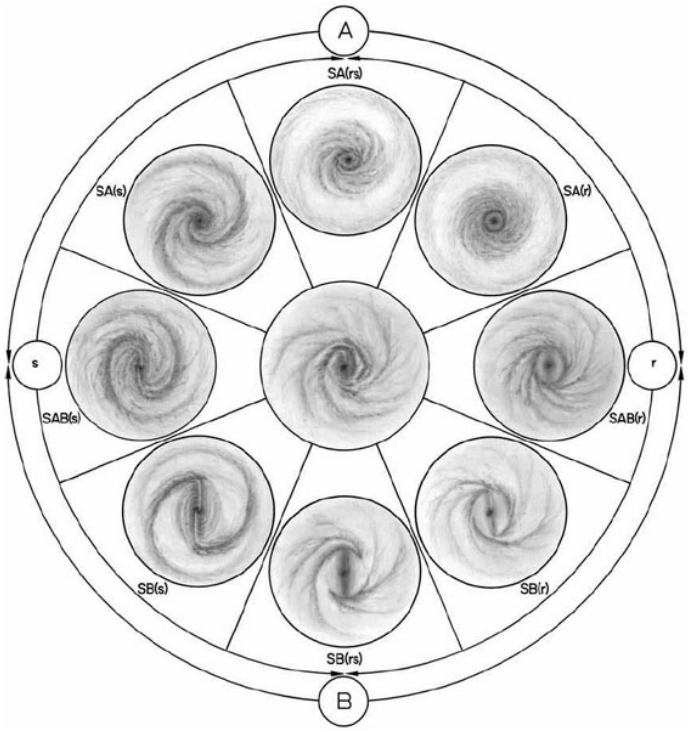

Figure 1.1.2: A cut through the de Vaucouleurs's 3-D scheme. Image credit: https://ned.ipac.caltech.edu/

Finally, galaxies without regular shapes are classified as irregulars.

The Hubble classification scheme was interpreted as an evolutionary sequence from early-type (elliptical) to late-type (spiral) galaxies. Nowadays, we believe that red, elliptical galaxies are the primary products of mergers of blue spiral galaxies and the sequence seems to be reversed. However, due to the historical background, the terms early-type and late-type referring to the elliptical and spiral galaxies are still in use.

Later on, de Vaucouleurs (1959) introduced a classification volume of galaxies by extending Hubble's classification and considering additional morphological properties. In de Vaucouleurs classification system unbarred spirals, spirals with a weak bar, and barred spirals are designated as “SA”, “SAB”, and “SB”, respectively. Also, de Vaucouleurs classified spiral galaxies based on the properties of their spiral arms. Spirals with diffuse and broken arms with a very faint central bulge, irregular galaxies with no bulge similar to the Magellanic clouds, and highly irregular galaxies are labeled as “Sd/SBd”, “Sm/SBm”, and “Im”, respectively. Further, the notation “r” is reserved for the presence of a inner ring-like structure while galaxies without rings are presented as “s”. The notation “rs” is used for the so-called “transition” galaxies. This classification is widely used today, and enters some important correlations, including gas content, bulge-to-disk ratio, star formation activity, metallicity, and colours. Fig. 1.1.2 represents a cut through the de Vaucouleurs's 3-D classification scheme.

Another classification scheme of spiral galaxies proposed by Elmegreen and Elmegreen

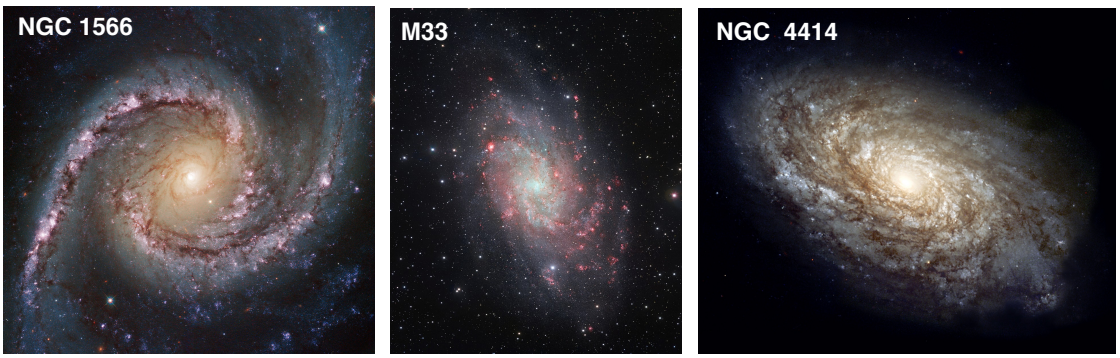

Figure 1.1.3: The three examples of a grand-design galaxy (NGC 1566, image credit: the Hubble Space Telescope), a multi-arm spiral galaxy (M33, image credit: the VLT survey Telescope), and a flocculent spiral (NGC 4414, image credit: the Hubble Space Telescope) from left to right, respectively.

(1982) and Elmegreen and Elmegreen (1987) categorized galaxies into 12 different classes based on the number, continuity, symmetry, and the length of their arms. For instance, spiral galaxies with two long inner arms are in a different class as those with many short arms. A similar classification divides spiral galaxies into three types: grand-design spiral galaxies with two primary and prominent inner arms (e.g., NGC 1566 and M51a), multi-arm spirals (e.g., M33), and flocculent spiral galaxies with patchy, short, filament-like features (e.g., NGC 4414). In Fig. 1.1.3, we show three examples of the different types of spiral galaxies.

1.2 Spiral Structures Theory

Understanding the origin and nature of the spiral patterns in spiral galaxies remains an open question in astrophysics. The number and structure of the arms are tightly linked to the mechanism that forms the spiral features. In this Section, we describe the key processes responsible for the creation of the spiral arms in disk galaxies, namely spiral density wave theory, swing amplification theory, bar driven arms, and tidally induced arms. We refer the reader to the comprehensive reviews of different theories of spiral structure in Dobbs and Baba (2014) and to Shu (2016) for more detailed descriptions of the origin of spiral structures.

1.2.1 Differential rotation of the disk

The simplest context to describe the formation of the spiral pattern is to consider them as a physical material. Imagine a series of stars located along a line through the galactic center. The rotation curve of spiral galaxies is almost flat in the disk meaning that the galactic disk exhibits differential rotation. Therefore, all the stars in the disk of the galaxy move with the same orbital speed and stars located in the larger radii take more time to orbit the center than those located at smaller radii closer to center. As a result, the straight line becomes

curved and very quickly gets wound up, which is called "winding problem" (Carroll and Ostlie 2006). If the spiral arms in the disk galaxies have been formed this way, we would not be able to observe them as spiral patterns today (Fig. 1.2.1).

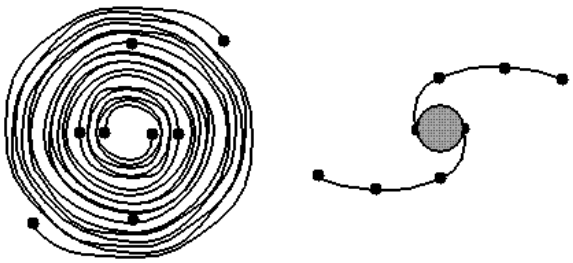

Figure 1.2.1: The "winding problem" caused by differential rotation over 500 million years (left-hand panel) and the observed spiral patterns over 15000 million years (right-hand panel). Image credit: https://www.astronomynotes.com/ismnotes/s8.htm

1.2.2 Spiral density wave theory

To resolve the "winding problem", Lin and Shu (1964) proposed that spiral regions are not made up of fixed material, but instead they are density waves with material (stars and gas) moving through them. The so-called "spiral density wave hypothesis" assumes that the spiral arms keep their shape over many galaxy rotational period (Lin and Shu 1964; Bertin and Lin 1996). In other words, spiral arms are long-lived and stationary in this scenario. This is comparable with assuming that spiral patterns are rotating as a solid-body with a constant specific angular velocity that is called the pattern speed. The angular speed of stars and gas equals the pattern speed at the corotation radius.

Inside the corotation radius, material rotates faster than the spiral pattern. When the gas enters the higher-density region of spiral arms, it may experience a shock which may lead to star formation (Roberts 1969). Consequently, the stars born in the molecular clouds in spiral arms eventually overtake the arms and move away from the spiral patterns as they age (see Fig. 1.2.2). This drift causes an age gradient across the spiral arms. If spiral arms have a constant angular speed, then we expect to find the youngest star clusters near the arm on the trailing side, and the oldest star clusters further away from the spiral arms inside the corotation radius (e.g., Martínez-García et al. 2009). Outside the corotation radius, the spiral pattern moves faster than the gas and leads to the opposite age sequence in the direction of galaxy rotation (see Fig. 1.2.3). In other words, if we group stars/clusters according to their age and measure their azimuthal distance from the spiral arms, we expect to see an offset in the location of stars/clusters with different ages (see Fig. 1.2.4).

Several observational studies have used the age of stellar clusters in nearby galaxies as a tool to test the stationary density wave theory and to investigate the presence of an age gradient across the spiral arms in disk galaxies. For instance, Scheepmaker et al. (2009)

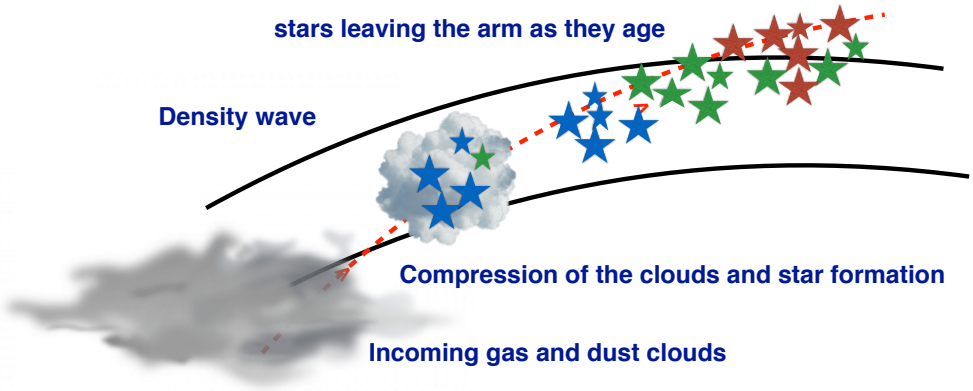

Figure 1.2.2: Illustrative sketch representing the spiral density wave theory. As gas and dust cloud enters the regions with greater density of a spiral arm, it compresses and forms stars. The stars born in this cloud leave the spiral arm as they age. The young, intermediate-age and old stars are shown as blue, green, and red stars. The original idea of this sketch is taken from http://www.astronomynotes.com/ismnotes/s8.htm.

studied the spatial distribution of 1580 stellar clusters in the interacting, grand-design spiral M51a from HST $UBVI$ photometry. They found no spatial offset between the azimuthal distribution of cluster samples of different age. Their results indicate that most of the young (age < 10 Myr) and old stellar clusters (age > 30 Myr) are located at the centers of the spiral arms. Kaleida and Scowen (2010) also mapped the age of star clusters as a function of their location in M51a using HST data and found no clear pattern in the location of star clusters as a function of their age. Both above studies suggest that spiral arms are not stationary, at least not for this particular galaxy in tidal interaction with a companion. In order to study the spatial distribution of star-forming regions, Sánchez-Gil et al. (2011) produced an age map of six nearby grand-design and flocculent spiral galaxies. Only two grand-design spiral galaxies in their sample presented a stellar age sequence across the spiral arms as expected from stationary density wave theory.

Dobbs and Pringle (2010) carried out numerical simulations of the age distribution of star clusters in four different spiral galaxy models, including a galaxy with a fixed pattern speed, a barred galaxy, a flocculent galaxy created using the spiral potential from the models of Sellwood and Carlberg (1984), and an interacting galaxy like M51 (see Fig. 1.2.5). The results of their simulations show that in a spiral galaxy with a constant pattern speed or in a barred galaxy, a clear age sequence across spiral arms from younger to older stars is expected. In the case of a flocculent spiral galaxy, no age gradient can be observed in their simulation. Also in the case of an interacting galaxy, a lack of an age gradient as a function of azimuthal distance from the spiral arms is predicted.

A simulation of an isolated multiple-arm barred spiral galaxy was performed by Grand et al. (2012a), who explored the location of star particles as a function of age around the spiral arms. Their simulation takes into account radiative cooling and star formation. They found no significant spatial offset between star particles of different ages, suggesting that

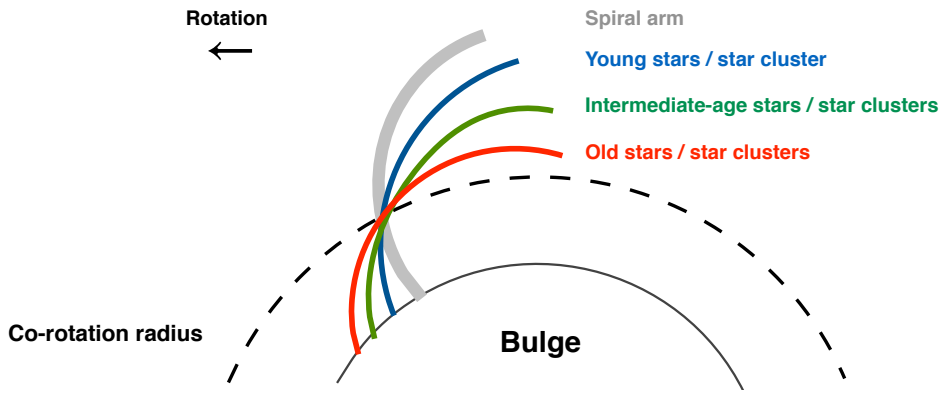

Figure 1.2.3: Illustrative sketch representing the age gradient of stars/star clusters across the spiral arms predicted by the spiral density wave theory. As we can see, there is an age gradient of stars/star clusters from the youngest to oldest on the trailing side of the spiral arm inside the co-rotation radius. The original idea of this sketch is taken from Fig. 1 in Pour-Imani et al. (2016).

spiral arms in such a spiral galaxy are not consistent with the long-lived spiral arms predicted by the static or stationary density wave theory. In a recent numerical study, Dobbs et al. (2017) looked in detail at the spatial distribution of stars with different ages in an isolated grand-design spiral galaxy. They found that star clusters of different ages are all concentrated along the spiral arms without a clear age pattern.

In galaxies where spiral arms are long-lived and stationary as predicted by the stationary density wave theory, one would expect to find an angular offset among star formation and gas tracers of different age within spiral arms (Roberts 1969). The majority of the observational studies of the spiral density wave scenario have tried to examine such an angular offset (Vogel et al. 1988; Rand 1995). Tamburro et al. (2008) detected an angular offset between HI (a tracer of the cold, dense gas) and 24 μm emission (a tracer of obscured star formation) in a sample of 14 nearby disk galaxies. An angular offset between CO (a tracer of molecular gas) and Hα (a tracer of young stars) was detected for 5 out of 13 spiral galaxies observed by Egusa et al. (2009). In another observational work, Foyle et al. (2011) tested the angular offset between different star formation and gas tracers including HI, H_2, 24 μm, UV (a tracer for unobscured young stars) and 3.6 μm emission (a tracer of the underlying old stellar population) for 12 nearby disk galaxies. They detected no systematic trend between the different tracers. Similarly, Ferreras et al. (2012) found no significant angular offset between Hα and UV emission in NGC 4321. Louie et al. (2013) found a large angular offset between CO and Hα in M51a while no significant offsets were found between HI, 21 cm, and 24 μm emissions. These searches for offsets are based on the assumption that the different tracers represent a time sequence of the way a moving density wave interacts with gas and triggers star formation. Elmegreen et al. (2014) used the S^4G survey (Sheth et al. 2010) and discovered embedded clusters inside the dust lanes of several galaxies with spiral waves, suggesting that star formation can sometimes start quickly.

In a recent observational study, Schinnerer et al. (2017) carried out a detailed investiga-

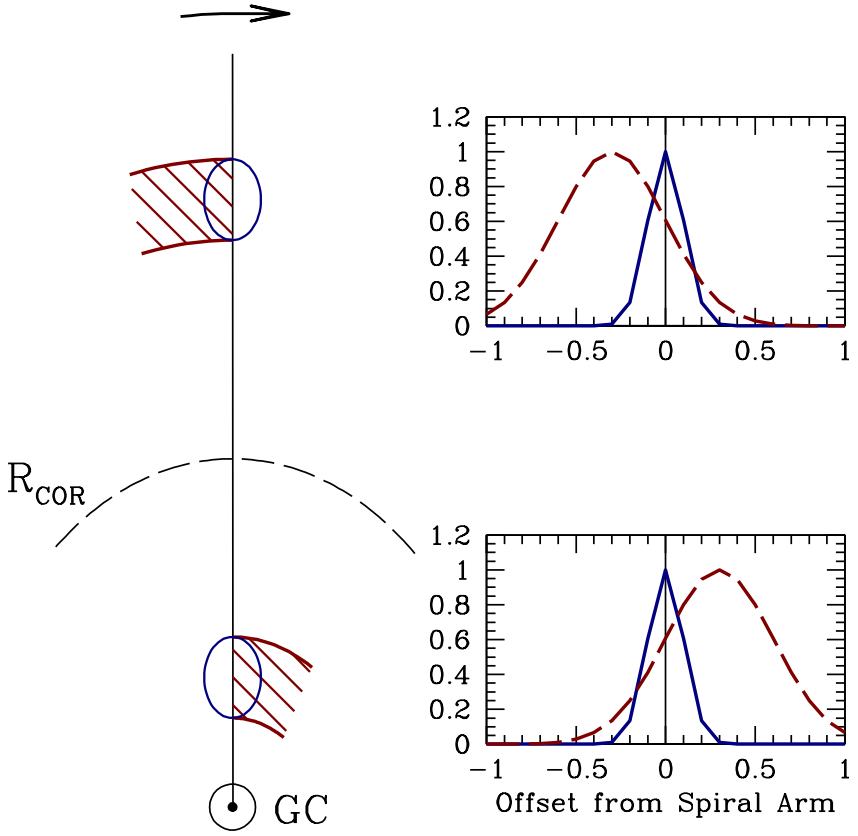

Figure 1.2.4: Sketch of the expected azimuthal offset in the distribution of the young (blue line) and old (red dashed line) stellar populations inside (the bottom panel) and outside (the upper panel) of the co-rotation radius as predicted in spiral density wave theory. Image credit: Fig. 11a in Ferreras et al. (2012).

tion of a spiral arm segment in M51a. They measured the radial offset of the star clusters of different ages ($<$ 3 Myr, and 3-10 Myr) and star formation tracers (HII regions and 24 μm) from their nearest spiral arm. No noticeable spatial offset between star clusters younger and older than 3 Myr was found in M51a. They also found no clear trend in the radial offset of HII regions and 24 μm emission. Similarly, Chandar et al. (2017) compared the location of star clusters with different ages ($<$ 6 Myr, 6-30 Myr, 30-100 Myr, 100-400 Myr, and $>$ 400 Myr) with the spiral patterns traced by molecular gas, dust, young and old stars in M51a. They found cold molecular gas and dark dust lanes to be located along the inner edge of the arms while the outer edge is defined by the old stars (traced with 3.6 μm) and young star clusters. The observed sequence in the spiral arms of M51a is in agreement with the prediction from stationary density wave theory. Chandar et al. (2017) also measured the spatial offset between molecular gas, young ($<$ 10 Myr) and old star clusters (100-400 Myr) in the inner

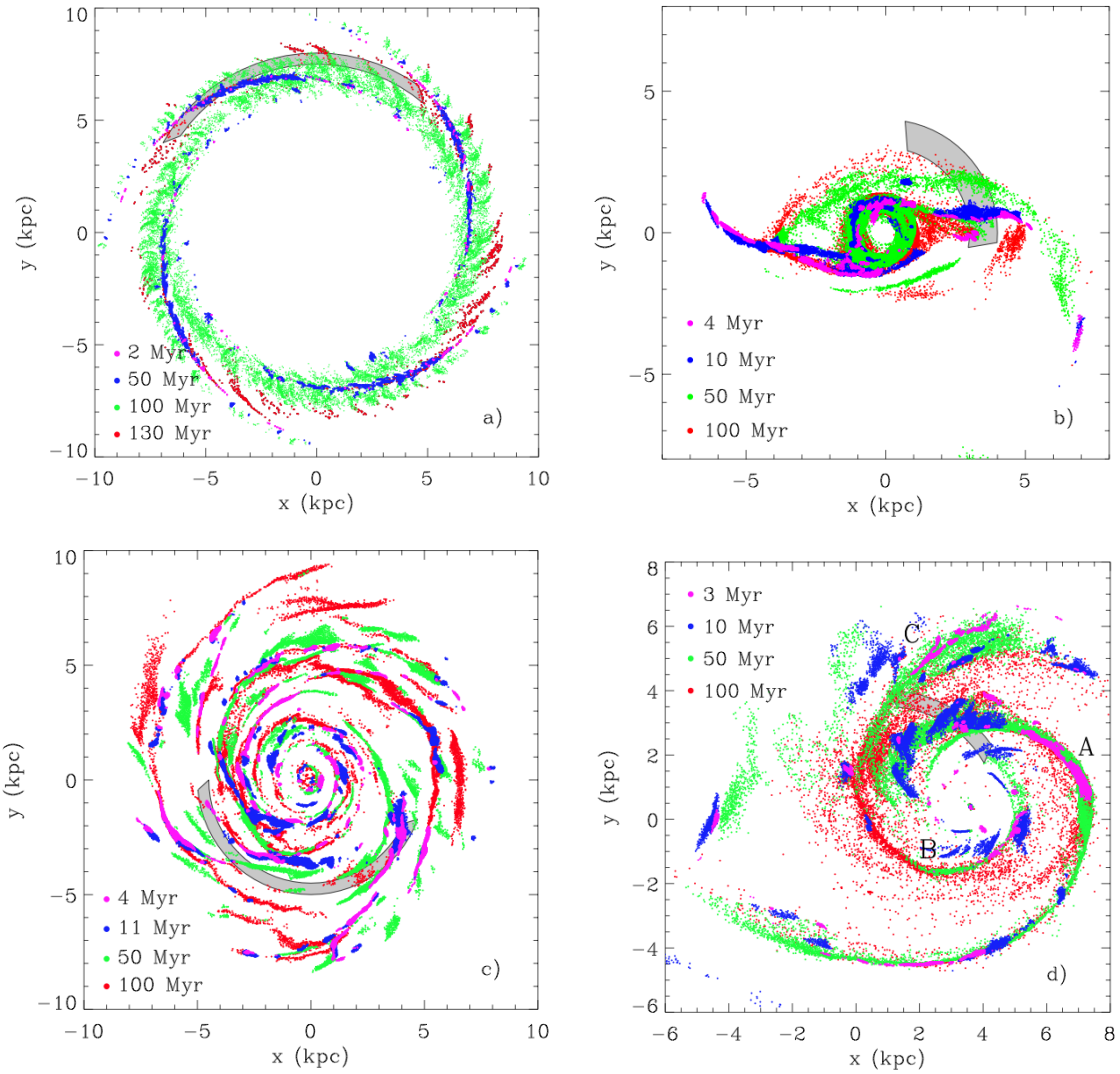

Figure 1.2.5: The spatial distribution of star clusters with different ages (shown in different colours) in simulated spiral galaxies with a constant pattern speed (top left), a barred spiral galaxy (top right), a flocculent spiral galaxy (bottom left), and a galaxy interacting with a companion (bottom right). A clear age gradient and shift in the location of star clusters with different ages can be seen in the galaxy with a constant pattern speed while the distribution in the other cases appears to be much more complex. Image credit: Fig. 2 of Dobbs and Pringle (2010).

(2.0-2.5 kpc) and outer (5.0-5.5 kpc) spiral arms in M51a. They found an azimuthal offset between the gas and star clusters in the inner spiral arm zone, which is consistent with the spiral density wave theory. In the outer spiral arms, the lack of such a spatial offset suggests that the outer spiral arms do not have a constant pattern speed and are not static. Chandar et al. (2017) found no star cluster age gradient along four gas spurs (perpendicular to the spiral arms) in M51a.

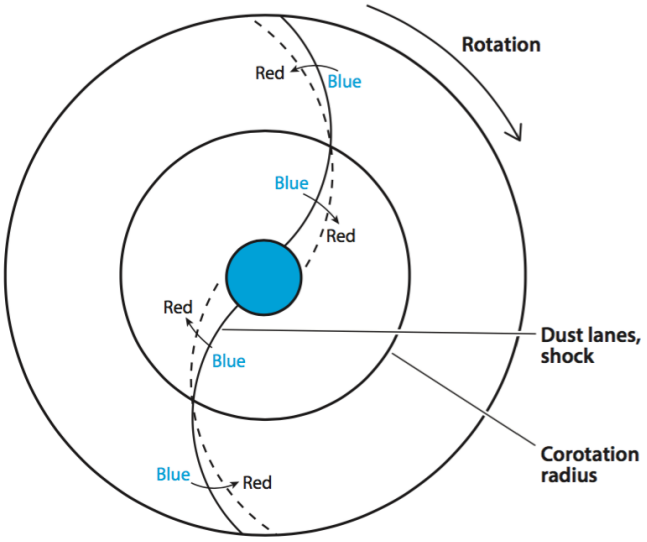

Figure 1.2.6: The expected colour gradient across the spiral arms form blue to red due to the progression of star formation and as a result of the stellar evolution. Image credit: Fig. 1 of Martínez-García et al. (2009).

Another simple test of the stationary density wave theory consists of looking for a colour gradient from blue to red across spiral arms due to the progression of star formation and as a result of the stellar evolution (see Fig. 1.2.6). It is important to note that this method can be affected by the presence of dust. Several observational studies have tried to test the stationary density wave theory by looking for colour gradients across spiral arms. In an early study of the $(B-V)$ colours and total star formation rates in a sample of spiral galaxies with and without grand design patterns, Elmegreen and Elmegreen (1986) found no evidence for an excess of star formation due to the presence of a spiral density wave, and explained the blue spiral arm colours as a result of a more significant compression of the gas compared to the old stars, with star formation following the gas density. Martínez-García et al. (2009) studied the colour gradients across the spiral arms of 13 SA and SAB galaxies. Ten galaxies in their sample present the expected colour gradient across their spiral arms.

In conclusion, there have been numerous observational studies aiming at testing whether spiral arms are long-lived and compatible with the density wave theory. In many cases, the conclusions show conflicting results, and the nature of spiral arms is still an open question.

1.2.3 Swing amplification theory

An alternative hypothesis to describe the physical origin and evolution of spiral patterns in disk galaxies is the so-called "swing amplification theory" (Goldreich and Lynden-Bell 1965; Julian and Toomre 1966; Goldreich and Tremaine 1978; Toomre 1981; Sellwood and Carlberg 1984; Carlberg and Freedman 1985; Bottema 2003; Sellwood 2011; Fujii et al. 2011; Grand et al. 2012a,b; Baba et al. 2013; D'Onghia et al. 2013). The swing amplification process operates through a combination of self-gravity and shear of the galactic disk.

In the regions where self-gravity dominates, segments produced by over-dense areas make up the spiral arms and eventually the generated spiral arms are stretched-out and broken due to the disk shear (D'Onghia et al. 2013). Therefore, this mechanism leads to the formation of short-lived, transient, and recurrent structures in flocculent and multi-arm spiral galaxies that can be continuously broken and re-made.

Sellwood and Carlberg (1984) did a pioneering study supporting the idea of short-lived spiral arms. They performed two-dimensional N-body simulations in which the spiral arms heat the disk of the galaxy and make the disk more stable against the growth of non-axisymmetric features. As a result, the spiral arms disappear within an interval of about ten rotational periods. Sellwood and Carlberg (1984) argued that some dynamical cooling mechanism, such as the continuous addition of a cold population of stars, is essential to preserve the spiral patterns.

Fujii et al. (2011) used high-resolution three-dimensional N-body simulations of a pure stellar disk and showed that although spiral arms are transient and recurrent, they can survive for more than 10 Gyr without the help of cooling mechanisms. Their results suggest that the quick disappearance of the spiral features in the simulations of Sellwood and Carlberg (1984) could be due to a low number of particles, resulting in a faster growth of spiral arms that then heat the disk and decays the spiral patterns. Fig. 1.2.7 shows the evolution of spiral arms in a simulated multi-arm spiral galaxy by Fujii et al. (2011) for 30M, 9M, 3M, 1M, and 300K number of particles at 0.5, 2, 6, and 10 Gyr. Also, in this N-body simulation, the spiral arms appear to decay into smaller pieces with a size of a few kpc. Subsequently, these segments are reconnected due to the differential rotation and generate large scale patterns.

Recently, Baba (2015) pointed out that grand-design spiral arms in barred galaxies are self-excited, transient patterns rather than bar-driven stationary. Their study suggests that spiral modes are time-dependent, i.e., the amplitudes and pitch angels of the spiral arms vary over a few rotational periods of the galaxy.

In addition to the short-lived, transient, and non-stationary spiral patterns, N-body simulations suggest that the pattern speed of spiral arms is not constant, but instead decreases with radius in a similar fashion to the rotation of star particles in the disk (Wada et al. 2011; Grand et al. 2012a,b; Baba et al. 2013; Roca-Fàbrega et al. 2013).

In summary, the swing amplification theory is associated with the formation and evolution of spiral arms in flocculent and multi-arm spiral galaxies even though there is yet no observational evidence to prove it. The N-body simulations of isolated disk galaxies suggest that spiral arms appear as transient, short-lived features rather than long-lived waves as in the spiral density wave theory that can recurrently reform.

1.2.4 Bar driven spiral arms

The grand-design structure of spiral patterns is found to be more common in barred galaxies than unbarred ones (Elmegreen and Elmegreen 1982). In many barred grand-design galaxies the spiral arms appear to be connected to the ends of the central bar, suggesting that the

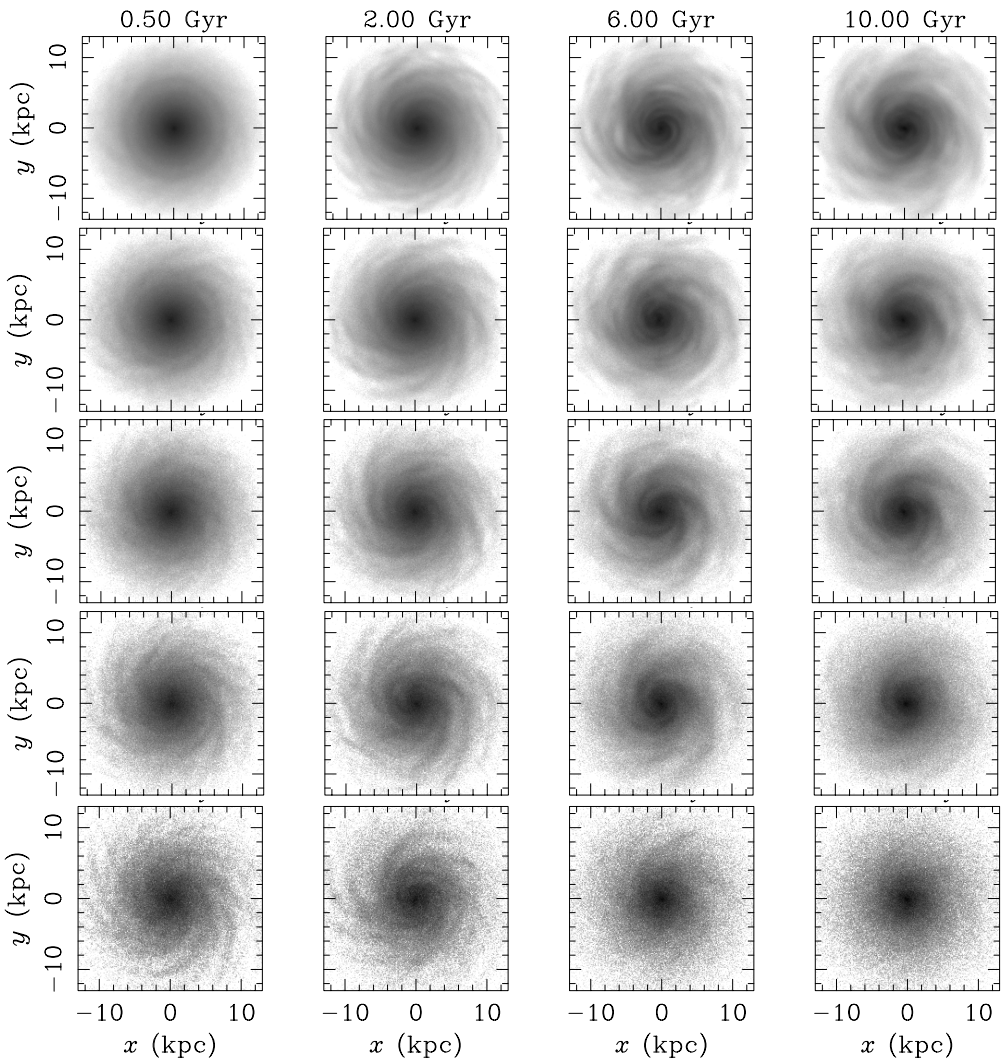

Figure 1.2.7: The evolution of spiral arms in a simulated multi-arm spiral galaxy for 30M, 9M, 3M, 1m, and 300K number of particles (from top to bottom) at 0.5, 2, 6, and 10 Gyr (from left to right). Image credit: the top panels of Fig. 2, 3, 4, 5, and 6 of Fujii et al. (2011).

bar and spiral arms are related and have the same pattern speed. This was first proposed by Sanders and Huntley (1976), who carried out a numerical hydrodynamical study to investigate the response of the gas component to a steady bar perturbation. Their simulation showed that the gas ultimately settles into a steady state by forming a prominent two-arm trailing spiral structure rotating with the same angular speed of the bar.

The orbits of stars in the bar driven spiral arms are determined by "manifold theory" (e.g., Romero-Gómez et al. 2006, 2007; Voglis et al. 2006; Tsoutsis et al. 2009; Athanassoula et al. 2009a,b, 2010; Athanassoula 2012; Efthymiopoulos et al. 2019). According to this theory,

in the spiral arms induced by a bar, stars move along the arms rather than crossing them as predicted in the density wave theory (Athanassoula et al. 2010; Athanassoula 2012). The manifold theory also predicts that spiral arms in galaxies with stronger bars are more open when compared to galaxies with weaker bars (Athanassoula et al. 2010). This predicted trend was confirmed by Martínez-García (2012), who examined the correlation between the strength of the bars and the pitch angle of spiral arms in 27 barred spirals. Although ≈ 70% of the barred spiral galaxies exhibit grand-design patterns (Elmegreen and Elmegreen 1982), there are many flocculent (e.g., NGC 1313, NGC 5068) and multi-arm spirals (e.g., NGC 3344, NGC 6946, NGC 1232) with a central bar (Dobbs and Baba 2014). In summary, several observational studies have investigated the relationship between the bars and arms in barred galaxies and confirmed the presence of bar-driven spiral arms (Block et al. 2004; Salo et al. 2010; Martínez-García 2012), whilst others did not report any obvious evidence (Seigar and James 1998; Durbala et al. 2009; Kendall et al. 2011). Thus, observations propose that the bar-driven spiral theory is not applicable to all barred galaxies.

In some barred galaxies, the spiral arms do not appear to begin at the end of the bar (e.g., NGC 1073, NGC 4548, and NGC 5383, Sellwood and Sparke 1988). An alternative interpretation for the origin of the spiral arms in barred galaxies is that the bar and spiral patterns have different pattern speeds and thus are independent features (Sellwood and Sparke 1988; Rautiainen and Salo 1999). The N-body simulations of a stellar disk by Sellwood and Sparke (1988) pointed out the existence of various pattern speeds in disk galaxies in which the bar has a much higher pattern speed than the spiral arms. Their simulations showed that the spiral patterns continuously break from and join to the bar.

A third possibility is that the spiral arms are not stationary or independent features, but instead they are transient structures enhanced by the bar (Grand et al. 2012a). In a hydrodynamic/N-body simulation of a barred spiral galaxy performed by Grand et al. (2012a), spiral arms appear to be transient structures with their pattern speed decreasing with radius. The non-stationary nature of spiral arms in barred galaxies was also suggested in the numerical studies by Fux (1997); Baba et al. (2009); Baba (2015).

However, the direct connection between the bars and arms is not yet fully understood and there is no clear evidence of which scenario is the primary mechanism to form the spiral arms in barred galaxies.

1.2.5 Tidally induced spiral arms

Grand-design structures in spiral galaxies might be induced by nearby galaxies through tidal interactions (e.g., Toomre and Toomre 1972; Kormendy and Norman 1979; Elmegreen and Elmegreen 1982, 1987; Hernquist 1990; Elmegreen et al. 1991; Salo and Laurikainen 2000a,b; Bottema 2003; Oh et al. 2008; Dobbs et al. 2010; Struck et al. 2011; Pettitt et al. 2016, 2017). The tidal interactions create bridge (facing the companion galaxy) and tail (on the opposite side of the bridge) arms in the host disk galaxies. Also, such interactions may change the star formation properties and result in strong bursts of star formation in the tidally induced arms (Keel et al. 1985; Kennicutt et al. 1987; Di Matteo et al. 2007; Pettitt

et al. 2017).

The first model of tidally induced spiral arms was presented by Toomre and Toomre (1972), who used non-interacting test particle simulations to investigate whether the grand-design spirals are the results of gravitational interactions between a host galaxy and its companion. In their simulations, the tidal arms could be triggered only in the outer regions of the galaxy. Later, Hernquist (1990) included self-gravity of stars in higher resolution simulations and found that the tidal arms extend to smaller radii and thus are enhanced in the disks.

There are many numerical studies of the formation of tidal arms in interacting systems including NGC 5194 (M51a)/NGC 5195 (e.g., Howard and Byrd 1990; Barnes 1998; Salo and Laurikainen 2000a,b; Dobbs et al. 2010; Pettitt et al. 2016). For instance, Dobbs and Pringle (2010) calculated hydrodynamical models of the galaxy M51a and its interactions with its companion NGC 5195, focusing mainly on the dynamics of the gas. Their simulation can produce the present-day appearance (300 Myr) of M51a together with spurs and substructures along one spiral arm. The evolution of the gas disk with 1% warm gas in the simulated M51a/NGC 5195 interacting system is shown for different time frames (see Fig. 4 of Dobbs and Pringle 2010). Briefly, their results indicate that the host galaxy appears as a flocculent spiral after 60 Myr with no clear signature of the interaction. The two-armed structure formed in the outer parts of the galaxy (R>5 kpc) after 120 Myr. Subsequently, the spiral patterns develop and extend toward smaller radii ($\sim$2 kpc) as the companion becomes progressively bound to the host galaxy, and eventually the two galaxies merge at 370 Myr. Further, they pointed out that the pattern speed of the produced spiral arms is decreasing with radius, and thus tidally induced spirals behave differently than long-lived stationary spiral arms predicted by density wave theory.

However, there is a possibility that a combination of these scenarios is needed to explain the presence of the observed spiral structure.

1.3 Lopsidedness in Spiral Galaxies

It has been known for a long time that the gas and/or stellar component of a large fraction of spiral galaxies is asymmetric, i.e., it is more extended on one side of the galaxy than the other. This phenomenon is called “lopsidedness” (Baldwin et al. 1980; Block et al. 1994; Richter and Sancisi 1994; Rix and Zaritsky 1995; Zaritsky and Rix 1997; Jog 1997; Haynes et al. 1998; Matthews et al. 1998; Rudnick and Rix 1998; Swaters et al. 1999; Rudnick et al. 2000; Jog 2002; Bournaud et al. 2005a,b; Angiras et al. 2006, 2007; Reichard et al. 2008; Mapelli et al. 2008; Sancisi et al. 2008; van Eymeren et al. 2011; Zaritsky et al. 2013; Elagali et al. 2019; Dupuy et al. 2019).

The lopsided distribution of neutral hydrogen (HI) in spiral galaxies was first highlighted by Baldwin et al. (1980). They investigated the large-scale asymmetry in the distribution of HI in four nearby galaxies, M101, NGC 891, NGC 2841, and IC 342 and claimed that lopsidedness is a common feature among disk galaxies. Later, Richter and Sancisi (1994)

analyzed the global HI line profiles of a sample of 1700 galaxies and concluded that at least 50% of the galaxies are significantly lopsided in their gaseous component. Their result was confirmed by Haynes et al. (1998), who studied high-resolution global HI profiles of 140 isolated spiral galaxies. Their findings also suggest that some of the lopsidedness might be triggered by nearby companions. An example of lopsided HI gas in M101 is shown in Fig. 1.3.1.

The lopsidedness of disk galaxies is not limited to the gaseous component. Rix and Zaritsky (1995) found that 1/3rd of their sample of 18 galaxies is significantly lopsided in the stellar populations. In their study, Rix and Zaritsky (1995) emphasized that the observed lopsidedness in the stellar populations is less strong than in the HI distribution and occurs at smaller galactocentric distances. These results were later confirmed by Zaritsky and Rix (1997), who studied a sample of 60 nearly face-on spiral galaxies and quantified that about 30% of the galaxies are strongly asymmetric in the near-infrared bands (I and K), where light is contributed mostly by unevolved, low-mass stars. Since none of the galaxies in their sample were interacting, they concluded that a nearby, current interaction is not necessary to induce significant lopsidedness. Furthermore, Kornreich et al. (1998) investigated the lopsidedness in the optical images of 32 face-on spiral galaxies and found that 30% of them are not axisymmetric. A similar average fraction of lopsided galaxies was corroborated by Bournaud et al. (2005a). They reported that 30% of their 149 galaxies are lopsided. Using N-body simulations, Bournaud et al. (2005a) found that strong asymmetry might be a result of tidal encounters, minor mergers, and cosmic gas accretion. Among the three possible scenarios, only cosmic gas accretion can describe the existence of lopsidedness in isolated galaxies that do not show any sign of current companion or recent interactions. Reichard et al. (2008) carried out an observational study of a large sample of $\sim$25000 asymmetric galaxies at $z < 0.06$ from Sloan Digital Sky Survey (SDSS), and found that the observed lopsided light distribution correlates with the corresponding lopsidedness in the stellar mass distribution.

Lopsidedness may greatly affect the evolution of the host galaxy and thus have an impact on its star formation (Jog and Combes 2009). For instance, Rudnick et al. (2000) investigated the correlation between the degree of lopsidedness and star formation in a sample of 40 spiral galaxies. They found that both recent (the past 1 Gyr) and current star formation of galaxies are linked with lopsidedness. They suggest that minor mergers could be the cause of asymmetry and enhance star formation.

Although many galaxies exhibit lopsidedness, its physical origin is not yet clearly understood. Lopsidedness in galaxies has been observed in the various tracers, regions, and the environment. For instance, it is detected in the young and old stars, in the HI gas, in the outer regions of the galaxy and within the optical disk, and in a high-density group of galaxies or in the field. Therefore, it is possible that multiple physical mechanisms may generate lopsidedness. Here, I summarize the most likely scenarios for the formation of asymmetry in disk galaxies.

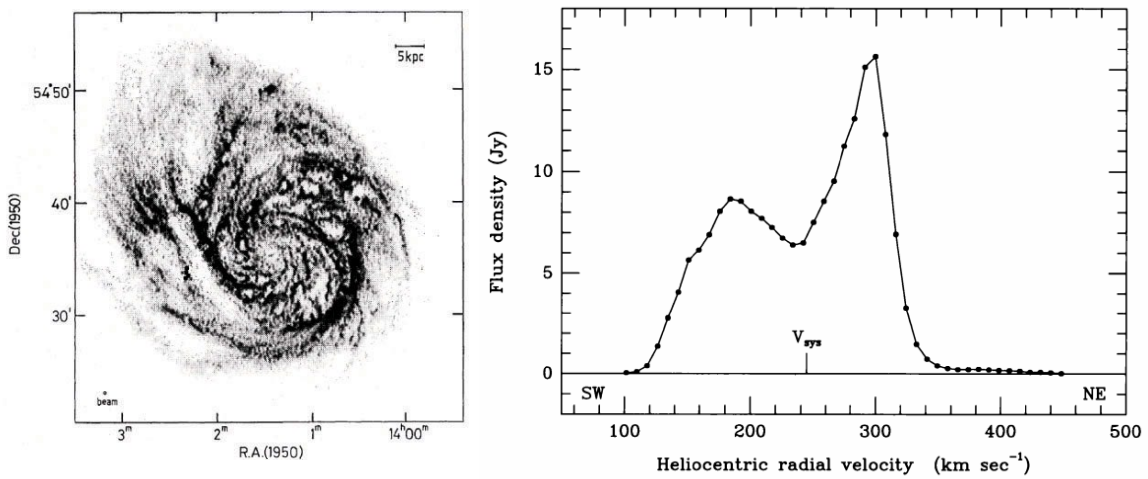

Figure 1.3.1: Left-hand panel: The total HI column density of M101 obtained using the Westerbork Synthesis Radio Telescope. Image credit: Fig. 1 in Kamphuis et al. (1991). Right-hand panel: The global lopsided HI profile of M101. Image credit: Kamphuis (1993).

1.3.1 Tidal encounters and mergers

One of the most promising models to explain the observed asymmetry in spiral galaxies is tidal interactions or a merger with a small companion (Beale and Davies 1969; Weinberg 1995; Walker et al. 1996; Jog 1997; Schoenmakers et al. 1997; Jog 2002; Yozin and Bekki 2014; Pardy et al. 2016).

A numerical study by Walker et al. (1996) showed that a minor merger induces significant disk lopsidedness lasting at least for 1 Gyr. Angiras et al. (2006) and Angiras et al. (2007) investigated the correlation between lopsidedness amplitude and environment. They found that galaxies in a high-density group environment show a higher quantitative lopsidedness than those in the field. Also, they reported that early-type galaxies in groups are more lopsided than late-type ones, especially in their outskirts. These results appear to suggest that tidal encounters may be the main mechanism responsible for the existence of significantly lopsided early-type galaxies. This is not surprising given that tidal interactions tend to cause the evolution of galaxies toward being an early-type. Therefore, a tidal encounter may be the dominant process in group galaxies where interactions take place frequently ($\sim 0.3\ \mathrm{Gyr}^{-1}$, Jog and Combes 2009).

In contrast, in their study of 149 galaxies Bournaud et al. (2005a) found that late-type galaxies in the field are more lopsided than early-type ones. Also, their simulations of an isolated galaxy show that a strong lopsidedness in the host galaxy occurs during the interaction itself. Such triggered lopsidedness is short-lived and will be visible only for about 500 Myr. Although their N-body simulations show that tidal encounters and mergers can produce significant lopsidedness, they do not explain various observed statistical properties such as the

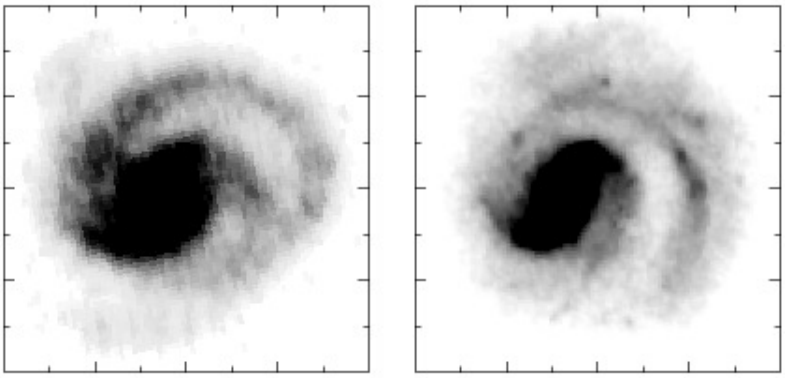

Figure 1.3.2: A snapshot of a simulation of asymmetrical gas accretion along two filaments producing similar lopsidedness in the host galaxy (left-hand panel) to the one observed in the NIR image of NGC1637 in the Ohio State University Bright Galaxy Survey (right-hand panel). Image credit: Fig. 18 in Bournaud et al. (2005a).

strong lopsidedness found in late-type field galaxies. Bournaud et al. (2005a) did not find any link between lopsidedness and the strength of the tidal interactions. Further, the degree of lopsidedness does not seem to be connected with the presence of a companion galaxy in an observational study by Wilcots and Prescott (2004).

1.3.2 Gas accretion

An alternative scenario proposed to explain the lopsidedness in field or in isolated galaxies is gas accretion from outside the galaxy. There are several numerical and observational studies indicating that galaxies steadily accrete gas from the intergalactic medium (IGM) (Bournaud and Combes 2002; Block et al. 2002; Bournaud et al. 2005a; Mapelli et al. 2008; Sancisi et al. 2008; de Blok et al. 2014). A galaxy can experience an asymmetric gas accretion from various external filaments, and thus the accretion rate will be different for each filament (Bournaud and Combes 2002). This asymmetrical gas accretion may lead to a lopsidedness in the galaxy disk, both the gaseous and the stellar component through star formation (Bournaud et al. 2005a).

In simulations of asymmetrical gas accretion along two and three filaments with a different accretion rate, Bournaud et al. (2005a) found that asymmetrical accretion can trigger strong lopsidedness in the gaseous and stellar disk of an isolated galaxy. The amplitude of the lopsidedness in their simulations decreases after a few Gyr, and when the accretion is stopped, the produced asymmetry has a time-scale of about 3 Gyr. An example of their simulations, that fits the morphology of NGC 1637 is shown in Fig. 1.3.2.

Further, Bournaud et al. (2005a) discussed how this scenario can explain the observed high fraction of lopsidedness in late-type galaxies. Gas accretion would tend to lead to the evolution of a galaxy towards late-type morphology (Bournaud and Combes 2002). Thus, in contrast to the tidal interactions and mergers scenario, the most lopsided galaxies due to gas accretion will generally tend to be late-type ones.

However, if asymmetrical gas accretion is frequent, one would expect to find strong lopsidedness in isolated or field galaxies as well.

1.3.3 Ram pressure stripping

The third possible mechanism to generate lopsidedness in galaxies is ram pressure stripping. The signature of ram pressure stripping has been observed in massive galaxy clusters (White et al. 1991; Acreman et al. 2003; Chung et al. 2007; Vollmer 2009; Ruggiero and Lima Neto 2017; Sheen et al. 2017; Yoon et al. 2017) and in few cases in galaxy groups (McConnachie et al. 2007; Westmeier et al. 2011; Heald et al. 2016; Vulcani et al. 2018). Many studies have shown that ram pressure stripping may cause the HI deficiency in groups (Sengupta and Balasubramanyam 2006; Sengupta et al. 2007; Freeland et al. 2010; Dénes et al. 2016). The motion of a galaxy through hot ionized IGM may produce ram pressure which can remove and strip away the gas from the galaxy disk (Gunn and Gott 1972). In particular, ram pressure stripping is effective in removing the HI gas from outer regions of a galaxy if the IGM density is high enough (Gunn and Gott 1972; McConnachie et al. 2007):

$$\mathrm{n_{IGM}} \geq 3.7 \times 10^{-6}\mathrm{cm^{-3}}(\frac{100\mathrm{kms^{-1}}}{\mathrm{v_{rel}}})^2(\frac{\Sigma_{\mathrm{HI}}}{10^{19}\mathrm{cm^{-2}}})^2 \tag{1.1}$$

where $\mathrm{v_{rel}}$ stands for the galaxy relative velocity with respect to the IGM and Σ_{HI} presents the column density of HI gas.

As a galaxy with inclined orientation moves through a high-density IGM the outer gas disk is quickly stripped away and generates a trailing stream of HI while the gas will be compressed at the leading edge of the outer disk (Quilis et al. 2000). This mechanism will lead to an asymmetry in the HI gas distribution. If the IGM density is higher than the threshold value in equation 1.1, any galaxy independently of its environment will experience ram pressure generating lopsidedness in the distribution of its gas (Mapelli et al. 2008).

After all, it is also possible that lopsidedness is a generic phenomenon of galaxies that does not originate from external events like as accretion of satellite galaxy into the disk of the host galaxy (Zaritsky et al. 2013).

1.4 Legacy ExtraGalactic UV Survey

All of the work in this dissertation has been done based on using high-quality multi-band photometric catalogs of star clusters produced by the Legacy ExtraGalactic UV Survey (LEGUS, GO–13364, PI: D. Calzetti) team to study the structure of spiral patterns in four nearby spiral galaxies. A general description of the standard data reduction of the LEGUS datasets and the goals of the survey can be found in Calzetti et al. (2015).

LEGUS is a Cycle 21 Hubble Space Telescope (HST) Treasury program designed to investigate the relation between star formation and its galactic environment in nearby galaxies

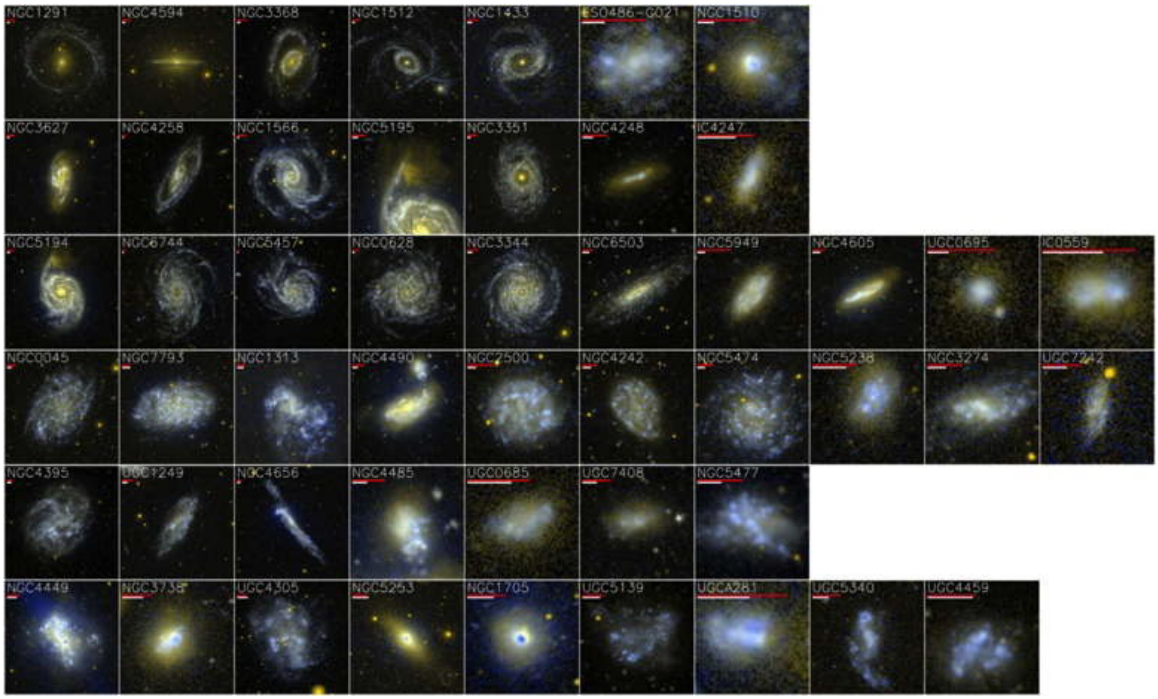

Figure 1.4.1: The montage of the $GALEX$ two-colour images for the 50 LEGUS galaxies. Image credit: Fig. 1 in Calzetti et al. (2015).

and to link the small and large scales of star formation. LEGUS survey has collected high-resolution images (0.0396″ / pix) of 50 local star-forming galaxies in the distance range of ≈ 3.5 - 12 Mpc in five broad-band filters (NUV, U, B, V, and I) with the UVIS channel of the Wide Field Camera Three (WFC3), supplemented with archival Advanced Camera for Surveys (ACS) imaging when available. In this distance range, HST is able to resolve the young stellar clusters and galaxy structures on pc and kpc scales. This large sample of star-forming spiral and dwarf galaxies covers a broad range of morphology, structure, galaxy mass, star formation rate (SFR), and metallicity. Fig. 1.4.1 shows the images for the 50 LEGUS sample galaxies.

1.4.1 Young stellar clusters

A large fraction of stars are believed to form in coeval clustered environments called star clusters (e.g., Lada and Lada 2003; Fall 2004; Portegies Zwart et al. 2010). Star clusters are gravitationally bound stellar over-densities composed of a few hundred to tens of millions of individual stars, with radii in the range of one to tens of parsec (pc), and masses between some hundred to $10^7 M_\odot$ (Portegies Zwart et al. 2010). The stellar component of star cluster form at the same time within the same parent cloud of gas and dust, and thus the cluster stars have approximately the same age and metallicity. Only a small fraction of these star clusters are long-lived structures, meaning that they will remain gravitationally bound and survive

for Gyrs (Goddard et al. 2010; Adamo et al. 2011; Johnson et al. 2016). These long-lived star clusters allow us to study stellar evolution and the star formation history of individual galaxies. In this dissertation, however, we use young star clusters ($\leq$ 200 Myr) to study the spiral structure of nearby spiral galaxies. The young star clusters are located within the disk of a galaxy in contrast to globular clusters, which are massive and old stellar clusters that can be found in the halos of galaxies.

Numerous physical properties can be measured for star clusters. Some features such as magnitude and size are directly measurable from observations while some others can be only derived through modeling (e.g., age, mass, and extinction). A detailed description of the cluster extraction, identification, classification, photometry, and spectral energy distribution (SED) fitting for the LEGUS galaxies is presented in Adamo et al. (2017) and Messa et al. (2018). Here, I will summarize the aspects of the mentioned papers that are relevant to the analysis carried out in this dissertation.

Stellar cluster candidates within each of the LEGUS galaxies were identified and extracted through an automated process using SExtractor (Bertin and Arnouts 1996), which filters out the single stars and background sources, from the white-light images produced with the five LEGUS filters. The SExtractor input parameters were set to detect sources with a minimum 4σ detection in at least five contiguous pixels.

Subsequently, the concentration index (CI) of each of the extracted objects in the initial catalogs was measured. The CI is defined as the magnitude difference between apertures of a radius of 1 pixel and 3 pixels and measures how much the light is concentrated in the center of the object. The CI distribution of stars (point sources) highly peaks around the average value of the stellar point spread function (PSF) while clusters have on average higher CI values and appear significantly broader. Therefore, applying a CI cut allows us to distinguish between stars and star cluster candidates and remove a significant amount of stars from the catalogs. The CI cut-off varies from galaxy to galaxy because the resolution depends on the HST cameras used and on the distance of the galaxy (e.g., the cut-off value of the CI for NGC 1566, NGC 3738, and NGC 6503 is 1.35, 1.4, and 1.25, respectively).

Further, the photometry was performed using a fixed circular aperture of 4 pixels in radius, and the sky background was measured from an annulus with 7 pixels in inner radius and 1 pixel in width. A final cut was made by including sources that satisfy the two following conditions: (1) the V band CI must be greater than the CI cut-off and (2) the source must be detected in at least two filters with a photometric error $\leq$ 0.3 mag. In addition, the photometry within each band, for all sources, was corrected for foreground Galactic extinction according to Schlafly and Finkbeiner (2011).

However, the produced catalogs are likely to contain contamination sources, i.e., background galaxies, bright stars with a CI slightly higher than the cut-off CI, foreground stars, and multiple stars. To remove non-cluster sources from the automatic catalogs, sources brighter than -6 mag in the V band and detected in at least four bands were visually selected and classified by three independent members of the LEGUS team.

The inspected sources were divided into four morphological classes: Class 1 contains

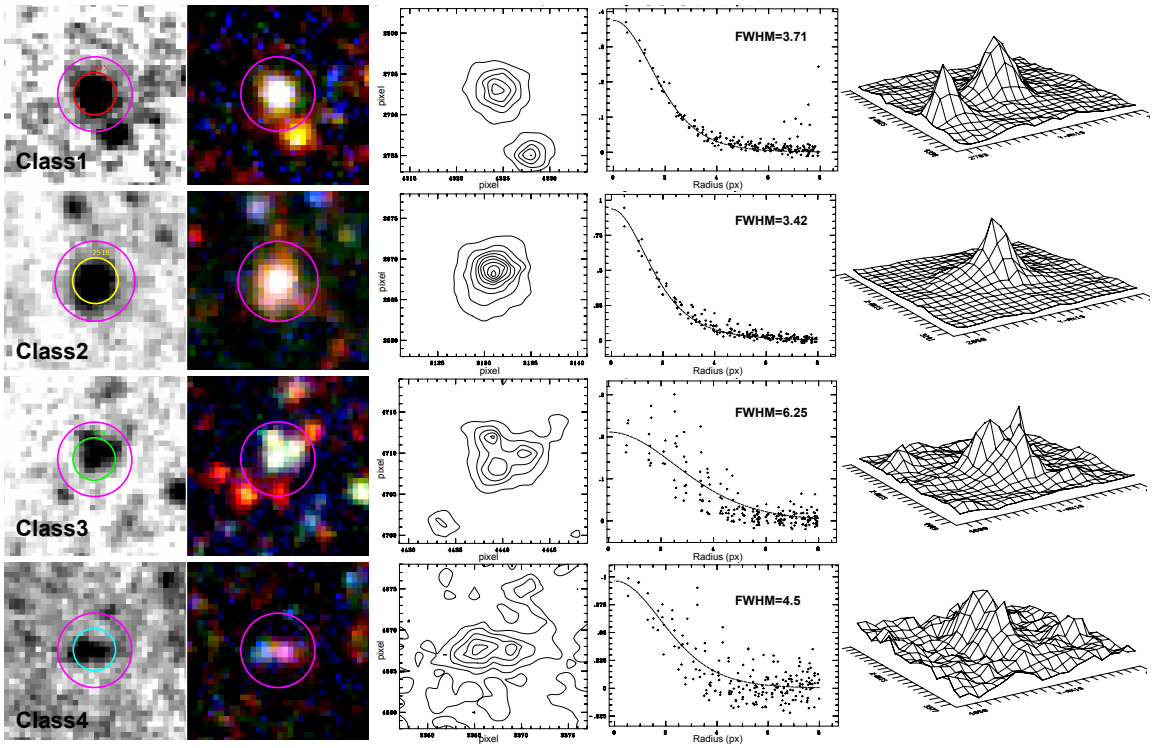

Figure 1.4.2: An example of all four star cluster classifications. The two first columns show each object classified as Class 1, Class 2, Class 3, and Class 4 (from top to bottom) in the V band and in a three colour composite. The inner and outer rings show the aperture radius used to do photometry and the position of the measured background annulus, respectively. The middle and right columns show the contours, the radial profile, and the surface plot of the classified source. Image credit: Fig. 3 in Adamo et al. (2017).

compact, symmetric, and centrally concentrated clusters. Class 2 includes compact clusters with a less symmetric light distribution. Class 3 represents less compact and multi-peak cluster candidates with asymmetric profiles, and Class 4 consists of unwanted objects like single stars, multiple stars, or background sources. Unclassified objects were labeled as Class 0. Fig. 1.4.2 shows an example of all four classifications.

In order to derive the cluster physical properties such as age, mass, and extinction, the SED of the clusters was fitted with the Yggdrasil stellar population models (Zackrisson et al. 2011). The stellar libraries of the Padova AGB and Geneva tracks without stellar rotation from Starburst99 (Leitherer et al. 1999; Vázquez and Leitherer 2005) were used to create two sets of simple stellar population (SSP) models. These libraries assume a fully sampled Kroupa (2001) initial mass function (IMF), with stellar masses between 0.1 and 100 $M_{\odot}$. In addition, three extinction/attenuation laws were applied to the fit: (1) the Milky Way extinction law from Cardelli et al. (1989), (2) the starburst extinction law from Calzetti et al. (2000) in which stars and gas suffer the same reddening, and (3) the differential starburst attenuation law by Calzetti et al. (2000) where the gas emission suffers higher extinction than the stars. The uncertainties derived in the physical parameters of the star clusters are

on average 0.1 dex (Adamo et al. 2017).

For some of the LEGUS galaxies, star cluster properties were also estimated based on a Bayesian approach, using the Stochastically Lighting Up Galaxies (SLUG) code (da Silva et al. 2012). A detailed and complete explanation of the Bayesian approach can be found in Krumholz et al. (2015). A comparison between the deterministic approach based on Yggdrasil models and the Bayesian approach with SLUG models presented by Krumholz et al. (2015) suggests that the derived cluster properties are quite uncertain at cluster masses below 5000 $M_{\odot}$.

The analyses and results presented hereafter were obtained using Yggdrasil deterministic models based on the following parameters:

- Padova evolutionary tracks produced with solar metallicity stellar libraries
- Milky Way extinction curve
- Kroupa (2001) stellar initial mass function

2

Star Cluster Age Gradients Across Spiral Arms

This chapter is a partially revised version of Shabani et al. (2018). "Search for Star Cluster Age Gradients Across Spiral Arms of Three LEGUS Disk Galaxies ", published in MNRAS 478, pp. 3590–3604.

2.1 Introduction

Understanding how spiral patterns form in disk galaxies is a long-standing issue in astrophysics. Two of the most influential theories to explain the formation of spiral structure in disk galaxies are named stationary density wave theory and swing amplification. The stationary density wave theory poses that spiral arms are static density waves Lindblad (1963); Lin and Shu (1964). In this scenario, spiral arms are stationary and long-lived. The swing amplification proposes instead that spiral structure is the local amplification in a differentially rotating disk (Goldreich and Lynden-Bell 1965; Julian and Toomre 1966; Sellwood and Carlberg 1984; Sellwood 2011; Elmegreen 2011; D'Onghia et al. 2013). According to this theory, individual spiral arms would fade away in one galactic year and should be considered transient features. Numerical experiments suggest that non-linear gravitational effects would make spiral arms fluctuate in density locally but be statistically long-lived and self-perpetuating (D'Onghia et al. 2013).

To complicate the picture, there is the finding that 60% of the galaxies in the nearby universe are grand-design, bisymmetric spirals (Elmegreen and Elmegreen 1982; Grosbøl et al. 2004). These galaxies may show evidence of a galaxy companion, suggesting that the perturbations induced by tidal interactions could cause spiral features in disks by creating localized disturbances that grow by swing amplification (Kormendy and Norman 1979; Bot-

tema 2003; Gauthier et al. 2006; D'Onghia et al. 2016; Pettitt et al. 2016). Some studies have been devoted to exploring galaxy models with bar-induced spiral structure (Contopoulos and Papayannopoulos 1980) and spiral features explained by a manifold (Contopoulos and Papayannopoulos 1980; Athanassoula 1992). It is also possible that a combination of these models is needed to describe the observed spiral structure.

A detailed explanation of the spiral structure theory can be found in the "Introduction" of this thesis. The main goal of this chapter is to test whether spiral arms in disk galaxies are static and long-lived. As we discussed before, the nature and longevity of a spiral structure can be tested observationally. In fact, the stationary density wave theory predicts that the age of stars / stellar clusters inside the co-rotation radius increases with increasing distance from the spiral arms, thus we expect to find an age sequence (from young to old) of stellar clusters around the spiral arms.

This work is based on the LEGUS observations obtained with HST (Calzetti et al. 2015). The chapter is organized as follows: The survey and the sample galaxies are described in Section 2.2. The selection of the star cluster samples is presented in Section 2.3. We investigate the spatial distribution together with clustering of the selected clusters in Section 2.4. In Section 2.5, we describe the results and analysis and how we measure the spatial offset of our star clusters across spiral arms. In Section 2.6, we discuss whether the two spiral arms of our target galaxies have the same nature. In Section 2.7, we use a non-LEGUS star cluster catalog to measure the spatial offset of star clusters in M51a, and we present our conclusions in Section 2.8.

2.2 The sample galaxies

Face-on spiral galaxies with prominent spiral structures are interesting candidates to study stationary density wave theory. Therefore, three face-on spiral galaxies, namely NGC 1566, M51a, and NGC 628 were selected from the LEGUS survey for our study. The morphological type, distance, co-rotation radius, and the pattern speed of each galaxy are listed in Table 2.2.1. The UVIS and ACS footprints of the pointings (red and yellow boxes, respectively) overlaid on Digitized Sky Survey (DSS) images of the galaxies are shown in Fig. 2.2.1 together with their HST colour composite mosaics.

2.2.1 NGC 1566

NGC 1566, the brightest member of the Dorado group, is a nearly face-on (inclination = 37.3°, derived from the sizes listed in NED) barred grand-design spiral galaxy with strong spiral structures (Elmegreen et al. 2011). The distance of NGC 1566 in the literature is uncertain and varies between 5.5 and 21.3 Mpc. In this study, we adopted a distance of 18 Mpc from Sabbi et al. (2018) which was determined from the tip of the red giant branch. NGC 1566 has been morphologically classified as an SABbc galaxy because of its intermediate-strength bar. It hosts a low-luminosity active galactic nucleus (AGN) (Combes et al. 2014).

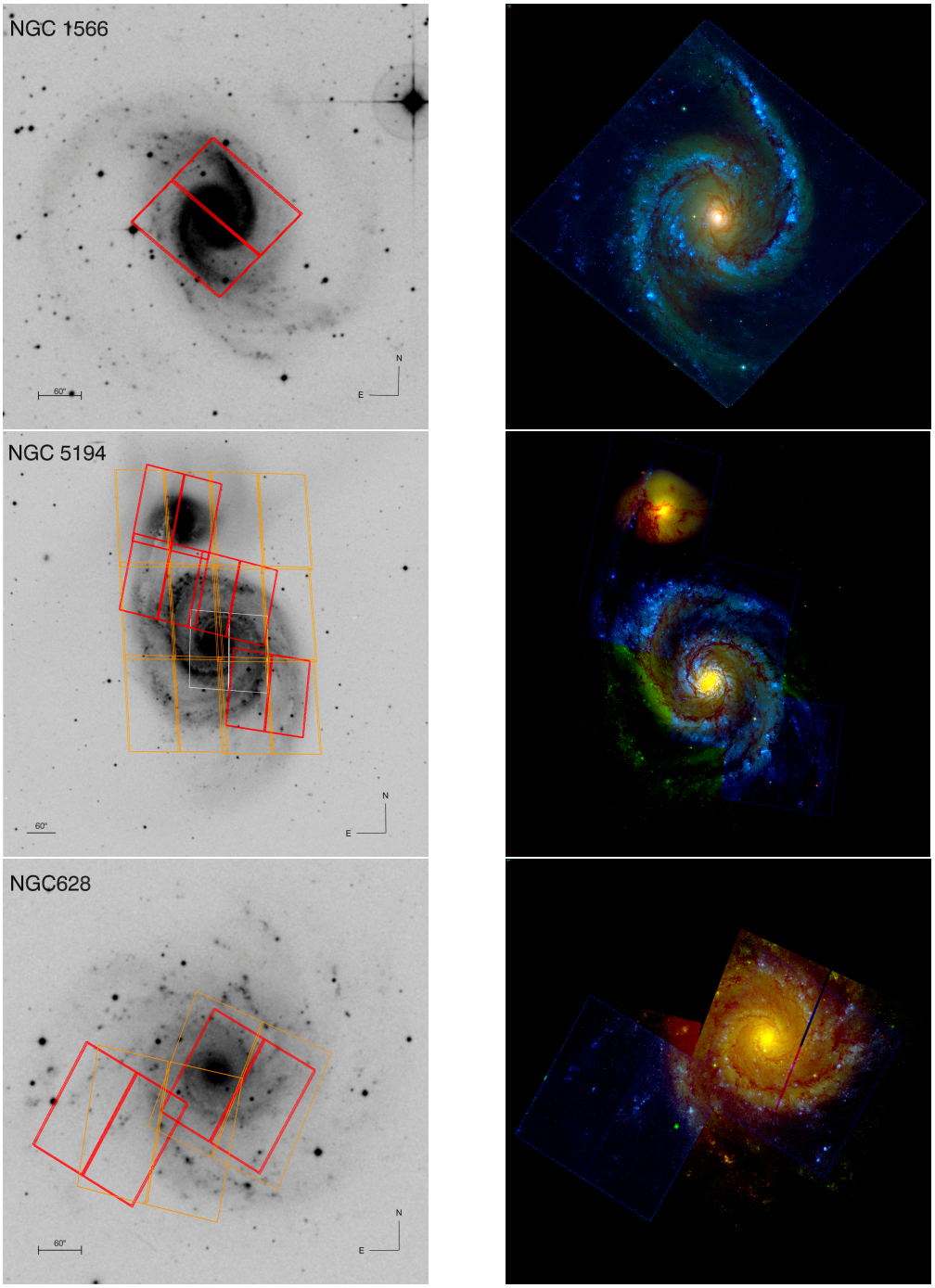

Figure 2.2.1: Left: UVIS (red boxes) and ACS (yellow boxes) footprints of the LEGUS observations on DSS images of the galaxies NGC 1566, M51, and NGC 628 (from top to bottom, respectively). The horizontal bar in the lower left corner denotes the length scale of 60 arcsec. North is up and East to the left. Right: Colour composite images for the same galaxies, constructed from LEGUS imaging in the filters $F275W$ and $F336W$ (blue), $F438W$ and $F555W$ (green), and $F814W$ (red). The central UVIS pointing (white) of M51a was taken from the observations for proposal GO-13340 (PI: S. Van Dyk).

Table 2.2.1: Fundamental properties of our target galaxies.

Galaxy	Morphology	D [Mpc]	$M_\star\,(M_\odot)$	SFR (UV) $(M_\odot\,yr^{-1})$	$\mathrm{R_{cr}}$ [kpc]	Ω_p [$\mathrm{km\,s^{-1}\,kpc^{-1}}$]	Ref
NGC 1566	SABbc	18	2.7×10^{10}	2.026	10.6	23 ± 2	1
M51a	SAc	7.6	2.4×10^{10}	6.88	5.5	38 ± 7	2
NGC 628	SAc	9.9	1.1×10^{10}	3.6	7	32 ± 2	3

Column 1, 2: Galaxy name and morphological type as listed in the NASA Extragalactic Database (NED)

Column 3: Distance
Column 4: Stellar mass obtained from the extinction-corrected B-band luminosity
Column 5: Star formation rate calculated from the GALEX far-UV, corrected for dust attenuation
Column 6: Co-rotation radius
Column 7: Pattern speed
Column 8: References for the co-rotation radii and pattern speeds: 1- Agüero et al. (2004), 2- Zimmer et al. (2004), 3- Sakhibov and Smirnov (2004)
The references for the distance measurement, stellar mass, and SFR can be found in the text.

The star formation rate and stellar mass of NGC 1566 are 2.0 $\mathrm{M_\odot\,yr^{-1}}$ and 2.7 $\times 10^{10}\,M_\odot$, respectively within the LEGUS field of view (Sabbi et al. 2018). Two sets of spiral arms can be observed in NGC 1566. The inner arms connect with the star-forming ring at 1.7 kpc (Smajić et al. 2015), which is covered by the LEGUS field of view (see Fig. 2.2.1, top panel). The outer arms beyond 100 arcseconds (corresponding to 8 kpc) are weaker and smoother than the inner arms.

2.2.2 M51a

M51a (NGC 5194) is a nearby, almost face-on (inclination = $22°$, derived from the sizes listed in NED) spiral galaxy located at a distance of 7.6 Mpc (Tonry et al. 2001). It is a grand design spiral galaxy morphologically classified as SAc with strong spiral patterns. M51a is interacting with a companion galaxy, M51b (NGC 5195). M51a has a star formation rate and a stellar mass of 6.9 $\mathrm{M_\odot\,yr^{-1}}$ and 2.4 $\times 10^{10}\,M_\odot$, respectively (Lee et al. 2009; Bothwell et al. 2009). Five UVIS pointings in total were taken through LEGUS observations: 4 pointings cover the center, the north-east, and the south-west regions of M51a, and one covers the companion galaxy M51b.

2.2.3 NGC 628

NGC 628 (M74) is the largest galaxy in its group. This nearby galaxy is seen almost face-on ($\mathrm{i} = 25.2°$, derived from the sizes listed in NED) and is located at a distance of 9.9 Mpc (Olivares E. et al. 2010). It has no bulge (Cornett et al. 1994) and is classified as a SAc spiral galaxy. Its star formation rate and stellar mass obtained from the extinction-corrected B-band luminosity are 3.6 $\mathrm{M_\odot\,yr^{-1}}$ and 1.1 $\times 10^{10}\,M_\odot$, respectively (Lee et al. 2009; Bothwell et al. 2009). NGC 628 is a multiple-arm spiral galaxy (Elmegreen and Elmegreen 1987) with two well-defined spiral arms. It has weaker spiral patterns than NGC 1566 and M51a (Elmegreen et al. 2011). The LEGUS UVIS observations of NGC 628 consist of one central and one east pointing that were combined into a single mosaic for the analysis.

2.3 Selection of star clusters with different ages

In this study, we made use of star clusters catalog described in Section 1.4.1. We use the age and position of star clusters in our galaxy sample as a tool to find a possible age gradient across the spiral arms predicted by the stationary density wave theory. Therefore, we group star clusters into three different cluster samples according to their ages.

The estimated physical properties of star clusters based on the Yggdrasil deterministic models are inaccurate for low-mass clusters (Krumholz et al. 2015). A comparison between the deterministic approach based on Yggdrasil models and the Bayesian approach with SLUG models presented by Krumholz et al. (2015) suggests that the derived cluster properties are quite uncertain at cluster masses below 5000 $\mathrm{M}_{\odot}$. We adopted the same mass cut-off for NGC 628 and M51a in our analysis. Using the luminosity corresponding to this mass, namely $\mathrm{M_V} = -6$ mag ($\mathrm{m_V}$ = 23.4 and 23.98 mag for NGC 628 and M51a, respectively) results in an age completeness limit of $\leq 200\,\mathrm{Myr}$. In Adamo et al. (2017) and Messa et al. (2018) the magnitude cut at $\mathrm{M_V} < -6$ mag is a more conservative limit than the magnitude limit corresponding to 90% of completeness in the recovery of sources.

NGC 1566 is the most distant galaxy within our LEGUS sample. Due to the large distance of this galaxy, the 90% completeness limit ($\mathrm{m_V}$ = 23.5 mag) is significantly brighter than $\mathrm{M_V} = -6$ mag. Therefore, in order to select star clusters in NGC 1566, we used the 90% completeness limit and a mass cut of 5000 $\mathrm{M}_{\odot}$ for the cluster ages up to 100 Myr and $10^4\mathrm{M}_{\odot}$ for the 100-200 Myr old star clusters (see Fig. 2.3.1). Applying these two criteria reduced our cluster samples from 1573 to 1195 clusters for NGC 1566, from 3374 to 1781 clusters for M51a, and from 1262 to 490 for NGC 628.

Then, we selected three cluster samples of different ages for each galaxy as follows:

- "Young" star clusters: age (Myr) < 10
- "Intermediate-age" star clusters: $10 \leq$ age (Myr) < 50
- "Old" star clusters: $50 \leq$ age (Myr) ≤ 200

The number of star clusters in the "young", "intermediate-age", and "old" samples is shown in Tab. 2.3.1.

Fig. 2.3.1 displays the age-mass diagram of star clusters in NGC 1566, M51a, and NGC 628. The young, the intermediate-age, and the old star cluster samples are shown in blue, green, and red colours, respectively. The excluded star clusters (due to the mass cut) are shown in black. The horizontal and vertical dotted lines show the applied mass cut of 5000 $\mathrm{M}_{\odot}$ and its corresponding completeness limit at a stellar age of 200 Myr, respectively. We have tested our results using different mass cuts as well as removing any constraint on the limiting mass, and we have not observed any significant change in the age distributions of the clusters as a function of azimuthal distances. Thus, the results presented in § 2.5 and § 2.6 are robust against uncertainties in the determination of cluster physical properties.

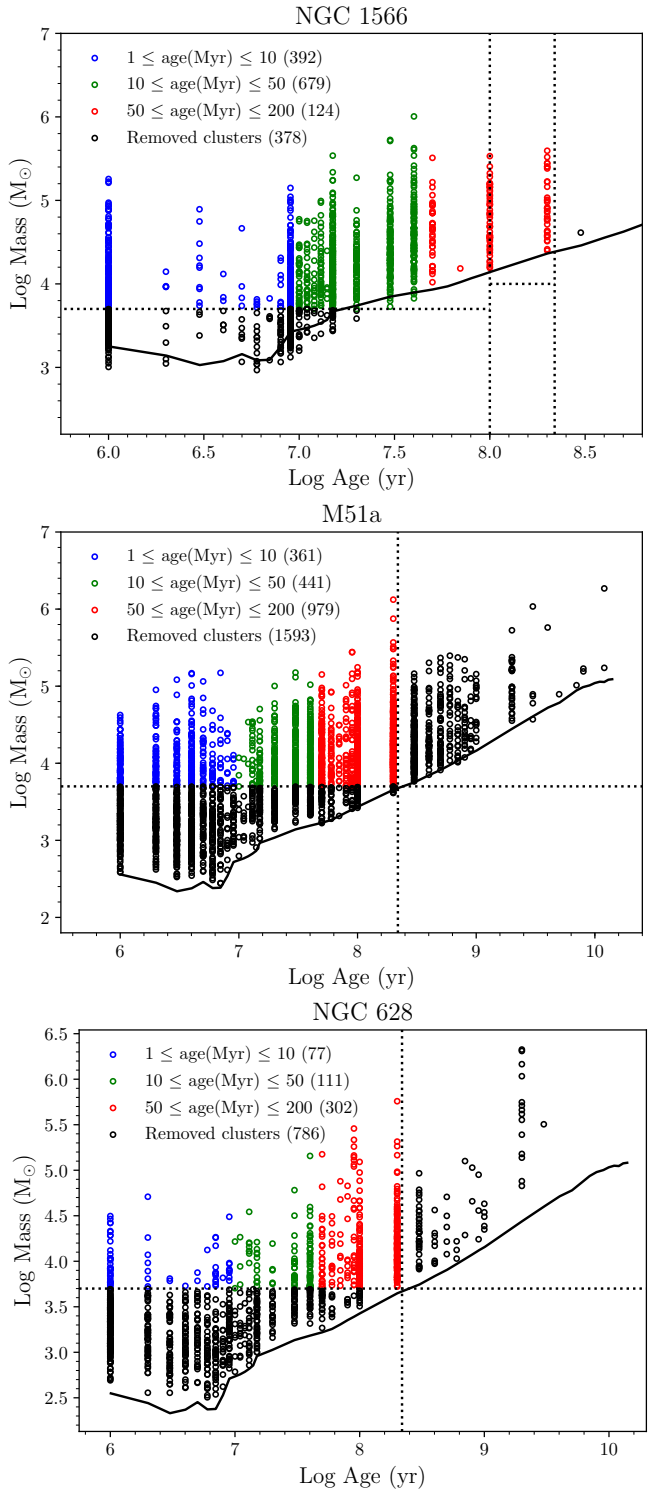

Figure 2.3.1: Distribution of ages and masses of the star clusters (class 1, 2, and 3) in NGC 1566, M51a, and NGC 628. The colours represent different age bins: blue (the young sample), green (the intermediate-age sample), red (the old sample), and black (excluded star clusters). The number of clusters in each sample is shown in parentheses. The horizontal dotted lines in NGC 1566 show the applied mass cut of 5000 $M_{\odot}$ up to the age of 100 Myr and 10^4 $M_{\odot}$ up to the age of 200 Myr. The applied mass cut of 5000 $M_{\odot}$ up to the age of 200 Myr in M51a and NGC 628 are also indicated by horizontal dotted lines. The solid black line shows the 90% completeness limit of 23.5 mag in the V–band in NGC 1566 and the magnitude cut of M_V = -6 mag in M51a, and NGC 628, respectively.

Table 2.3.1: The number of star clusters in the "young", "intermediate-age", and "old" samples in our target galaxies.

Galaxy	age (Myr) $<$ 10	10 $\leq$ age (Myr) $<$ 50	50 $\leq$ age (Myr) $\leq$ 200
NGC 1566	392	679	124
M51a	361	441	979
NGC 628	77	111	302

2.4 Spatial distribution and clustering of star clusters

In Fig. 4.2.1, 4.2.3, and 4.2.2 we plot the spatial distribution of star clusters of different ages in the galaxies NGC 1566, M51a, and NGC 628, respectively. The young, intermediate-age, and old stellar cluster samples are shown in blue, green, and red, respectively. In general, we observe a similar trend in our target galaxies: First, the young and the intermediate-age star clusters mostly populate the spiral arms rather than the interarm regions. This is particularly evident for NGC 1566 and M51a, which show strong and clear spiral structures in young and intermediate-age star clusters. Second, the old star clusters are less clustered and more widely spread compared to the young and intermediate-age star cluster samples.

Our findings are similar to other literature results on the spatial distribution of star clusters of different ages: Dobbs et al. (2017), using LEGUS HST data found that in NGC 1566 the 100 Myr old star clusters clearly trace the spiral arms while in NGC 628 star clusters older than 10 Myr show only weak spiral structures. Chandar et al. (2017), using other HST data observed that M51a shows weak spiral structure in older star clusters (>100 Myr).

Clustering of star clusters has been observationally investigated for a number of local star-forming galaxies (e.g., Efremov 1995; Efremov and Elmegreen 1998). In a detailed study of clustering of the young stellar population in NGC 6503 based on the LEGUS observations, Gouliermis et al. (2015) found that younger stars were more clustered compared to the older ones. Grasha et al. (2015) investigated the spatial distribution of the star clusters in NGC 628 from the LEGUS sample. Their findings confirmed that the degree of the clustering increases with decreasing age. More recently, Grasha et al. (2017a) studied the hierarchical clustering of young star clusters in a sample of six LEGUS galaxies. Their results suggested that the youngest star clusters are strongly clustered and the degree of clustering quickly drops for clusters older than 20 Myr and the galactic shear appears to drive the largest sizes of the hierarchy in each galaxy (Grasha et al. 2017b).

Adopting a similar approach as Grasha et al. (2015), we use the two-point correlation function to test whether or not the clustering distribution of the clusters in our selected age bins shows the expected age dependence. The two–point correlation function $\omega(\theta)$ is a powerful statistical tool for quantifying the probability of finding two clusters with an angular separation θ against a random, non-clustered distribution (Peebles 1980). Here we use the Landy-Szalay (Landy and Szalay 1993) estimator, which has little sensitivity to the

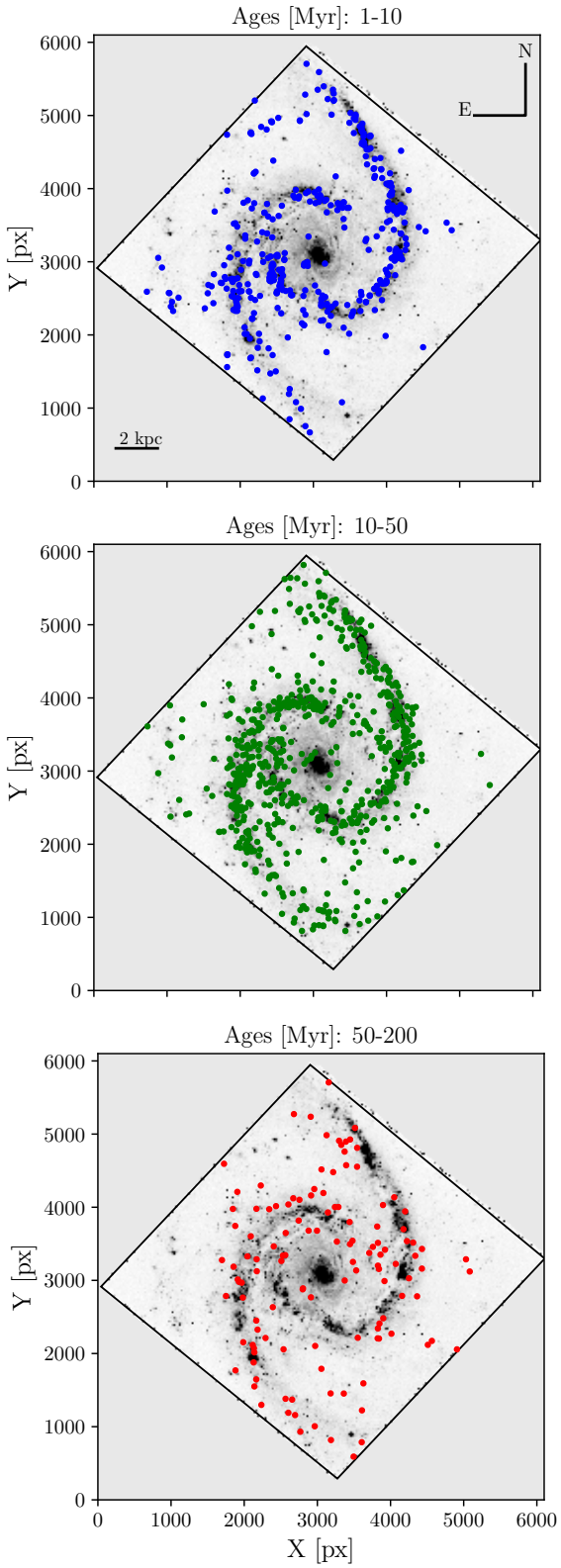

Figure 2.4.1: The spatial distribution of star clusters of different age in the galaxies NGC 1566 superimposed on the B-band images. The blue, green, and red circles show the young (age (Myr) $<$ 10), intermediate-age (10 $\leq$ age (Myr) $<$ 50), and old star clusters (50 $\leq$ age (Myr) $\leq$ 200), respectively. The black outlines show the UVIS footprints. The horizontal bar in the lower left corner denotes a length of 2 kpc. North is up and East to the left.

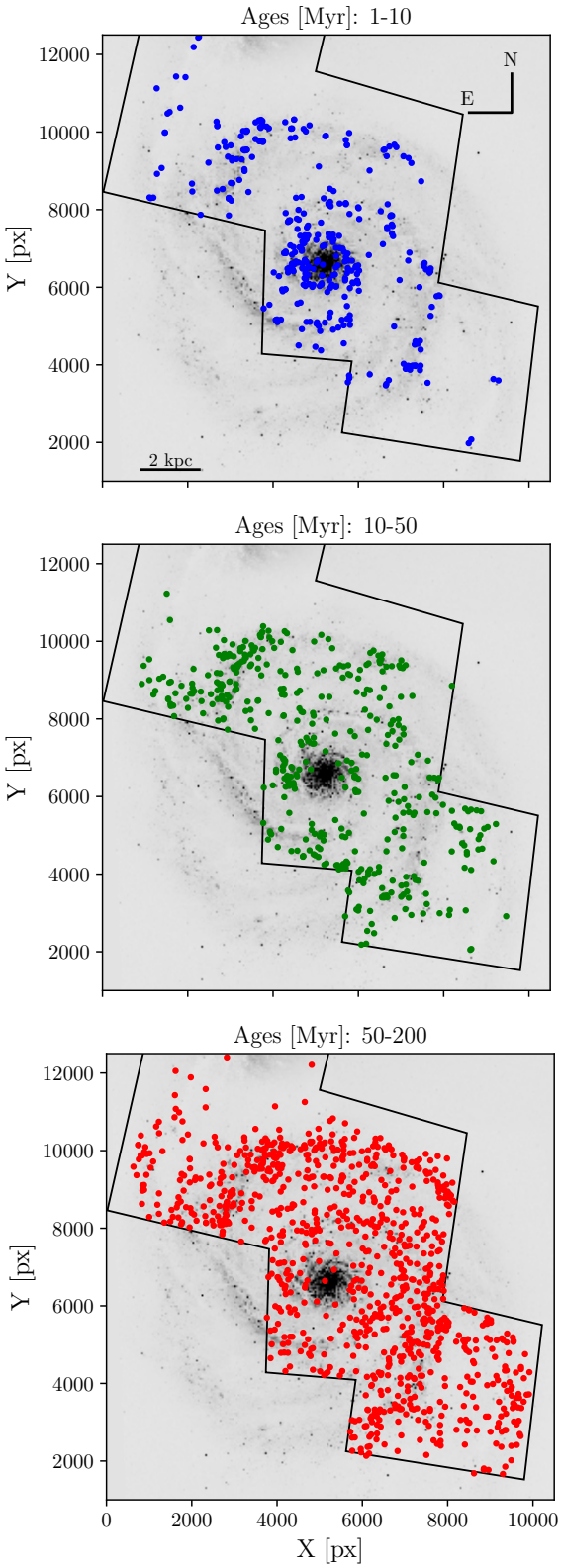

Figure 2.4.2: Same as Fig. 4.2.1 but for M51a.

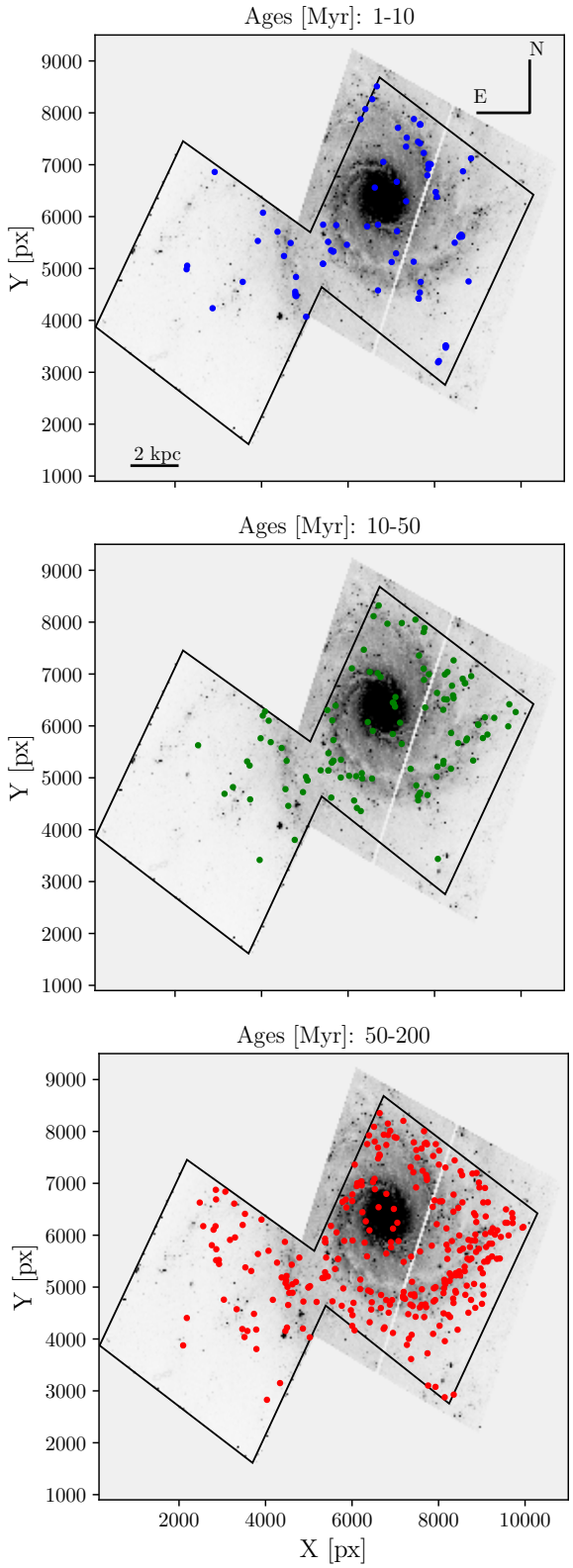

Figure 2.4.3: Same as Fig. 4.2.1 but for NGC 628.

presence of edges and masks in the data:

$$\omega(\theta) = \frac{r(r-1)}{n(n-1)}\frac{DD}{RR} - \frac{(r-1)}{n}\frac{DR}{RR} + 1, \tag{2.1}$$

where n and r are the total number of data and random points, respectively. DD, RR, and DR are the total numbers of data-data, random-random, and data-random pair counts with a separation $\theta \pm \mathrm{d}\theta$, respectively. We construct a random distribution of star clusters that has the same sky coverage and masked regions (e.g., the ACS chip gap) as the images of each galaxy.

Fig. 2.4.4 displays the two-point correlation function for the star clusters in different age bins as defined for our galaxy samples. The blue, green, and red colours represent the young, intermediate-age, and old star cluster samples in each galaxy, respectively. The error bars on the two-point correlation function were estimated using a bootstrapping method with 1000 bootstrap resamples. The general distribution of the star cluster samples in the target galaxies shows a similar trend: Independent of the presence of spiral arms, the young star clusters are highly clustered and show hierarchical structure. The clustering declines as star clusters age and the old star clusters show a non-clustered, smooth distribution.

2.5 Are the spiral arms static density waves?

As discussed in § 3.1, the stationary density wave theory foresees that the age of stellar clusters inside the co-rotation radius increases with increasing distance from the spiral arms. In other words, we expect to find a shift in the location of stellar clusters with different ages.

In order to test whether the distribution of star clusters of different ages in our target galaxies agrees with the expectations from the stationary density wave theory, we need to quantify the azimuthal offset between star clusters of different ages.

2.5.1 Spiral arm ridge lines definition

First of all, we need to locate the spiral arms of our galaxy sample. We wish to define a specific location in each spiral arm so we can measure the relative positions of the star clusters in a uniform way. We use the dust lanes for this purpose because they are narrow and well-defined in optical images.

As gas flows into the potential minima of a density wave, it gets compressed and forms dark dust lanes in the inner part of the spiral arms, where star formation is then likely to occur (Roberts 1969). We have used the B-band images for this purpose since most of the emission is due to young OB stars and dark obscuring dust lanes can be better identified in this band.

To better define the average positions of the dust lanes, we used a Gaussian kernel (with a 10 pixels sigma) to smooth the images, reduce the noise, and enhance the spiral structure.

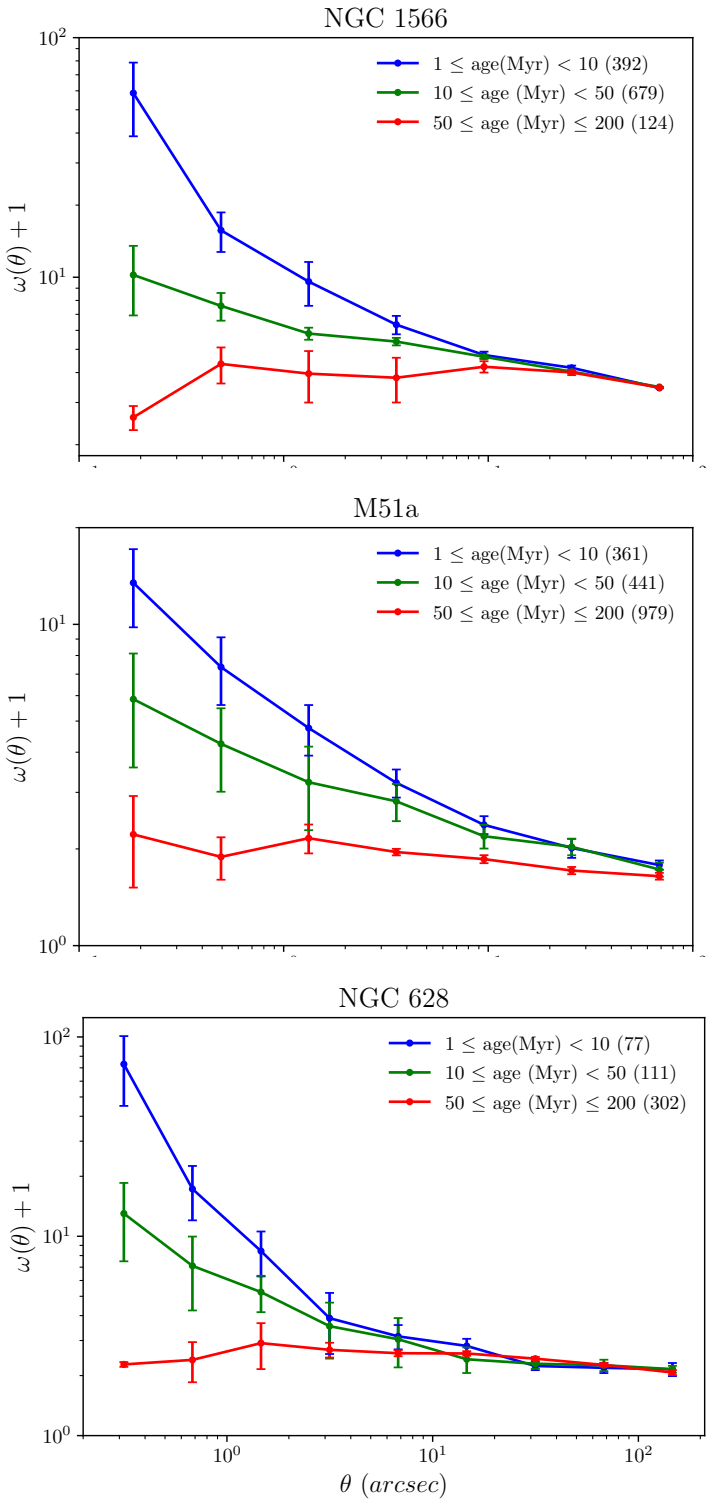

Figure 2.4.4: Two-point correlation function for the star cluster samples of different ages as a function of angular distance (arcseconds) in NGC 1566, M51a, and NGC 628. The young, intermediate-age, and old star cluster samples are shown in blue, green, and red, respectively. The error bars were computed based on a bootstrapping method. The number of star clusters in each age bin are listed in parentheses.

In the smoothed images the dust lanes are clearly visible as dark ridges inside the bright spiral arms. We defined these dark spiral arm ridge lines manually. For the remainder of this paper, we refer to the southern arm and northern arm as "Arm 1" and "Arm 2", respectively. Fig. 3.3.1 presents the defined spiral arm ridge lines (red lines) overplotted on the smoothed B-band images of NGC 1566, M51a, and NGC 628.

2.5.2 Measuring azimuthal offset

Knowing the position of star clusters and spiral arm ridge lines in our target galaxies allowed us to measure the azimuthal distance of a star cluster from its closest spiral arm, assuming that it rotates on a circular orbit.

We limited our analysis to the star clusters located in the disk where spiral arms exist. The disk of a galaxy can be defined by its rotation curve. The rotational velocity increases when moving outwards from the central bulge–dominated part and becomes flat in the disk-dominated part of the galaxy. We derived a radius of 2 kpc for the bulge-dominated part of our galaxies using the rotation curves of Korchagin et al. (2000) for NGC 1566, Sofue (1996, 1997) for M51a, and Combes and Becquaert (1997) for NGC 628. Furthermore, we limited our analysis to star clusters located inside the co-rotation radius. If stationary density waves are the dominant mechanism driving star formation in spiral galaxies we expect to find an age gradient from younger to older clusters inside the co-rotation radius. The bulge-dominated region and co-rotation radius of each galaxy are shown in Fig. 3.3.1. The adopted co-rotation radii of the galaxies are listed in Tab. 2.2.1.

Fig. 2.5.2 (left panels) shows the normalized distribution of the azimuthal distance of star clusters in the three age bins from their closest spiral arm ridge line in NGC 1566, M51a, and NGC 628. The error bars in each sample were calculated by dividing the square root of the number of clusters in each bin by the total number of clusters. We note that an azimuthal distance of zero degrees shows the location of the spiral arm ridge lines and not the center of the arms. Positive (negative) azimuthal distributions indicate that a cluster is located in front of (behind) the spiral arm ridge lines. Blue, green, and red colorus represent the young, intermediate-age, and old star cluster samples, respectively.

Fig. 2.5.2 (right panels) shows the cumulative distribution function of star clusters as a function of the azimuthal distance. In order to test whether the samples come from the same distribution, we used a two–sample Kolmogorov–Smirnov test (hereafter K-S test). Since we aim at finding the age gradient in front of the spiral arms, the K-S test was only calculated for star clusters with positive azimuthal distances. The probability that two samples are drawn from the same distribution (p-values) and the maximum difference between pairs of cumulative distributions (D) are listed in Tab 2.5.1.

In the case of NGC 1566 (Fig. 2.5.2, top), we see that the young and intermediate-age star cluster samples are peaking close to the location of the spiral arm ridge lines (azimuthal distance of 0-5 degrees) while the old sample peaks further away from the ridge lines (azimuthal distances of 5-10 degrees). The derived p-values are lower than the test's significance level (0.05) of the null hypothesis, i.e., that the two samples are drawn from the

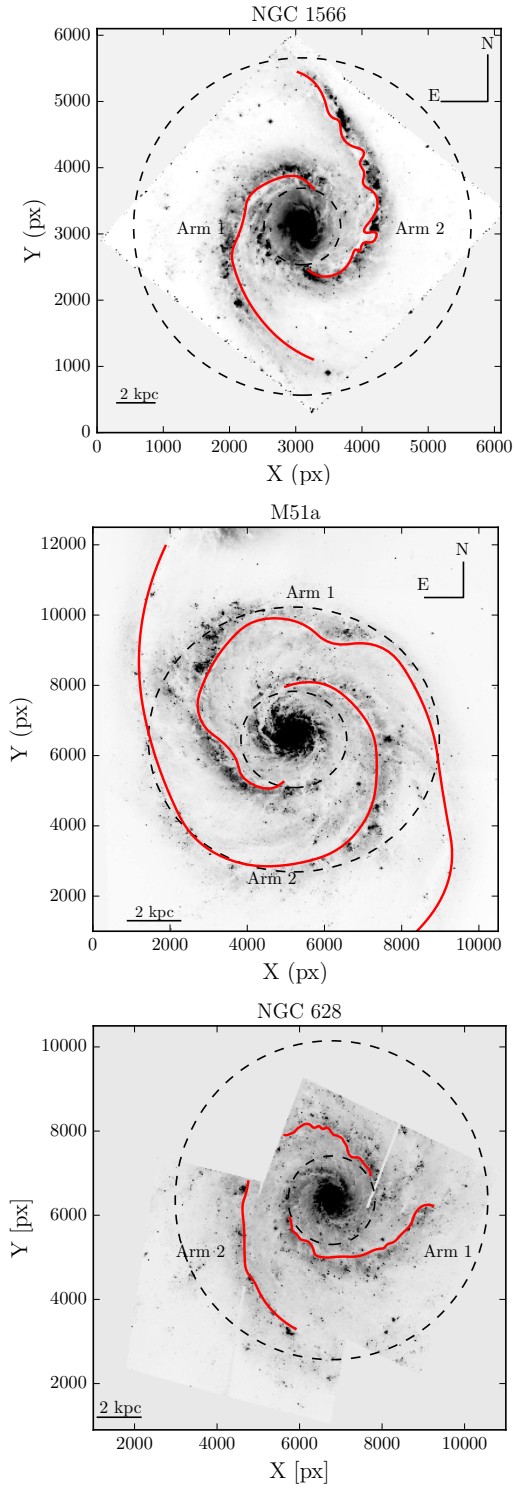

Figure 2.5.1: The location of spiral arm ridge lines of NGC 1566, M51a, and NGC 628. We refer to the southern arm and northern arm as "Arm 1" and "Arm 2", respectively. The two black dashed circles in each panel mark the onset of the bulge and the location of the co-rotation radius of the galaxies. The horizontal bar in the lower left corner denotes a length scale of 2 kpc. North is up and East to the left.

Table 2.5.1: The maximum difference between pairs of cumulative distributions (D) of azimuthal distance of star clusters and the probability that two samples are drawn from the same distribution (p-values) of the two sample K-S test in NGC 1566, M51a, and NGC 628.

Galaxy	Young & Intermediate–age		Young & Old		Intermediate–age & Old	
	D	p–value	D	p–value	D	p–value
NGC 1566	0.15	3.78×10^{-3}	0.31	2.88×10^{-5}	0.26	6.19×10^{-5}
M51a	0.15	0.10	0.13	0.10	0.17	2.4×10^{-3}
NGC 628	0.21	0.49	0.17	0.47	0.19	0.10

same distribution. As a consequence, our three star cluster samples are unlikely to be drawn from the same population. A clear age gradient across the spiral arms can be observed in NGC 1566, which is in agreement with the expectation from stationary density wave theory. The existence of such a pattern supports the picture of an age sequence in the model of a grand–design spiral galaxy and a barred galaxy suggested by Dobbs and Pringle (2010); Gouliermis et al. (2017).

No obvious age gradient from younger to older age is seen in the azimuthal distributions of the star cluster samples in M51a (Fig. 2.5.2, middle). What is remarkable here is that the older star clusters are located closer to the spiral arm ridge lines than the young and intermediate-age star clusters. The K-S test indicates that the probability that the young star cluster sample is drawn from the same distribution as the intermediate-age and old star cluster samples is more than 10%. The derived p-value for the intermediate–age and old cluster samples is lower than the significance level of the K-S test and rejects the null hypothesis that the two samples are drawn from the same distribution. The lack of an age pattern is consistent with the observed age trend for an interacting galaxy, modeled based on M51a, suggested by Dobbs and Pringle (2010). Our result is compatible with a number of observational studies have found no indication for the expected spatial offset from the stationary density wave theory in M51a (Scheepmaker et al. 2009; Kaleida and Scowen 2010; Foyle et al. 2011; Schinnerer et al. 2017).

There is no evident trend in the azimuthal distribution of star clusters in NGC 628 (Fig. 2.5.2, bottom). The majority of the young star clusters tends to be located further away from the ridge lines (azimuthal distance of 20-25 degrees). The calculated p-values from the K-S test are larger than 0.05, which suggests weak evidence against the null hypothesis. As a result, the three young, intermediate-age, and old star cluster samples are drawn from the same distribution. The absence of an age gradient across the spiral arms in NGC 628 is consistent with a simulated multiple arm spiral galaxy by Grand et al. (2012a).

2.6 The origin of two spiral arms

An observational study by Egusa et al. (2017), based on measuring azimuthal offsets between the stellar mass (from optical and near-infrared data) and gas mass distributions (from CO and HI data) in two spiral arms of M51a, suggests that the origin of these spiral arms differs.

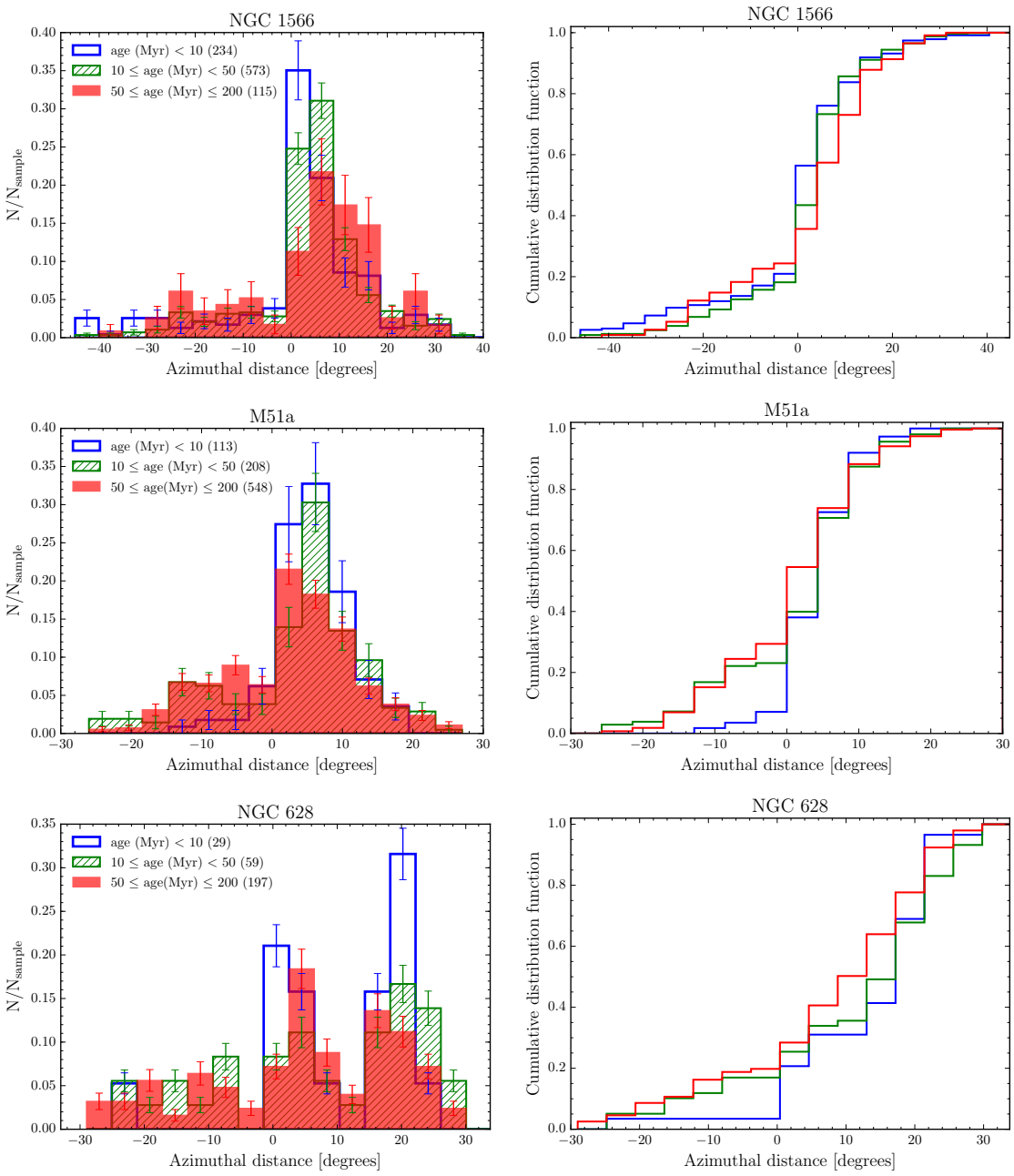

Figure 2.5.2: The normalized distribution of azimuthal distance (in degrees) of the star cluster samples from their closest spiral arm (left panels) and the cumulative distribution function of star clusters of different ages as a function of the azimuthal distances (in degrees) in NGC 1566, M51a, and NGC 628. The young (< 10 Myr), intermediate-age (10-50 Myr), and old star cluster samples (50-200 Myr) are shown in blue, green, and red, respectively. The number of star clusters located in the disk and inside the co-rotation radius of each galaxy is listed in parentheses.

One spiral arm obeys the stationary density wave theory while the other does not.

In another recent study of M51a, Chandar et al. (2017) quantified the spatial distribution of star clusters with different ages relative to different segments of the two spiral arms of M51a traced in the 3.6 μm image. They observed a similar trend for the western and eastern arms: the youngest star clusters (< 6 Myr) are found near the spiral arm segments, and the older clusters (100-400 Myr) show an extended distribution.

In this Section, we test whether measuring the azimuthal offset of star cluster samples from each spiral arm individually leads to different results. We assume that a star cluster whose distance from Arm 1 is smaller than its distance from Arm 2 belongs to Arm 1 and vice versa.

Fig. 2.6.1 shows the normalized distribution of ages of star clusters associated with Arm 1 (shown in red) and Arm 2 (shown in blue) in each of the galaxies. No significant differences between the age distribution of star clusters belonging to the two spiral arms in our target galaxies can be observed. Also, the K-S test indicates that the age distributions of star clusters relative to Arm 1 and Arm 2 in each galaxy are drawn from the same population.

In Fig. 2.6.2 we compare the normalized azimuthal distribution of the three young, intermediate-age, and old star cluster samples relative to Arm 1 (left panels) and Arm 2 (right panels) in our target galaxies. As before, our analysis was limited to the star clusters positioned in the disk and inside the co-rotation radius of our target galaxies.

The upper panels of Fig. 2.6.2 exhibit a noticeable age gradient across both spiral arms of NGC 1566. The young star clusters are highly concentrated towards the location of Arm 1 and Arm 2 while the older ones are peaking further away from the two spiral arms.

The second row panels of Fig. 2.6.2 show the azimuthal distance of star cluster samples across the two arms of M51a. This galaxy displays an offset in the location of young and old star clusters across Arm 1. The young star clusters culminate close to Arm 1 (at azimuthal distances of 2-6 degrees) while the old ones are positioned further away (at azimuthal distances of 6-10 degrees). Even though M51a shows an age gradient across the Arm 1 at first glance, the K-S test does not imply significant differences between the young and old star cluster samples (all derived p-values are larger than the test's significance level). We do not observe any shift in the azimuthal distribution of the star cluster samples across Arm 2 in M51a.

In the case of NGC 628, no obvious age gradient across Arm 1 and Arm 2 is observed (the lower panels of Fig. 2.6.2). It is important to note that our results are inconclusive for the young star clusters associated with Arm 2 due to small number statistics. Hence, we also explored the change in the azimuthal distribution of the star clusters by including clusters with masses < 5000 $M_{\odot}$ and ages > 200 Myr. The observed differences are not significant and the general trend is the same as before.

Thus, measuring the azimuthal distance of the star clusters from the two individual spiral arms in each galaxy suggests that the two spiral arms of our target galaxies may have the same physical origin and the star formation proceeded in both arms in a similar fashion.

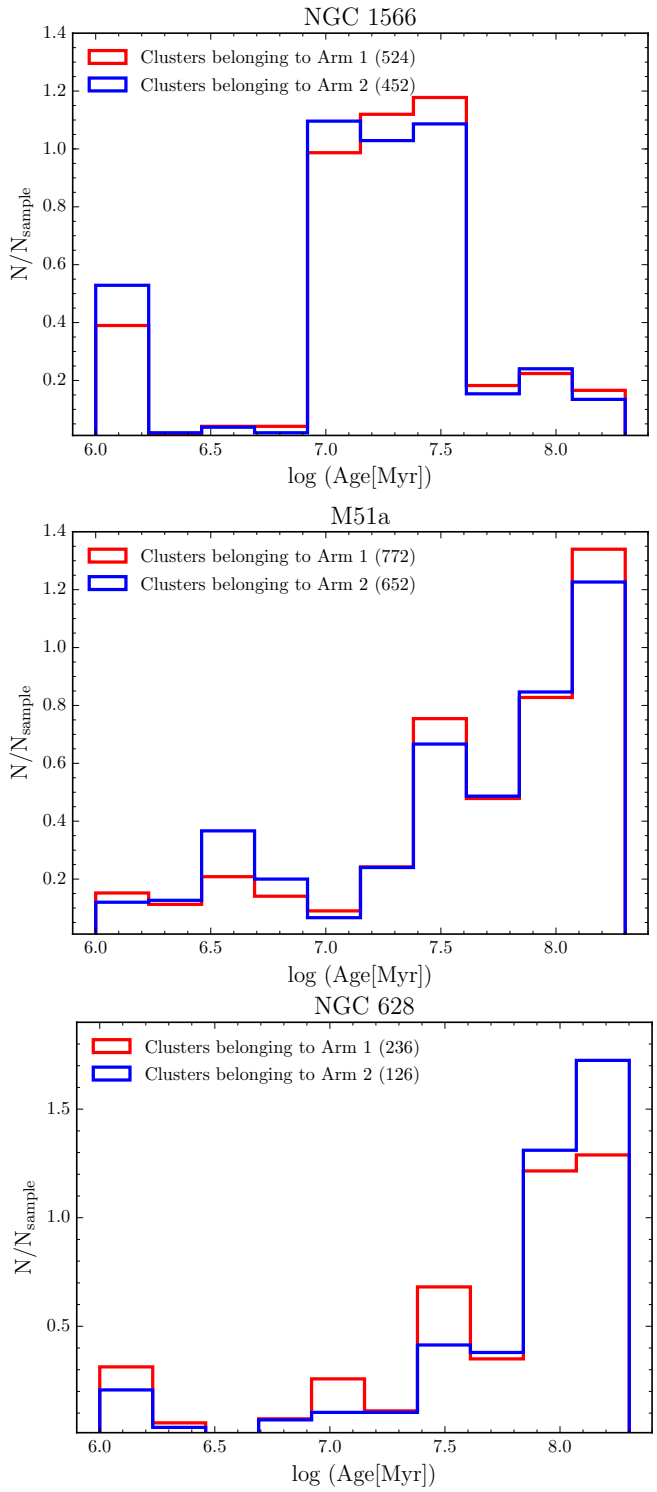

Figure 2.6.1: The distribution of the age of star clusters associated with Arm 1 (red) and Arm 2 (blue) in NGC 1566, M51a, and NGC 628. The number of star clusters relative to the Arm 1 and Arm 2 is listed in parentheses.

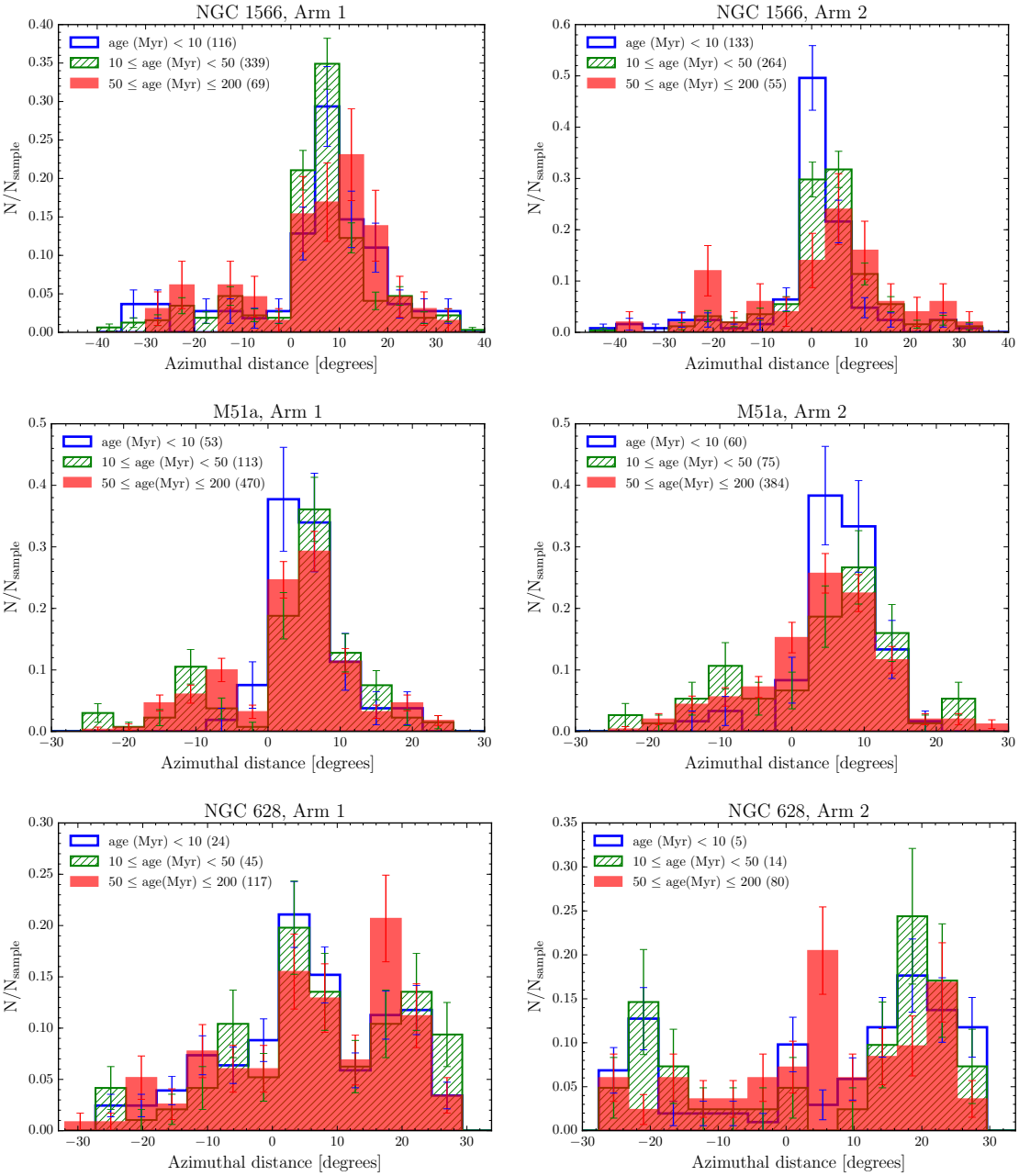

Figure 2.6.2: The normalized distribution of azimuthal distance (in degrees) of the star cluster samples belonging to Arm 1 (left panels) and Arm 2 (right panels) in NGC 1566, M51a, and NGC 628. Blue, green, and red colorus present the young (< 10 Myr), intermediate-age (10-50 Myr), and old star cluster samples (50-200 Myr), respectively. The number of star clusters corresponding to Arm 1 and Arm 2 is listed in parentheses. The error bars in each sample were calculated by dividing the square root of the number of clusters in each bin by the total number of clusters.

2.7 Comparison with the non-LEGUS cluster catalog of M51

In this Section, we use the Chandar et al. (2016) catalog to measure the azimuthal offsets of star clusters with different ages in M51a and to compare the results with our analysis based on the LEGUS catalog. We caution that the south-eastern region of M51a is not covered by the LEGUS observations. We also investigated whether our results are biased due to the absence of star clusters from that region.

Chandar et al. (2016) provided a catalog of 3816 star clusters in M51a based on the same $UBVI$ filters as LEGUS observations together with Hα filter (GO-10452, PI: S. Beckwith) and HST WFC2/ F336W filters (GO- 10501, PI: R. Chandar, GO-5652, PI: R. Kirshner, and GO-7375, PI: N. Scoville). Messa et al. (2018) compared the age distributions of star clusters in common between the LEGUS and Chandar et al. (2016) catalog. They observed that a large number of young star clusters (age $<$ 10 Myr) in Chandar et al. (2016) have a broad age range (age: 1-100 Myr) in the LEGUS catalog. They argued that the discrepancies in the estimated ages are due to the use of different filter combinations. In addition to the $UBVI$ filters used for SED fitting, Messa et al. (2018) used the UV broad-band. Their standard method aims at recovering high-quality physical properties of star clusters by using two data points below the Balmer break (λ $<$ 4000 Å). Chandar et al. (2016) took advantage of the Hα narrow-band emission from ionized gas by young massive stars to detect the young stellar population in the star clusters.

In Fig. 2.7.1, we show the distribution of ages and masses of star clusters in M51a from the Chandar et al. (2016) catalog. In order to be able to compare our results, we considered a mass–limited sample with masses $>$ 5000 $M_{\odot}$ and ages $<$ 200 Myr and selected the same age bins as before: The young ($<$ 10 Myr), intermediate-age (10-50 Myr), and old star cluster samples (50-200 Myr).

In Fig. 2.7.2, we plot the spatial distribution of the young, intermediate-age, and old star clusters based on the Chandar et al. (2016) catalog in M51a. As we can see, M51a displays a very clear and strong spiral pattern in the young star clusters. The intermediate-age star clusters tend to be located along the spiral arms while the old ones are more scattered and populate the inter-arm regions. Recently, Chandar et al. (2017) using the Chandar et al. (2016) catalog found that the youngest star clusters ($<$ 6 Myr) are concentrated in the spiral arms (defined based on 3.6 μm observations). The older star clusters (6-100 Myr) are also found close to the spiral arms but they are more dispersed, and the spiral structure is not clearly recognizable in older star clusters ($>$ 400 Myr).

In order to quantify the possible spatial offset in the location of the three young, intermediate-age, and old star cluster samples from the Chandar et al. (2016) catalog across the spiral arms, we computed the normalized azimuthal distribution and corresponding cumulative distribution function of the star cluster samples in Fig. 2.8.1. We applied our analysis only to the star clusters positioned in the disk and inside the co-rotation radius of M51a (2.0-5.5 kpc). Our result demonstrates that the three young, intermediate-age, and old star cluster samples peak at an azimuthal distance of 6 degrees from the location of the spiral arm ridge lines. We observe no obvious offsets between the azimuthal distances of the three

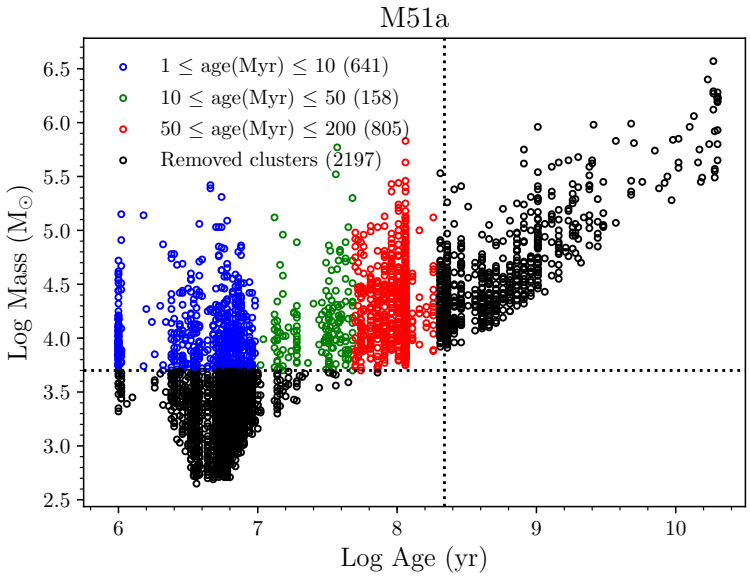

Figure 2.7.1: The distribution of ages and masses of the 3816 star clusters in M51a, based on the Chandar et al. (2016) catalog. The young (<10 Myr), intermediate-age (10-50 Myr), and old (50-200 Myr) star clusters are shown in blue, green, and red, respectively. The black points indicate excluded star clusters due to the applied mass cut and the imposed completeness limit. The number of clusters in each sample is listed in parentheses. The horizontal and vertical dotted lines show the applied mass cut of 5000 $M_\odot$ and the corresponding detection completeness limit of 200 Myr, respectively.

star cluster age samples in M51a. Chandar et al. (2017), using the same cluster catalog, quantified the offset between the molecular gas (from PAWS and HERACLES) and young (<10 Myr) and intermediate-age (100-400 Myr) star clusters in the inner (2-2.5 kpc) and outer (5-5.5 kpc) annuli of the spiral arms. They found that in the inner annuli the young star clusters show an offset of 1 kpc from the molecular gas while there is no offset between the molecular gas and young and old star clusters in the outer portion of the spiral arms. Also, they observed that the star clusters with different ages peak around spiral arms and the width of the distribution increases with the age of star clusters.

Adopting the Chandar et al. (2016) catalog, we found that there is no noticeable age gradient across the spiral arms of M51a, which is in agreement with our finding based on the LEGUS star cluster catalog.

2.8 DISCUSSION AND CONCLUSIONS

The stationary density wave theory predicts that the age of star clusters increases with increasing distance away from the spiral arms. Therefore, a simple picture of the stationary density wave theory leads to a clear age gradient across the spiral arms. In this study, we are testing the theory that spiral arms are static features with constant pattern speed. For this

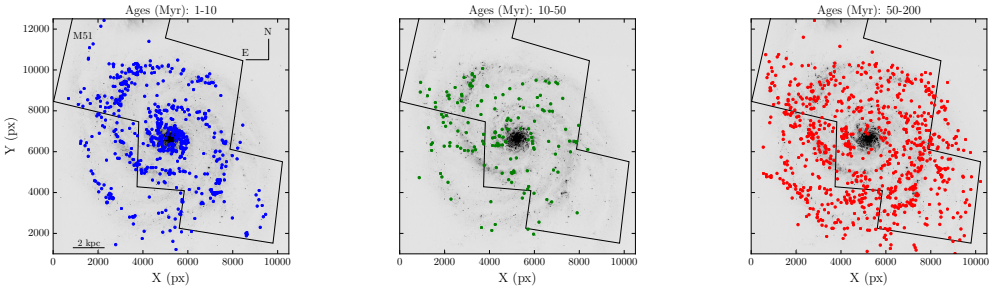

Figure 2.7.2: The spatial distribution of the young (blue), intermediate-age (green), and old (red) star clusters in M51a taken from the Chandar et al. (2016) catalog. The black outlines show the area covered by the LEGUS observations. The horizontal bar indicates the length of 2 kpc, corresponding to 54″. North is up and East to the left.

purpose, we use the age and position of star clusters relative to the spiral arms.

We use high-resolution imaging observations obtained by the LEGUS survey (Calzetti et al. 2015) for three face-on LEGUS spiral galaxies, NGC 1566, M51a, and NGC 628. We measured the azimuthal distance of the LEGUS star clusters from their closest spiral arm to quantify the possible spatial offset in the location of star clusters of different ages (< 10 Myr, 10-50 Myr, and 50-200 Myr) across the spiral arms. We found that the nature of spiral arms in our target galaxies is not unique. The main results are summarized as follows:

- Our detailed analysis of the azimuthal distribution of star clusters indicates that there is an age sequence across spiral arms in NGC 1566. NGC 1566 shows a strong bar and bisymmetric arms typical of a massive self-gravitating disk (D'Onghia 2015). We speculate that when disks are very self-gravitating the bar and the two–armed features dominate a large part of the galaxy, producing an almost constant pattern speed. The observed trend is also in agreement with what was found by Dobbs and Pringle (2010) in simulations of a grand design and a barred spiral galaxy.
- We find no age gradient across the spiral arms of M51a. This galaxy shows less strong arms and a weaker bar and hence a less self-gravitating disk. The absence of an age sequence in M51a indicates that the grand-design structures of this galaxy are not the result of a steady-state density wave, with a fixed pattern speed and shape, as in the early analytical models. More likely, the spiral is a density wave that is still changing its shape and amplitude with time in reaction to the recent tidal perturbations induced by M51b. A possible mechanism to explain the formation and presence of grand-design structures in spiral galaxies is an interaction with a nearby companion (Toomre and Toomre 1972; Kormendy and Norman 1979; Bottema 2003). Since such an interaction is obviously occurring in M51a, tidal interactions could be the dominant mechanism for driving its spiral patterns. Dobbs and Pringle (2010) simulated M51a with an interacting companion (M51b), and observed no age gradient across the tidally induced grand–design spirals arms. Our findings are consistent with the results of several other observational studies, which did not find age gradients as expected from the spiral density wave theory in M51a (Scheepmaker et al. 2009; Kaleida and Scowen

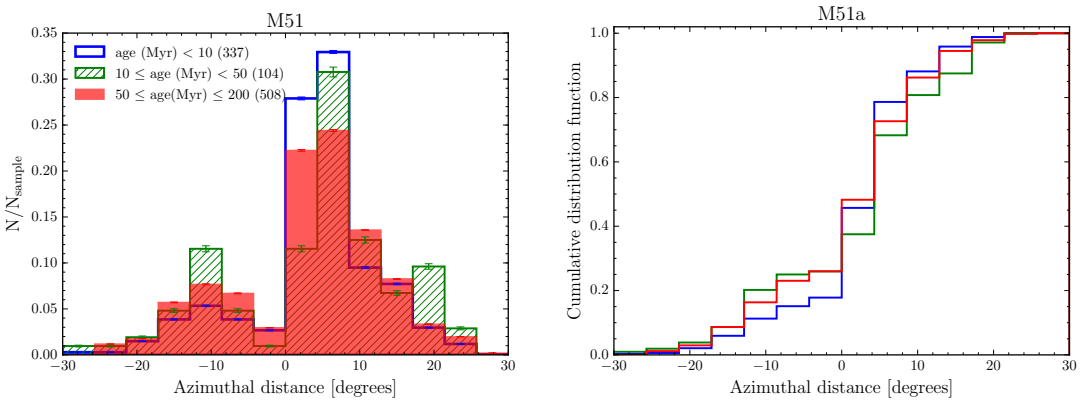

Figure 2.8.1: The normalized azimuthal distribution (top) and the cumulative distribution function as a function of the azimuthal distance (bottom) of three star cluster samples in M51a, based on the Chandar et al. (2016) catalog. The young, intermediate-age, and old star clusters are shown in blue, green, and red, respectively. The number of star clusters in each age bin (located in the disk and inside the co-rotation radius of M51a) is listed in parentheses. The error bars in each sample were calculated by dividing the square root of the number of clusters in each bin by the total number of clusters.

2010; Foyle et al. 2011; Schinnerer et al. 2017).

- NGC 628 is a multiple-arm spiral galaxy with weak spiral arms consistent with a pattern speed decreasing with radius and multiple co-rotation radii. In this case, we find no significant offset among the azimuthal distributions of star clusters with different ages, which is consistent with the swing amplification theory. The lack of such an age offset is in agreement with an earlier analysis of NGC 628 (Foyle et al. 2011), and consistent with the spatial distribution of star clusters with different ages in the simulated multiple-arm spiral galaxy by Grand et al. (2012a).

3

A Spatially-resolved, Multi-wavelength Study of the Lopsided Spiral Galaxy NGC 3344

This chapter was submitted for publication in MNRAS as F.Shabani et al., "A Spatially-resolved, Multi-wavelength Study of the Spiral galaxy NGC 3344 ".

3.1 Introduction

In this chapter and the next one of this thesis, we present a new study of lopsidedness in the distribution of star clusters in disk galaxies, particularly along the two main spiral arms, and investigate whether this asymmetry is reflected in the star formation or stellar mass distribution of the two spiral arms in the host galaxy. For a detailed explanation of lopsidedness in galaxies see Section 1.3.

One approach to measuring the star-formation rate (SFR) and stellar mass surface density across a galaxy is to use a pixel-by-pixel spectral energy distribution (SED) fitting techniques (Bothun 1986; Abraham et al. 1999; Welikala et al. 2008; Zibetti et al. 2009; Wuyts et al. 2012; Sorba and Sawicki 2015, 2018; Abdurro'uf and Akiyama 2017; Abdurro'uf 2018; Williams et al. 2018). Nowadays, the availability of extensive photometric surveys, covering the wavelength range from UV to infrared (IR), enables us to construct spatially resolved SFR and stellar mass surface density maps of a galaxy and study its star formation history on a sub-kpc scale.

There is a remarkable number of different studies in the literature based on photometric pixel-by-pixel SED fitting. For instance, Zibetti et al. (2009) developed a pixel-by-pixel SED fitting technique based on the observed colours of a galaxy to construct spatially resolved

stellar mass surface density maps of nine spirals and one elliptical galaxy. They observed that the prominent spiral arms are somewhat smoothed out in these maps. They compared the total resolved stellar mass (obtained by integrating the pixel-by-pixel maps) with the unresolved stellar mass (obtained from the total light of each galaxy) and found that in galaxies with strong dust lanes, the total, integrated light leads to underestimates of up to 40% in the total stellar mass.

Recently, Abdurro'uf and Akiyama (2017) derived the spatially resolved SFR and stellar mass surface density maps of 93 local massive spiral galaxies located at $0.01<z<0.02$, using a pixel-by-pixel SED fitting method, to examine the relationship between their SFR and stellar mass surface density on sub-kpc scales. They found a linear relationship between the local surface density of the SFR and stellar mass, which becomes flat at high stellar mass surface densities. They also investigated the variation of the specific star formation rate, the SFR normalized by stellar mass (sSFR), in more massive and less massive galaxies, and also barred and non-barred galaxies. Their findings suggest that more massive galaxies have lower sSFR values compared to less massive galaxies. Also, barred galaxies have lower sSFR in the inner regions than non-barred, while in the outer regions they have a similar sSFR.

More recently, Williams et al. (2018) studied the star formation law (the relation between SFR and gas content) on sub-kpc scales of the spiral galaxy M33. They used different SFR indicators including the total infrared luminosity, a combination of $FUV+24\mu$m emission, and the pixel-by-pixel SED fitting tool MAGPHYS (da Cunha et al. 2008) to construct a spatially resolved SFR surface density map of M33. They found that the SFR derived from the total infrared luminosity is lower compared to the other two measures due to the unobscured contributions to the SFR that is missing when using just the total infrared luminosity. Also, the SFR determined from a combination of $FUV+24\mu$m returns a lower SFR surface density than those computed with the MAGPHYS code, because MAGPHYS treats many HII regions as starburst-like. Afterwards, Williams et al. (2018) combined the spatially resolved SFR surface density map derived from the MAGPHYS code in combination with HI and CO gas maps. Their results suggest that on sub-kpc scales, the gas and SFR surface density is linearly correlated but with a higher exponent than the power-law relating SFR and total gas.

In this chapter, we use NGC 3344 as a test bench for our SED fitting method, whose aim is to recover the distribution of SFR and stellar mass surface density across the spiral arms of a galaxy. We study the inner region (5.5×5.5 kpc^2) of the face-on, multi-arm spiral galaxy NGC 3344 located at a distance of 6.9 Mpc (Verdes-Montenegro et al. 2000). NGC 3344 has been morphologically classified as a SABbc galaxy. It exhibits two star-forming ring-like features at galactocentric radii of 1 and 7 kpc with a small bar within the inner ring. The center of the outer ring is shifted to the east by 18″ with respect to the center of the galaxy (Verdes-Montenegro et al. 2000). NGC 3344 is a relatively isolated spiral galaxy, with its nearest neighbor being NGC 3274 located at a distance of 446 kpc (Verdes-Montenegro et al. 2000). It has a UV-based star formation rate and a stellar mass of $0.86\,\mathrm{M}_\odot\mathrm{yr}^{-1}$ and $5\times10^9\mathrm{M}_\odot$, respectively (Lee et al. 2009; Bothwell et al. 2009).

The layout of this chapter is as follows: in § 3.2, we present an overview of the data, including imaging data as well as the star cluster catalog. In § 3.3, we define the spiral arms

of the galaxy and we investigate the spatial distribution of the star clusters with different ages throughout the inner part of the galaxy. We describe the details of the pixel-by-pixel SED fitting method in § 3.4. § 3.5 contains the maps of galaxy's key parameters derived from the SED fitting code. We also test whether the derived parameters depend on the choice of imaging data from different surveys. In § 3.6, we study the radial dependence of the derived parameters. We compare our derived SFR surface density map with the different star formation tracers in § 3.7 and finally, we summarize our results in § 4.5.

3.2 Overview of the data

3.2.1 Imaging data

In this study, we use an imaging dataset that spans a broad range of wavelengths from UV to IR (see Tab. 3.4.1).

The UV data of NGC 3344 in the FUV (1516Å) and NUV (2267Å) were obtained with the Galaxy Evolution Explorer (GALEX, Morrissey et al. 2007)[1] between April 19, 2004 and March 19, 2005. The GALEX data have a spatial resolution of 4.2″ and 5.3″ in the FUV and NUV, respectively. The pixel scale of the GALEX images is 1.5″ / pix.

The optical data used for this research come from the Legacy ExtraGalactic UV Survey (LEGUS, Calzetti et al. 2015)[2]. LEGUS is an HST Cycle 21 Treasury programme that has imaged 50 nearby star-forming dwarf and spiral galaxies within 18 Mpc in the NUV $(F275W)$, U $(F336W)$, B $(F438W)$, V $(F555W)$, and I $(F814W)$ bands using the UVIS channel of the Wide Field Camera Three (WFC3) and the Advanced Camera for Surveys (ACS) in parallel. LEGUS images have a spatial sampling of 0.04″/pix.

We also made use of ground-based optical images from the Sloan Digital Sky Survey DR12 (SDSS, Alam et al. 2015)[3] in its five u, g, r, i, and z bands. SDSS images have a spatial sampling of 0.39″/pix.

In addition, NIR data in the J (1.25 μm), H (1.65 μm), and K_s (2.16 μm) filters from the Two Micron All Sky Survey (2MASS, Jarrett et al. 2000)[4] were used. 2MASS images have a pixel scale of 1.0″.

Furthermore, we made use of the $Spitzer$ Infrared Array Camera (IRAC, Fazio et al. 2004)[5] images of NGC 3344 taken in the 1, 2, 3, and 4 bands (3.6, 4.5, 5.8, and 8 μm, respectively). IRAC images have a pixel scale of 0.75″.

Finally, we obtained archival 24, 70, and 160 μm data from the Multiband Imaging Photometer (MIPS, Rieke et al. 2004)[6] for $Spitzer$. MIPS images have a spatial sampling of

[1] http://www.galex.caltech.edu
[2] https://archive.stsci.edu/prepds/legus/
[3] https://dr12.sdss.org/home
[4] https://www.ipac.caltech.edu/2mass
[5] http://irsa.ipac.caltech.edu/data/SPITZER/docs/irac
[6] http://irsa.ipac.caltech.edu/data/SPITZER/docs/mips

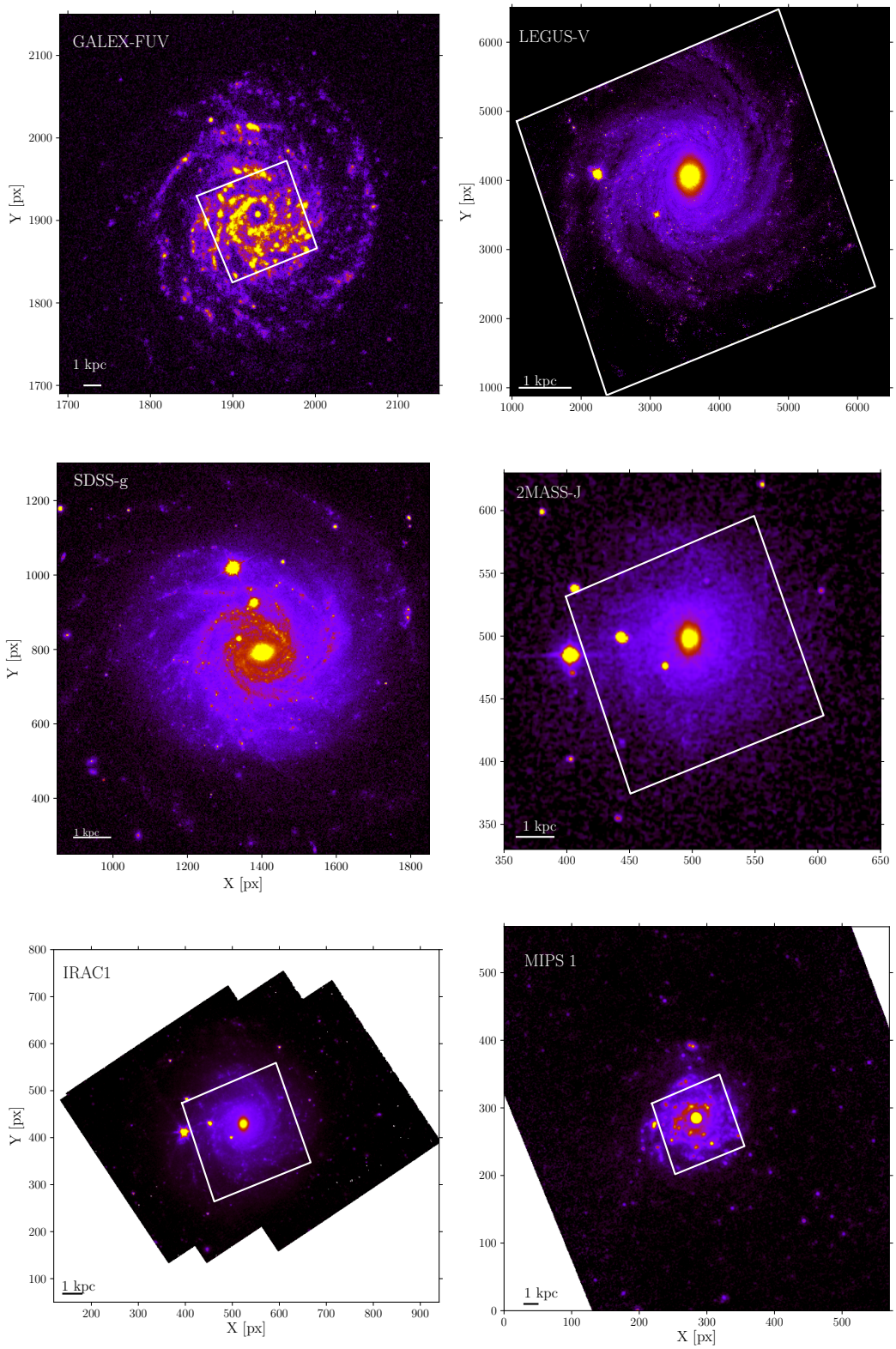

Figure 3.2.1: Some of the images collected for NGC 3344 and used in this work. From top left: GALEX-FUV, LEGUS-V, SDSS-g, 2MASS-J, IRAC-3.6 μm, and MIPS-24 μm. The white box shows the LEGUS WFC3 / UVIS footprint.

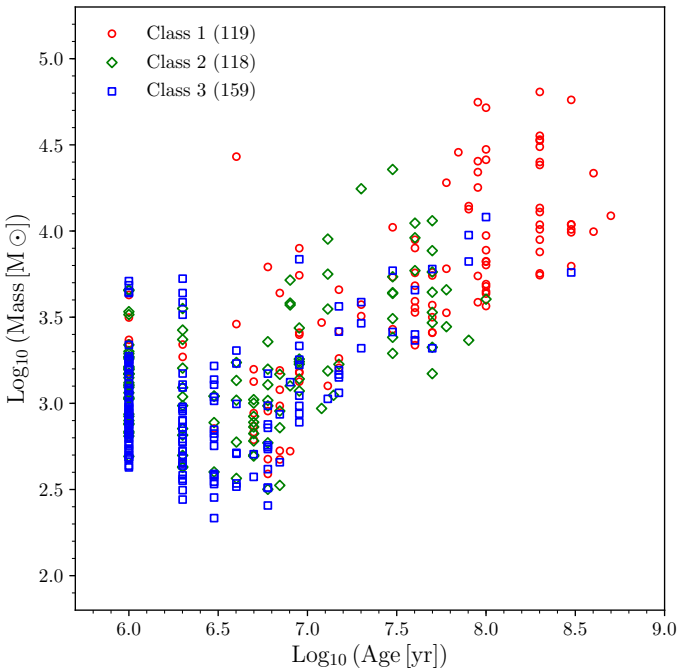

Figure 3.2.2: The distribution of ages and masses for the 396 star clusters in NGC 3344. The colours and shapes represent different cluster classifications: red circles for Class 1, green diamonds for Class 2, and blue squares for Class 3 (see § 3.2.2 for an explanation). The number of clusters in each class is shown in parentheses.

1.5, 6, and 9 ″/pix at 24, 70, and 160 μm, respectively.

In Fig. 3.2.1, we show six examples of the imaging data used in this study.

3.2.2 The star cluster catalog

In this Section, we take advantage of the stellar cluster catalog of NGC 3344 provided by the LEGUS team for our analysis. We refer the interested reader to Chapter. 1 for detailed explanations.

In this study, we made use of star clusters of Class 1, 2, and 3, whose properties were derived using Yggdrasil deterministic models based on the Padova stellar libraries (see Zackrisson et al. 2011, for details) with the Kroupa (2001) stellar initial mass function (IMF), solar metallicity, and the Milky Way extinction curve (Cardelli et al. 1989).

Fig. 3.2.2 shows the distribution of ages and masses of the star clusters in NGC 3344. The derived cluster physical properties based on the Yggdrasil deterministic models are quite uncertain at cluster masses below 5000 $M_{\odot}$ (Krumholz et al. 2015). In this study, we do not apply any mass cut due to the small number statistics available for massive clusters. The number of low-mass ($<$ 5000 $M_{\odot}$) and high-mass ($>$ 5000 $M_{\odot}$) star clusters in each of the

Table 3.3.1: Number of low-mass (< 5000 $M_\odot$) and high-mass (> 5000 $M_\odot$) star clusters in Class 1, 2, and 3.

	Class 1	Class 2	Class3
low-mass clusters	66	106	150
high-mass clusters	53	12	9

morphology classes is listed in Tab. 3.3.1.

3.3 Star Clusters Associated with the Spiral Arms and Inner Ring

In this Section, we examine the spatial distribution of the star clusters in three different age bins across the galaxy NGC 3344.

3.3.1 Spiral arms

In order to compare star clusters of different ages in different areas of NGC 3344, we first need to define the loci of its spiral arms and inner ring. We define the spiral arms according to their optical brightness in the LEGUS B-band image. We used a Gaussian kernel with a 5 pixel sigma to blur the image and enhance the spiral arms. Subsequently, we identified two pronounced spiral arms. We also located the inner ring of the galaxy at 1 kpc from the center (Verdes-Montenegro et al. 2000). We focus only on the two prominent spiral arms and do not consider other stellar structures associated with the arms (e.g., spurs, etc.).

For the rest of this paper, we will refer to the southern and western arms as Arm 1 and Arm 2, respectively. The upper panel of Fig. 3.3.1 presents the two main arms and the inner ring overplotted on the smoothed LEGUS B-band image.

3.3.2 Spatial distribution of the star clusters

In the bottom panel of Fig. 3.3.1, we plot the spatial distribution of the stellar clusters with different ages. Following our previous work (Shabani et al. 2018), we divided the star clusters into three different groups: star clusters younger than 10 Myr ("Young" clusters), clusters with ages between 10 and 50 Myr ("Intermediate-age" clusters), and clusters older than 50 Myr ("Old" clusters).

In general, we observe that the star clusters with different ages are mainly concentrated in the inner ring, inter-arm regions, and along Arm 1. More precisely, we see that the young star clusters mostly populate Arm 1 rather than Arm 2. This is particularly evident in the brightest portion of Arm 1 (the upper region that is closer to the inner ring) where the young clusters tend to clump together. They can also be found in the inner ring of the galaxy. Arm 1 and the inner ring can be clearly traced by the young star clusters while Arm 2 is fainter and sparsely populated by young clusters. The intermediate-age and old star clusters are more spatially spread and can be found both at the location of the spiral arms and the inter-arm

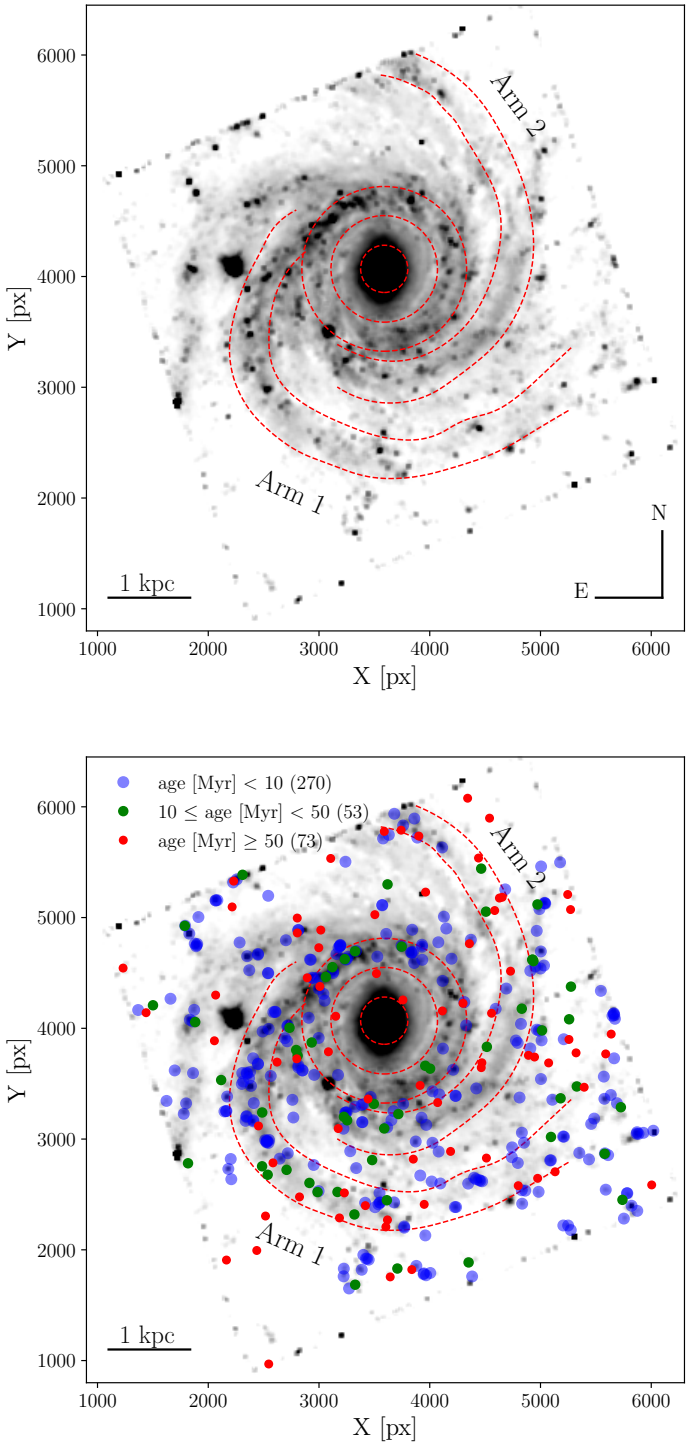

Figure 3.3.1: Top panel: the location of the defined spiral arms (red dashed lines) overplotted on the smoothed B-band image. The red dashed circles are centered on the nucleus of the galaxy and the inner ring. Bottom panel: the spatial distribution of star clusters with different ages on the LEGUS B-band image. The blue, green, and red circles show the young star clusters (age [Myr] < 10), the intermediate-age star clusters (10 < age [Myr] < 50), and old ones (age [Myr] > 50), respectively. The number of clusters in each sample is listed in parentheses.

Table 3.3.2: The number density of the young, intermediate-age, and old star clusters in different regions of the galaxy with different applied mass-cuts.

Applied mass-cut	Regions	Young	Intermediate-age	Old
No mass cut	Arm 1	19.66	3.33	5.67
	Arm 2	10.48	3.22	4.48
	Ring	14.28	2.20	7.14
	Inter-arm	6.46	1.24	1.99
4000 $M_\odot$	Arm 1	0.66	2.0	3.33
	Arm 2	0.0	0.81	4.03
	Ring	0.0	0.0	0.0
	Inter-arm	0.56	0.44	1.55
3000 $M_\odot$	Arm 1	2.0	2.0	3.67
	Arm 2	0.0	1.61	4.43
	Ring	0.0	0.0	0.0
	Inter-arm	0.72	0.72	1.71
2000 $M_\odot$	Arm 1	3.33	3.0	3.67
	Arm2	0.40	2.41	4.43
	Ring	1.65	1.65	0.0
	Inter-arm	1.57	0.99	1.99

regions. We note that our results might be biased due to the uncertainty in the derived physical properties for low mass clusters. We have tested our results using different mass cuts (4000, 3000, and 2000 $M_\odot$) and we observe that in all cases the number density of the young star clusters (number of star clusters with different ages in each region divided by the area of that region) in Arm 1 is the highest among the other defined regions (refer to Tab. 3.3.2).

Furthermore, we note that some of the young star clusters are located in the inter-arm regions of the galaxy. Our finding is in agreement with the ground-based Hα observations of NGC 3344 (Dale et al. 2009) where Hα emission was detected in both spiral arms and inter-arm regions. In Fig. 3.3.2, we overplot the star clusters younger than 10 Myr (blue circles) on the Hα image. The Hα image is star and continuum subtracted and it is also corrected for [NII] contamination assuming [NII]/Hα = 0.52 (Kennicutt et al. 2008). As we can see, the location of the young star clusters in the inter-arm regions coincides with the location of the observed Hα emission. This illustrates that some recent star formation might have taken place in the inter-arm areas. Furthermore, there are a few young star clusters that are not associated with any Hα emission peaks. This finding might be due to the uncertainty on the derived ages of the star clusters, meaning that their real ages could be older and thus they are not expected to be associated with Hα emission. These young star clusters have low masses ($< 5000\ M_\odot$) and thus the absence of Hα emission could also be due to a stochastic sampling of the upper part of the stellar mass function. The lack of young star clusters along Arm 2 is also consistent with the small number of Hα peaks in this arm in comparison with Arm 1.

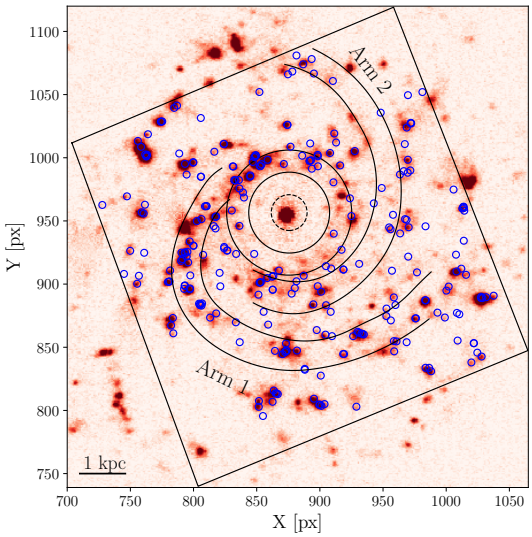

Figure 3.3.2: The spatial distribution of the star clusters younger than 10 Myr (blue circles) overplotted on the Hα image obtained from Dale et al. (2009). The black box shows the LEGUS WFC3 / UVIS footprint.

Here, attention is drawn to the observed lopsidedness in the distribution of the young star clusters and Hα emission in the two main spiral arms of the galaxy. Below, we investigate whether this lopsidedness correlates with any asymmetry in the SFR and stellar mass surface density distribution in the two arms.

3.4 Methodology

In order to study the origin of the observed asymmetry in the distribution of star clusters among the spiral arms of NGC 3344, we produce spatially resolved SFR and stellar mass surface density maps. To do so, we use a pixel-by-pixel photometric SED fitting technique (Bothun 1986; Abraham et al. 1999; Welikala et al. 2008; Zibetti et al. 2009; Wuyts et al. 2012; Sorba and Sawicki 2015; Abdurro'uf and Akiyama 2017; Abdurro'uf 2018; Williams et al. 2018). The fundamental steps of this method are (1) image preparation including PSF matching, image registration, and flux calibration, (2) pixel binning, and (3) fitting photometric SEDs to the data to extract the physical parameters. In this Section, we describe these steps in detail for a dataset of GALEX (FUV, NUV), LEGUS (NUV, UV, B, V, and I), 2MASS (J, H, and K_s), and $Spitzer$ (3.6, 4.5, 5.8, 8, and 24 μm) images. Later, we will repeat these steps by replacing the HST images with SDSS ones.

3.4.1 PSF matching and image regridding

Imaging data for this study were taken from a variety of surveys, therefore a careful and precise data reduction is required to make the data homogeneous. To apply the pixel-by-pixel photometric SED fitting, all images should have the same point spread function (PSF) and pixel scale.

To measure the PSF of each of the background subtracted images, we visually selected non-saturated and isolated stars in the optical images and made use of the **psfmeasure** command in IRAF [7]. For the non-optical images, we adopted the PSF values from the corresponding instrument handbook. The broadest PSF belongs to the MIPS-24μm image, which has a PSF full-width-at-half-maximum (FWHM) of 6″. Then, all other images were convolved with the Gaussian kernels to match their PSFs to that of the MIPS-24μm image. The convolution kernels were calculated using the **PSFmatch** algorithm in IRAF.

After convolving the images to reach the same resolution, we registered and resampled all the images (from FUV to 24 μm) to a pixel scale of 1.5″ per pixel (MIPS-24μm, GALEX-FUV, and GALEX-NUV). Afterwards, the images were aligned to the LEGUS ones, which cover the inner region of the galaxy. For the remainder of this paper, we consider only the pixels inside the LEGUS-UVIS footprint. The FWHM and pixel scale of each image are listed in Tab. 3.4.1.

3.4.2 Flux calibration

In order to measure the flux associated with each pixel in each band, we first removed stars and any clear artifacts in the background-subtracted images. Then, we converted all of the pixel values into units of Jansky (Jy) as follows:

The pixel values of GALEX images are in units of counts per second (CPS). To convert them to Jy, we used the following equations[8]:

$$\mathrm{Flux_{fuv}}[\mathrm{erg\ sec^{-1}cm^{-2}\ \AA^{-1}}] = 1.04 \times 10^{-15}\mathrm{CPS} \tag{3.1}$$

$$\mathrm{Flux_{nuv}}[\mathrm{erg\ sec^{-1}cm^{-2}\AA^{-1}}] = 2.06 \times 10^{-16}\mathrm{CPS} \tag{3.2}$$

$$\mathrm{Flux[Jy]} = 3.34 \times 10^{4}\lambda^{2}\ \mathrm{Flux\ [erg\ sec^{-1}cm^{-2}\AA^{-1}]} \tag{3.3}$$

where CPS is the pixel value in counts per second and λ is the wavelength in Å.

[7] IRAF (Image Reduction and Analysis Facility) is distributed by the National Optical Astronomy Observatory, operated by the Association of Universities for Research in Astronomy, Inc., under cooperative agreement with the National Science Foundation.

[8] https://asd.gsfc.nasa.gov/archive/galex/FAQ/counts-background.html

Table 3.4.1: The wavelength, FWHM, and pixel scale of the images used in this study.

Images	Wavelength (μm)	FWHM (arcsec)	Pixel scale (arcsec per pixel)
GALEX FUV	0.1516	4.5	1.5
GALEX NUV	0.2267	5.4	1.5
LEGUS NUV	0.2704	0.087	0.0396
LEGUS UV	0.3355	0.081	0.0396
LEGUS B	0.4325	0.075	0.0396
LEGUS V	0.5308	0.072	0.0396
LEGUS I	0.8024	0.089	0.0396
SDSS u	0.3551	1.3	0.39
SDSS g	0.4686	1.2	0.39
SDSS r	0.6165	1.07	0.39
SDSS i	0.7481	0.95	0.39
SDSS z	0.8931	1.01	0.39
2MASS J	1.25	2.89	1.00
2MASS H	1.65	3.04	1.00
2MASS K_s	2.15	3.06	1.00
IRAC 1	3.6	1.6	0.75
IRAC 2	4.5	1.6	0.75
IRAC 3	5.8	1.6	0.75
IRAC 4	8.0	1.9	0.75
MIPS 1	24	6	1.5
MIPS 2	70	18	4.5
MIPS 3	160	40	9

To convert LEGUS images, which are expressed in units of electrons per second to Jy, we multiplied the pixel values by the inverse sensitivity factor (PHOTFUN) in units of Jy $\times$ sec/e. The PHOTFUN value of each filter is given as a keyword in the image header.

The SDSS images are presented in units of nanomaggy where 1 nanomaggy $\approx 3.631 \times 10^{-6}$ Jy.

The pixel values of 2MASS images are in units of data-number [DN]. To convert these to Jy, we followed the recipe available on the 2MASS website [9]. Briefly, we first converted the pixel values into magnitudes:

$$\mathrm{mag} = \mathrm{MAGZP} - 2.5 \log[\mathrm{DN}] \tag{3.4}$$

where MAGZP is the zero point magnitude in each filter, which can be found in the image header. Then, 2MASS magnitudes were converted into Jy applying:

$$\mathrm{Flux\ [Jy]} = 10^{-0.4\mathrm{mag}}\ \mathrm{F_0[Jy]} \tag{3.5}$$

[9] https://www.ipac.caltech.edu/2mass/releases/allsky/faq.html

where $\mathrm{F}_0[\mathrm{Jy}]$ is the flux for the zero-magnitude zero point (see Table 1 of Section VI.4a of the All-Sky Data Release Explanatory Suppement).

Spitzer images (IRAC and MIPS) are given in units of surface brightness in MJy/sr where sr is the solid angle. Surface brightness values can be converted into flux density [Jy] per pixel using the following conversion:

$$[\frac{\mathrm{MJy}}{\mathrm{sr}}]\,[\frac{10^6\mathrm{Jy}}{\mathrm{MJy}}]\,[\frac{\pi\mathrm{rad}}{180\,\mathrm{deg}}]^2\,[\frac{1\,\mathrm{deg}}{3600''}]^2\,[\frac{\text{pixel scale (arcsec)}}{\text{pixel}}]^2 \tag{3.6}$$

where 1 $[\mathrm{arcsec}]^2$ = 2.3504 $\times 10^{-11}$ sr.

Afterwards, all fluxes were corrected for Galactic foreground extinction with A_V = 0.088 mag as derived by Schlafly and Finkbeiner (2011) according to the extinction curve of Cardelli et al. (1989) for wavelengths between 0.1μm and 3.3μm, and the mid-infrared extinction law of Chapman et al. (2009) for the wavelengths from 3.6μm to 24μm.

In Fig. 3.4.1, we show the results of our image processing for six of the images from Fig. 3.2.1.

3.4.3 Pixel binning: Voronoi tessellation

In order to construct spatially resolved maps of SFR and stellar mass surface density, we need to enhance the signal-to-noise ratio (S/N) of the pixel-by-pixel photometric SED. For this purpose, we bin the pixels to reach a threshold S/N value of 10 per bin (following Wuyts et al. 2012; Abdurro'uf and Akiyama 2017). Firstly, we calculated the S/N of each pixel using the following equation:

$$S/N = \frac{S}{\sqrt{S + \sigma_r^2 + \sigma_b^2}} \tag{3.7}$$

where σ_r and σ_b are the read-out noise and rms of the median background level. Subsequently, we implemented the Voronoi two-dimensional binning technique (Cappellari and Copin 2003) in order to spatially group the pixels[10].

As an example, the left-hand panel of Fig. 3.4.2 shows the Voronoi 2D binned map of NGC 3344 in the LEGUS UV band with 458 bins. The colour coding indicates the index number of each bin. The blank pixels are those without signal in the UV band. In the right-hand panel of Fig. 3.4.2, we show the distribution of the adopted bins in area (in units of pc^2).

We note that there are several bins located in the spiral arms or the inner ring that partially overlap with the interarm regions. We visually selected overlapping bins and excluded those that have more than 50 % of their area outside the spiral arm or the inner ring. Afterwards, we took the median of the flux and the corresponding error on the median flux in

[10] In this work, we used the VorBin code from Michele Cappellari's Python and IDL Programs: http://www-astro.physics.ox.ac.uk/ mxc/software/

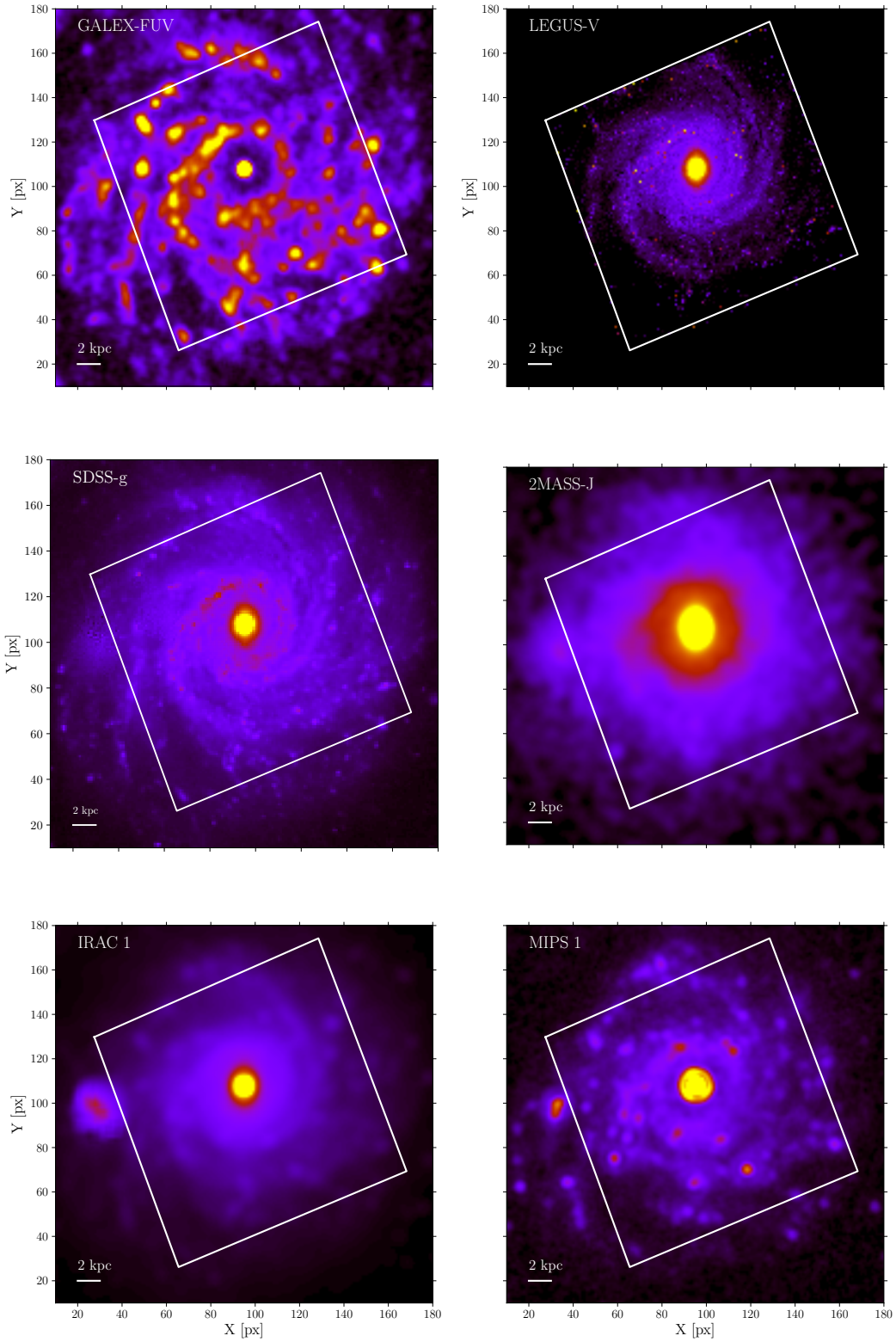

Figure 3.4.1: Same as Fig. 3.2.1, but after image processing.

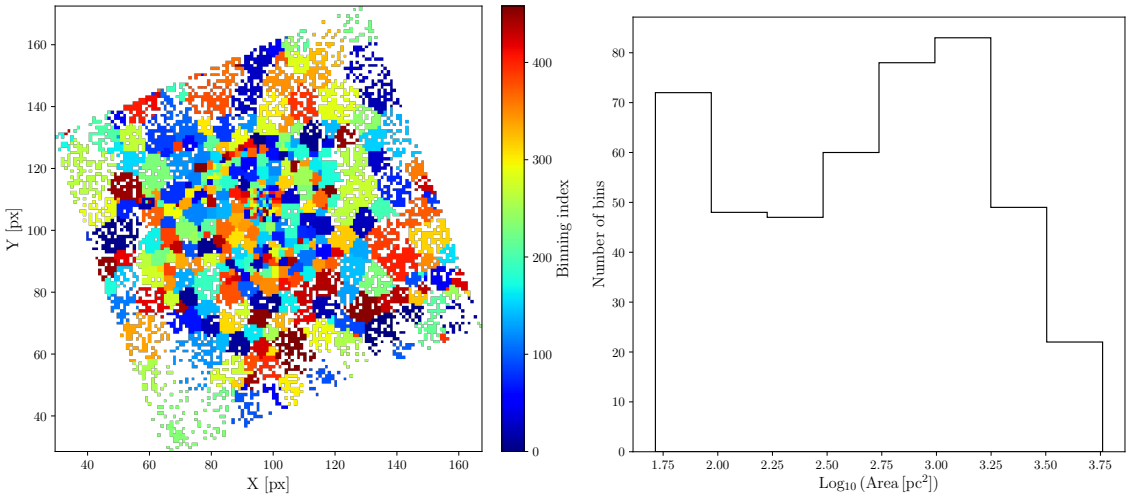

Figure 3.4.2: The Voronoi binning map of NGC 3344 in the LEGUS UV band. The colour bar shows the index number of each bin (left panel). The distribution of the adopted bins in area in units of pc^2 (right panel).

each bin for the 15 bands from FUV to 24 μm to run the SED fitting code MAGPHYS. We do not consider the calibration uncertainty in each band in the derived error on the median flux, since it is lower than the error on the bin's median flux.

3.4.4 From UV to IR: SED Fitting

We derived the SFR and stellar mass per pixel in each individual bin by using MAGPHYS[11] (Multi-wavelength Analysis of Galaxy Physical Properties, da Cunha et al. 2008) to model the observed multiwavelength SED of NGC 3344. MAGPHYS is a simple, publicly available SED fitting code that has been widely used throughout the literature (e.g. da Cunha et al. 2008, 2010; Smith et al. 2012; Berta et al. 2013; Lianou et al. 2014; Viaene et al. 2014; Davies et al. 2015; Hayward and Smith 2015; Smith and Hayward 2015; Viaene et al. 2016; Smith and Hayward 2018; Williams et al. 2018; Hunt et al. 2019).

The MAGPHYS code uses the Bruzual and Charlot (2003) stellar population synthesis package to model the emission of stars assuming a Chabrier (2003) IMF with a range of metallicities between 0.0 < Z ($Z_\odot$) < 2.0.

The process of star formation is modeled with an exponentially declining SFR law, characterized as SFR(t) $\propto$ $\exp(-\mathrm{t}\gamma)$, where t is the age of the galaxy and γ^{-1} stands for star formation time-scale. The SFR is assumed to be averaged over the last 100 Myr.

The code uses the two-component dust model of Charlot and Fall (2000), which accounts for the additional attenuation of starlight from young stars (< 10 Myr) due to the dust in their short-lived birth clouds in comparison to the older stars. In addition, MAGPHYS enforces

[11] http://www.iap.fr/magphys

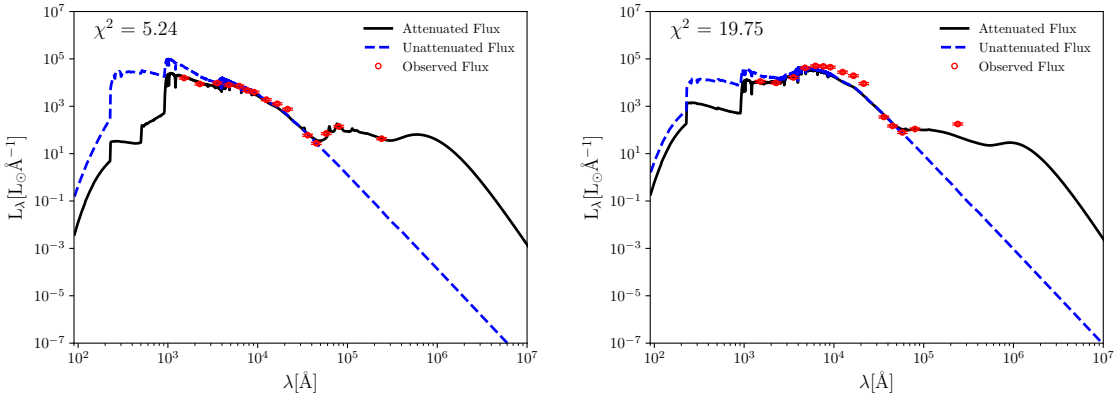

Figure 3.4.3: An example of a good (left-hand panel) and poorly constrained (right-hand panel) SED fit of NGC 3344 obtained with MAGPHYS. The dashed blue and black solid lines represent the unattenuated SED and the best fit to the data (the dust attenuated SEDs), respectively. The observed fluxes are shown in red circles.

an energy balance where the energy from UV to optical wavelengths absorbed by dust is re-radiated in the far-infrared. The energy balance feature is needed to model the whole galaxy SED (Smith and Hayward 2015), but it may not be suitable for sub-kpc regions since the emission from neighboring areas can affect the flux of a given pixel.

MAGPHYS was designed initially for galaxy-scale SED fits, thus its parameter space is not proper for the low flux values of a single pixel or bin in a galaxy. Following Viaene et al. (2014) and Williams et al. (2018), we artificially increased the median flux of each bin by a factor of 10^4 to achieve higher fluxes of the order of integrated light from galaxies. The obtained SFR and stellar mass parameters are linearly correlated with the flux and thus it is necessary to scale them back to derive their real fitted values (Viaene et al. 2014).

Furthermore, it is necessary to carefully examine the quality of the fits to filter out unreliable ones and their estimated physical parameters. For this purpose, we use the method employed by Viaene et al. (2014) to remove the poorly constrained SED fits. This pixel filtering method uses the 16th, 50th, and 84th percentiles (p_{16}, p_{50}, and p_{84}) for each parameter from the MAGPHYS output to calculate the mean relative error as follows:

$$\sigma_r = 0.5 \times (p_{84} - p_{16})/p_{50} \tag{3.8}$$

Subsequently, all the estimated parameters with $\sigma_\mathrm{r} > 0.32$ are discarded. Applying this criterion, we have excluded 6.3% of the total bins. In Fig. 3.4.3, we show an example of a good fit (upper panel) and a poorly constrained fit (lower panel) of our MAGPHYS final results.

3.5 Galaxy SFR and stellar mass maps

In this Section, we will show the results of our MAGPHYS SED fitting on sub-kpc scales. For our estimate of galaxy physical properties, we take the values of the best-fit model. We only focus on SFR and stellar mass in our pixel-by-pixel analysis to see how these vary in different regions of the galaxy. In addition, we investigate whether the derived physical properties based on the HST optical filters are consistent with the results obtained with the SDSS images while keeping the other filters the same as before. Further, we will repeat our analysis by adding the 70 μm and 160μm MIPS filters to our data.

3.5.1 HST filters

The SFR and stellar mass surface density maps derived by running MAGPHYS on the GALEX, HST, 2MASS, IRAC, and MIPS-24 μm photometry are shown in Fig. 3.5.1. In these maps, the blank pixels from Fig. 3.4.2 (pixels with S/N <= 0) are replaced with the average value of the SFR and stellar mass of the neighboring pixels.

The upper panel of Fig. 3.5.1 shows the SFR surface density map, which ranges from 1.5 $\times 10^{-5}$ to 3.6 $\times 10^{-3}$ $\mathrm{M_{\odot} yr^{-1} kpc^{-2}}$. The lower values of the SFR (darker bins) were mostly associated with Arm 2 and the inter-arm regions, notably in the western part of the galaxy. The higher SFR values (brighter bins) are found along Arm 1, in the upper part of the ring, and the beginning of Arm 2, all located in the eastern part of the galaxy. In addition, we observe that the SFR surface density map clearly traces the prominent Arm 1 and shows some star-forming regions associated with the inner ring and inter-arm regions of the galaxy. In contrast, Arm 2, which is visible in the optical images is, mostly washed out.

The bottom panel of Fig. 3.5.1 shows the stellar mass surface density map ranging from 3.15×10^4 to 3.15×10^6 $\mathrm{M_{\odot} kpc^{-2}}$. We observe a clear homogeneous distribution of stellar mass along the two spiral arms. Further, we observe that all spiral patterns have faded away and the galaxy does not show any prominent spiral in its stellar mass surface density map.

It is important to note that, because of its high angular resolution, HST is less sensitive to faint diffuse emission, and thus we may miss a significant fraction of it. This might affect the derived stellar mass and SFR surface density map of the galaxy.

3.5.2 SDSS filters

In order to test whether the derived physical properties in § 3.5.1 depend on the choice of the optical photometry, we replaced HST optical images with the SDSS u, g, r, i, and z images and we kept the rest of the images unchanged. We repeated all the steps described in § 3.4 for the new set of data but in order to be able to make a bin-by-bin comparison between the results, we used the same Voronoi binning as before.

In Fig. 3.5.2, we present the observed and the MAGPHYS best fit SEDs obtained with the HST and SDSS images for two individual bins located in Arm 1 and Arm 2. We see that

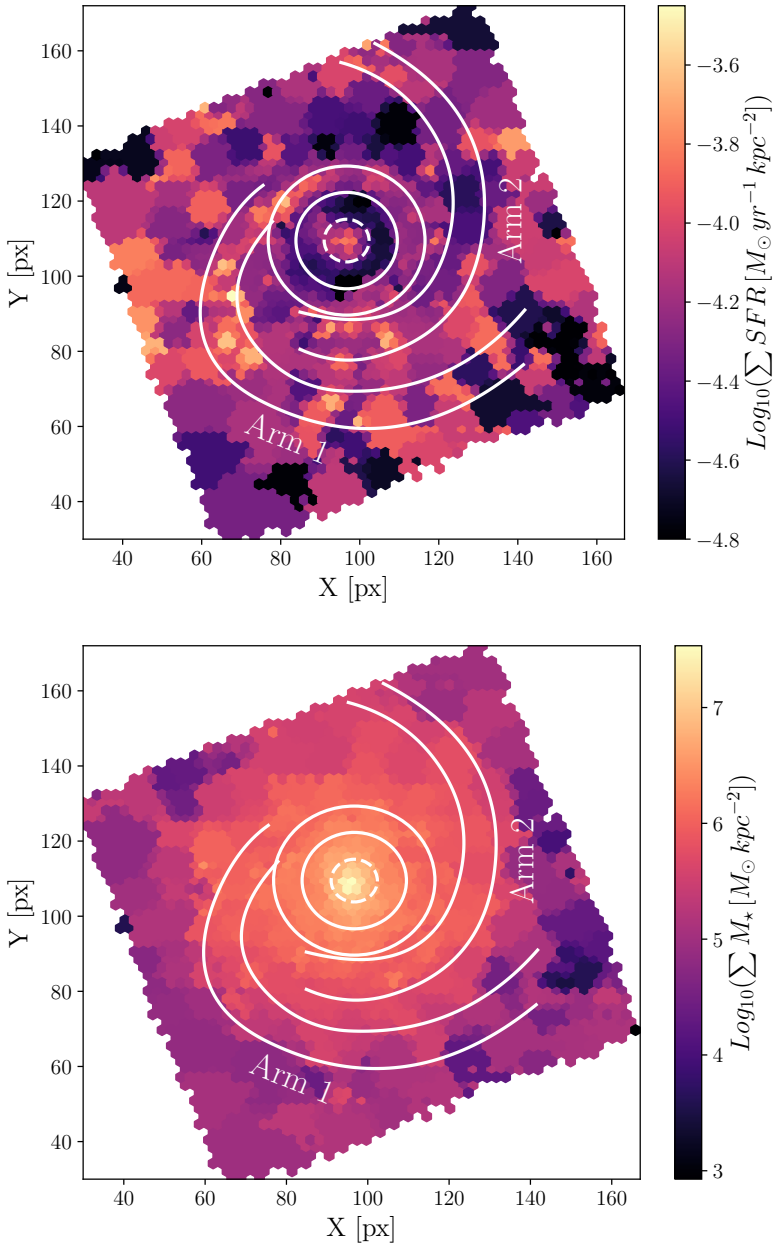

Figure 3.5.1: The SFR and stellar mass surface density maps (upper and bottom panels, respectively), resulting from pixel-by-pixel SED fitting using HST images. Different SFR and stellar mass surface densities are encoded with different colours. The spiral arms as defined in § 3.3.1 are overplotted on the SFR and stellar mass surface density maps. The white dashed circle is centered on the nucleus of the galaxy. The two white solid circles enclose the inner ring. North is up and east is to the left.

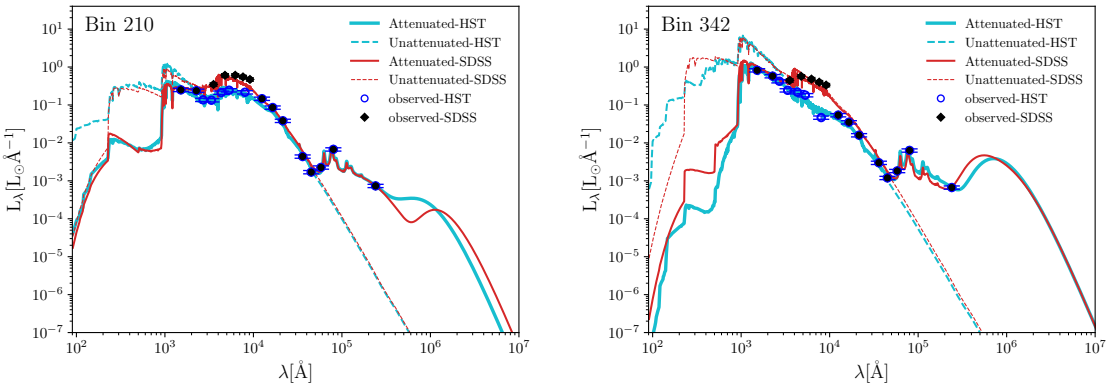

Figure 3.5.2: Example MAGPHYS SEDs obtained with HST (cyan) and SDSS data (red) for two individual bins of Arm 1 (bin 342) and Arm 2 (bin 210). The dashed and solid lines represent the unattenuated SED and the best fit to the data (the dust attenuated SEDs), respectively. The observed SEDs of HST and SDSS are shown in blue circles and black diamonds, respectively. Note that the fluxes were scaled back by the same factor to place them into MAGPHYS parameter space.

using SDSS images gives higher luminosity density than HST images with a mean value of 0.33 ± 0.095 L_λ $Å^{-1}$. The observed difference is due to the recovered diffuse emission in the SDSS photometry which is lost in the HST photometry. Therefore, the remainder of this study will be based on the SFR and stellar mass surface density maps derived based on the SDSS optical images.

The resulting SFR and corresponding uncertainty surface density maps from MAGPHYS derived using SDSS images instead of HST images are shown in Fig. 3.5.3. The upper panel of Fig. 3.5.3 shows the SFR surface density map ranging from 10^{-5} to 1.6×10^{-4} $M_\odot yr^{-1} kpc^{-2}$ The presence of Arm 1 (particularly the upper part), the lower part of Arm 2 (which is closer to the ring), and the inner ring of the galaxy are quite visible in the SFR surface density map. Additionally, we observe some star-forming inter-arm regions located in the southern part of the galaxy. A bin-by-bin comparison between SFR surface density maps shows that both maps trace similar star-forming regions but the SFR map derived using HST images returns higher SFR values than the one based on SDSS images with a median offset of $(4.69 \pm 0.92) \times 10^{-5}$, $(3.81 \pm 0.71) \times 10^{-5}$, and $(2.38 \pm 0.55) \times 10^{-5}$ $M_\odot yr^{-1} kpc^{-2}$ in Arm 1, Arm 2, and the inner ring, respectively.

Fig. 3.5.4 presents the stellar mass surface density map and its corresponding error map derived based on SDSS images, which ranges from 6.3 $\times 10^4$ to 3.16 $\times 10^7$ $M_\odot kpc^{-2}$. We observe that the spiral structure is washed out in the stellar mass surface density maps derived with either HST or SDSS images. This is not an artifact of the applied Voronoi binning, because we use the same bins to build the SFR and stellar mass surface density maps, and the presence of spiral arms is evident in the SFR map. In addition, we find that the map derived using SDSS images gives higher stellar mass values than the one from HST images with the median values of $(2.26 \pm 0.28) \times 10^5$, $(2.89 \pm 0.49) \times 10^5$, and $(3 \pm 0.54) \times 10^5$ $M_\odot kpc^{-2}$ in

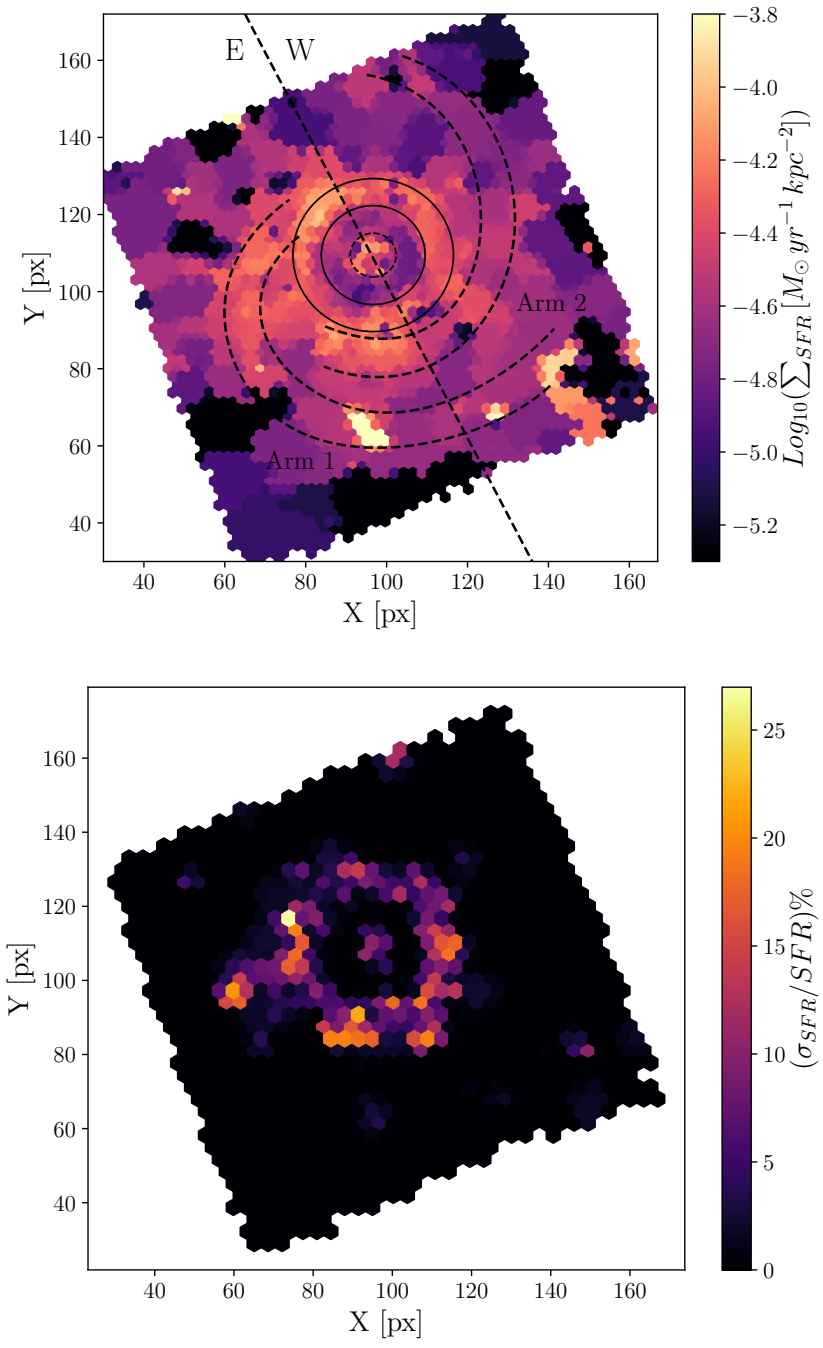

Figure 3.5.3: The SFR surface density map (upper panel) and the unncertainty of SFR surface density map (lower panel) using SDSS optical images instead of HST images. The black dashed line divides the galaxy into an eastern (E) and a western (W) part.

Arm 1, Arm 2, and the inner ring, respectively. Our findings are in agreement with previous studies by Zibetti et al. (2009), Abdurro'uf and Akiyama (2017), and Abdurro'uf (2018), who found that spiral arms as traced by star-forming regions can be detected in the SFR surface density maps, while their strength appears to be much more reduced in the stellar mass surface density maps.

Fig. 3.5.5 better quantifies the distribution of the SFR and stellar mass in Arm 1, Arm 2, and the inner ring of the galaxy. In the left-hand panel of Fig. 3.5.5, we observe that Arm 1 and Arm 2 are peaking at low SFR values $\approx 0.32 \times 10^{-4}$ while the inner ring peaks at higher SFR values of $\approx 0.45 \times 10^{-4}$ and 0.7×10^{-4} $\mathrm{M_{\odot} yr^{-1} kpc^{-2}}$. The results of our two-sample K-S test show that the two spiral arms have a fairly similar SFR distribution while the inner ring differs (the derived p-values are much lower than the test's significance level (0.05) of the null hypothesis). Nevertheless, despite the analogous distribution of the SFR between Arm 1 and Arm 2, we see a different picture as we move toward regions with SFRs higher than 1×10^{-4}. These regions are not present in Arm 2, while they encompass 13% of the SFR bins associated with Arm 1. In addition, only 2% of the SFR bins of the inner ring exhibit such high values.

The right-hand panel of Fig. 3.5.5 shows an evident offset between the stellar mass distributions of the inner ring and the two spiral arms confirming that the galaxy is more massive in the center compared with the outer regions. In addition, Arm 1 and Arm 2 are approximately similar in terms of their stellar mass distribution.

3.5.3 Additional IR filters

In order to derive the SFR, MAGPHYS requires IR filters. Our observed SEDs extend up to 24μm and lack the peak of dust infrared emission ($\approx$ 100 μm, derived using the dust effective temperature of 30 K as measured in star-forming galaxies by Bendo et al. 2003), thus leaving the energy balance feature potentially unconstrained. Therefore, MAGPHYS might include more (less) dust than physical values in the SEDs, producing more (less) light from obscured star formation. This might lead to overestimating (underestimating) SFR values.

In order to further test the impact of the IR filters on the physical properties derived with MAGPHYS, we added MIPS 70 and 160μm images to our dataset in §. 3.5.2. For this investigation, we convolved all the images with Gaussian kernels to match their PSFs to the one from the MIPS-160μm image. We also re-sampled all the images to a pixel scale of 9″ per pixel. Subsequently, we model the SEDs on a pixel-by-pixel basis considering 91 bins derived from Voronoi binning. By including these two filters we significantly decrease the spatial resolution of the images.

The resulting SFR and stellar mass surface density maps are shown in Fig. 3.5.6. The SFR surface density map (upper panel) shows that bins with a higher SFR value are mostly located in the inner ring and the upper portion of Arm 1. In addition, due to the low spatial resolution maps, we do not observe any spiral structure. In the stellar mass surface density map (bottom panel) we see that the center of the galaxy is more massive than its outer regions.

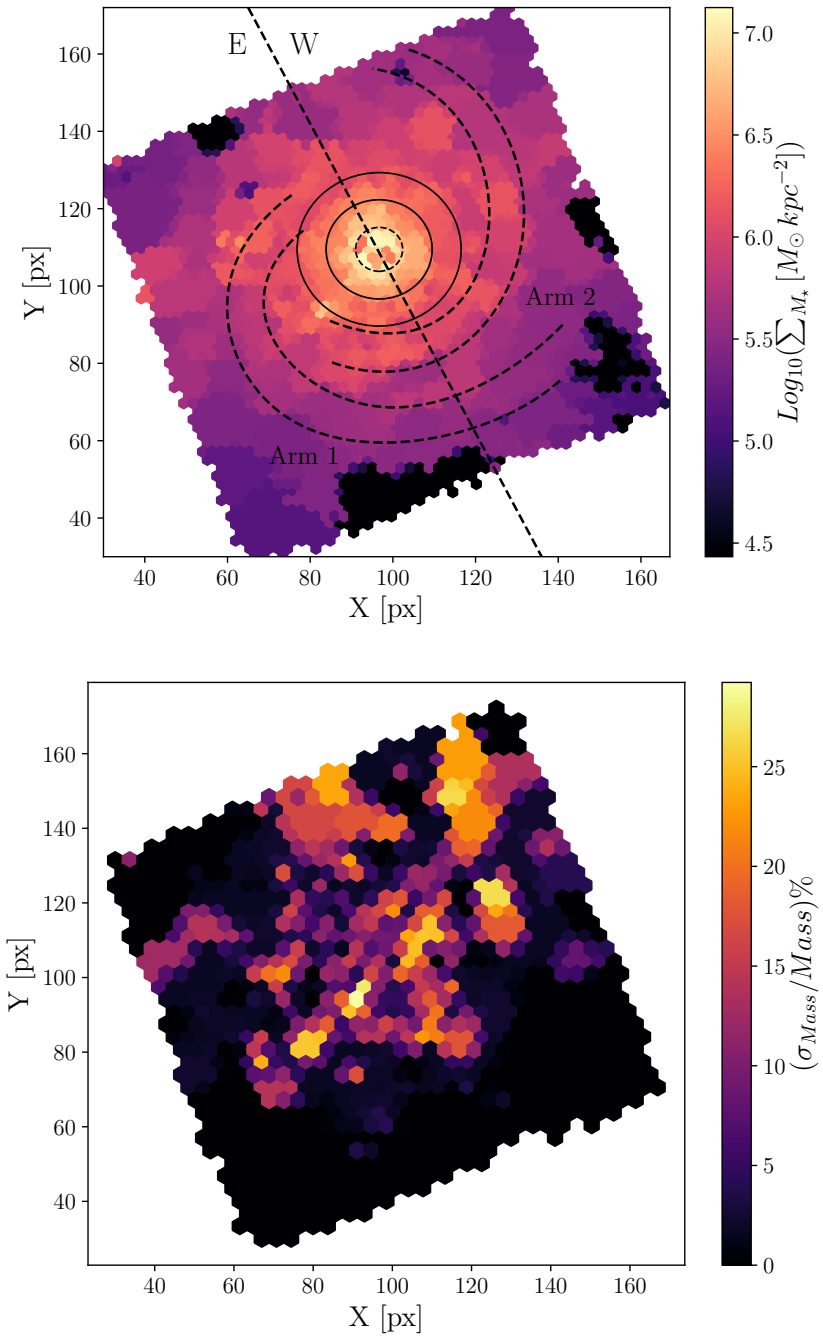

Figure 3.5.4: Same as Fig. 3.5.3 but for the stellar mass parameter.

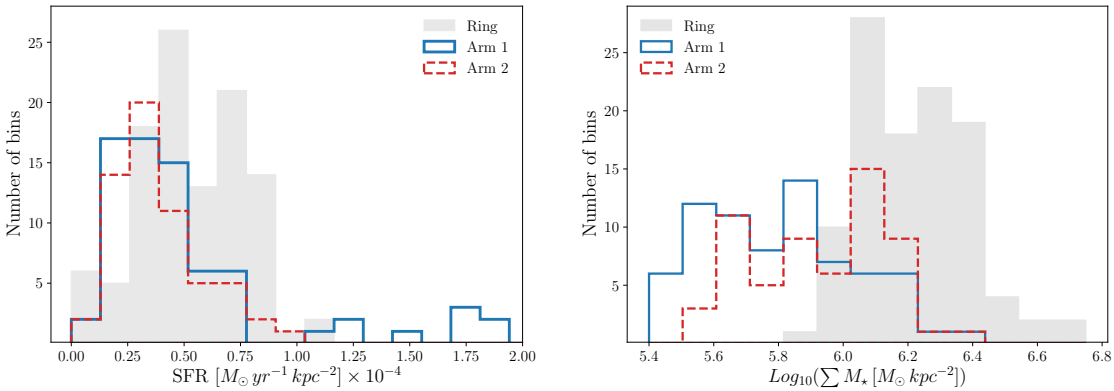

Figure 3.5.5: The distribution of SFR (left-hand panel) and stellar mass (right-hand panel) surface densities in three different regions. Arm 1, Arm 2, and the ring are shown in blue, red, and grey, respectively.

A comparison between the high resolution (Fig. 3.5.4 and Fig. 3.5.3) and low resolution maps (Fig. 3.5.6) derived by excluding and including MIPS 70 and 160μm images show a trend of increasing SFR with increasing pixel scale (decreasing spatial resolution). This increase in the SFR could also be due to the including obscured star formation from MIPS 70 and 160μm. We find an offset in the median of the derived SFRs of $\approx$ 1.5 dex. In contrast, the low and high-resolution stellar mass surface density maps have almost the same range of values and we do not find any evidence of a resolution dependence.

In addition, Smith and Hayward (2018) report a similar result in their study of the efficiency of MAGPHYS to recover the physical properties of a simulated spiral galaxy in sub-kpc regions. They compared the galaxy properties, including stellar mass and SFR derived from MAGPHYS and simulations at different spatial resolutions from 0.2 to 10 kpc. They found that MAGPHYS is capable of producing a good estimation of stellar mass both at high resolution (pixel scale $<$ 1 kpc) and low resolution (pixel scale $>$ 1 kpc). Their results suggest that the spatial resolution does not have any influence on the derived stellar mass. Their results for the SFR are more complicated, MAGPHYS recovers well the SFR particularly at pixel scales $>$ 1 kpc but moving toward smaller sub-galactic regions (where the energy balance criterion may not hold true) it becomes more resolution-dependent.

3.6 Radial variation of SFR and stellar mass

In this Section, we investigate the radial dependence of the spatially resolved SFR and stellar mass surface density and sSFR. Firstly, we considered the bins within seven concentric, circular annuli with a radius starting from 0.5 kpc and increasing up to 3 kpc. We did not consider the central nuclear region of the galaxy. Then, the radial profiles of SFR, stellar mass, and sSFR were constructed by calculating their average values in each annulus and normalizing by the first annulus values. Furthermore, we divided the galaxy into an east-

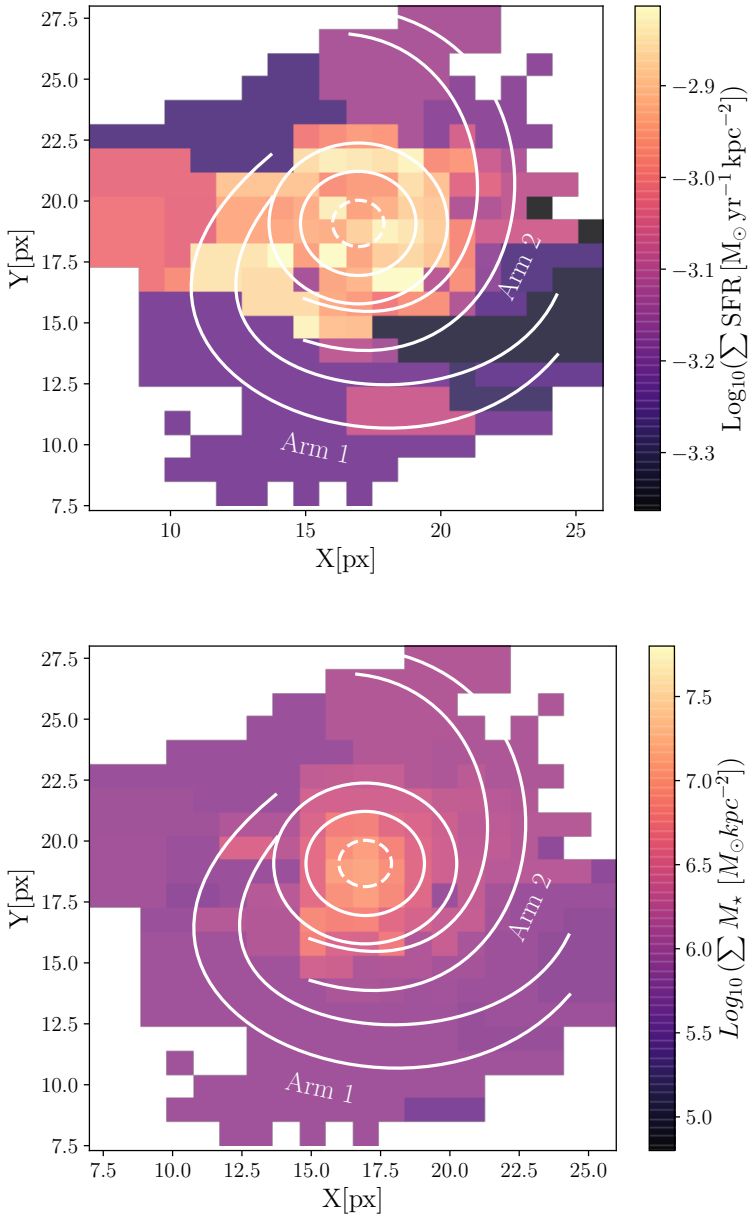

Figure 3.5.6: The SFR (upper panel) and stellar mass (lower panel) surface density maps derived based on using IR filters up to 160μm.

ern (dominated by Arm 1) and western (dominated by Arm 2) part, and repeated the same procedure but now only using half-circle annuli. Fig. 3.6.1 presents the radial profiles of the aforementioned parameters for the whole galaxy and its eastern and western regions where the error bars were calculated from the standard deviation of the average values.

The top panel of Fig. 3.6.1 shows that the radial profile of the stellar mass surface density is declining toward the outskirts. In addition, we do not observe any significant difference between the stellar mass distribution in the eastern and western parts of the galaxy.

The middle panel of Fig. 3.6.1 shows that the distribution of the SFR surface density is not symmetric throughout the galaxy. We observe that the eastern part of the galaxy has a higher SFR surface density in comparison to the western part. We also observe that the radial profile of the SFR surface density in both regions is decreasing from the center to a radius of ≈ 2 kpc. Beyond this radius the SFR profiles diverge somewhat. In the next annuli, we see an increase in the SFR in the eastern part, mainly due to the highly star-forming regions in Arm 1, while the SFR surface density remains constant on the western side. In the last radius annulus, we observe an increase of the SFR surface density in the western region as a result of the high SFR in the inter-arm regions.

In the bottom panel of Fig. 3.6.1 we see that the radial distribution of the sSFR is increasing with radius from the inner to the outer regions. This result is consistent with the inside-out scenario of galaxy formation, which suggests that star formation activity and stellar mass distribution were more centrally concentrated in the past and gradually extended outwards at later times. In addition, the distribution of the SFR is more extended (and shallower) than that of the stellar mass confirming that the current star formation is more active in the outer regions than past star formation (Cole et al. 2000; van den Bosch 2002; Dutton and van den Bosch 2009; Gomes et al. 2016; García-Benito et al. 2017).

3.7 SFR Tracers

The star formation rate (SFR) can be measured using different indicators that are sensitive to different stellar populations and time scales. In this Section, we consider the SFR surface density maps determined via the FUV+24μm and Hα+24μm tracers and compare them with the ones derived with MAGPHYS.

3.7.1 FUV + 24μm tracer

We first combine GALEX-FUV and $Spitzer$-24μm images to calculate the SFR surface density applying the Voronoi binning derived in § 3.4.3. The FUV continuum comes from hot, massive O and B stars, and therefore is a very good tracer of unobscured star formation over a time-scale of 10-100 Myr (Kennicutt 1998; Calzetti et al. 2005; Salim et al. 2007). The 24μm emission measures the continuum emission from small dust grains heated by the ionizing photons of young and massive stars, and thus correlates with the ongoing star formation over a time-scale of 10 Myr (Calzetti et al. 2005; Pérez-González et al. 2006; Calzetti et al.

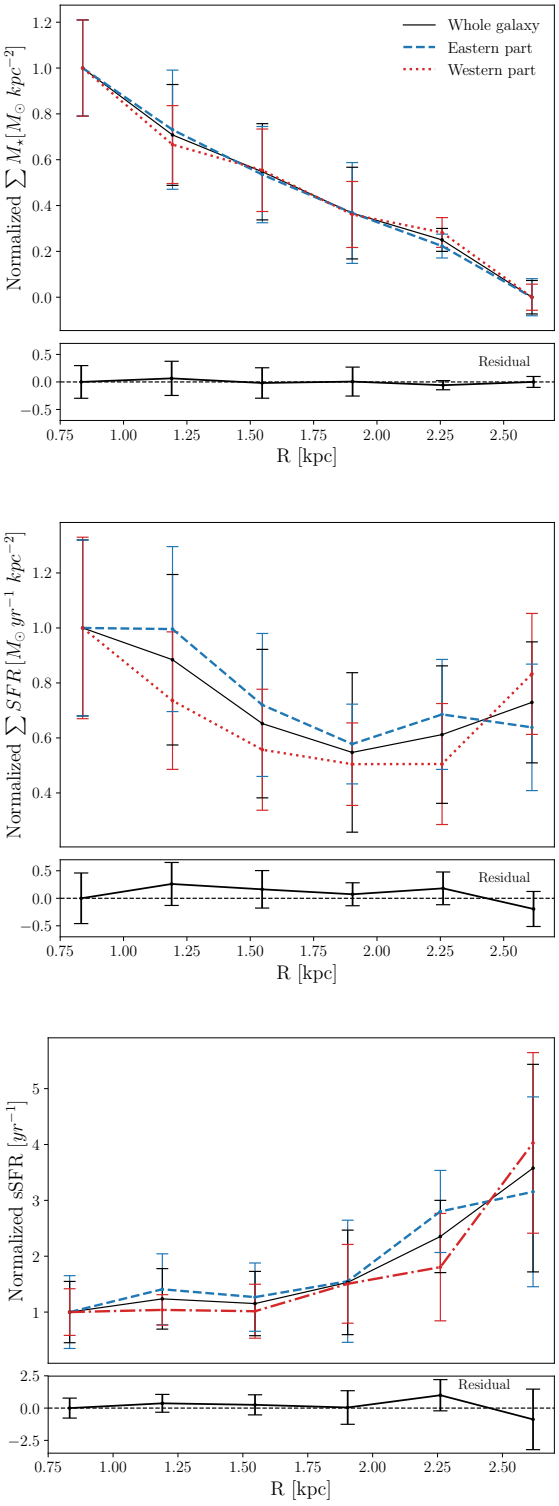

Figure 3.6.1: The normalized radial profile of the average stellar mass (top panel) and SFR (middle panel) surface density and sSFR (bottom panel) for the whole galaxy (black solid line), eastern part (blue dashed line), and western part (red dotted line). The error bars were calculated from the standard errors of the average values. The bottom panels of each diagram show the difference in the stellar mass, SFR, and sSFR between the eastern and western parts.

2007). Thus, a combination of these tracers measures the recent unobscured and obscured star formation (Leroy et al. 2008).

In this paper, we adopt the FUV and 24μm SFR calibration of Leroy et al. (2008) assuming a Kroupa (2001) IMF:

$$\Sigma_{SFR} = 8.1 \times 10^{-2}\, I_{FUV} + 3.2^{+1.2}_{-0.7} \times 10^{-3}\, I_{24} \tag{3.9}$$

where $\Sigma_{\rm SFR}$ has the unit of $\mathrm{M_\odot\,kpc^{-2}\,yr^{-1}}$, and $\mathrm{I_{FUV}}$ and $\mathrm{I_{24}}$ are intensities in MJy $\mathrm{sr^{-1}}$. We correct the FUV and 24μm emission for the possible contribution of older populations by subtracting a fraction of the observed intensity of 3.6μm using the following equations:

$$I_{FUV,corr} = I_{FUV,obs} - \alpha_{FUV}\, I_{3.6} \tag{3.10}$$

$$I_{24,corr} = I_{24,obs} - \alpha_{24}\, I_{3.6} \tag{3.11}$$

where $\alpha_{FUV} \sim 2 - 4 \times 10^{-3}$ (Dale et al. 2007; Johnson et al. 2007) and $\alpha_{24} = 0.1$ (Temi et al. 2005; Dale et al. 2007; Johnson et al. 2007).

3.7.2 Hα+24μm tracer

Finally, we use the ground-based Hα image from Dale et al. (2009) together with MIPS-24μm data to construct the SFR surface density map. In principle, the Hα emission originates from gas ionized by the youngest and hottest stars. Therefore, it is directly connected to current and unobscured star formation events. Since the 24μm emission provides a measure of the dust-obscured star formation, a combination of the two traces all the current star formation (exposed and embedded) in a region (Kennicutt et al. 2007; Calzetti et al. 2007).

Here, we use the Hα and 24μm SFR calibration of Calzetti et al. (2007), who assume a Kroupa (2001) IMF in the stellar mass range of 0.1-100 $\mathrm{M_\odot}$:

$$SFR = 5.3 \times 10^{-42}\, [L(H\alpha)_{obs} + 0.031\, L(24\mu m)] \tag{3.12}$$

where the SFR is in $\mathrm{M_\odot\,yr^{-1}}$ and both luminosities (L) are expressed in units of $\mathrm{erg\,s^{-1}}$. The advantage of using this calibration is that it is convenient for sub-kpc star-forming regions of the galaxy because measuring luminosities over smaller areas does not change the calibration (Calzetti et al. 2007).

3.7.3 SFR Comparison

In Fig. 3.7.1 we show the resulting SFR surface density maps from a combination of Hα+24μm (top panel), a combination of FUV+24μm (middle panel), and from MAGPHYS (bottom panel). We observe that the three SFR surface density maps trace the same star-forming

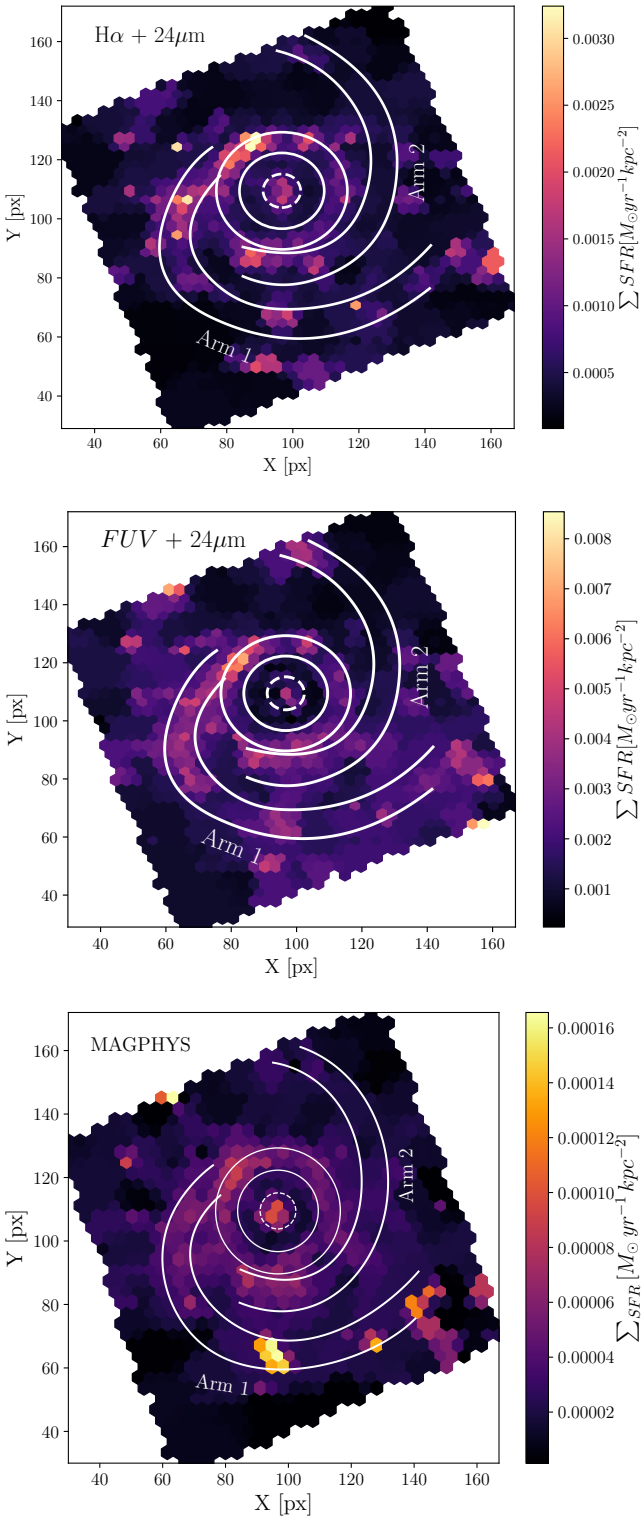

Figure 3.7.1: SFR surface density maps derived from a combination of Hα+24μm (top panel), a combination of FUV+24μm (middle panel), and from MAGPHYS (bottom panel).

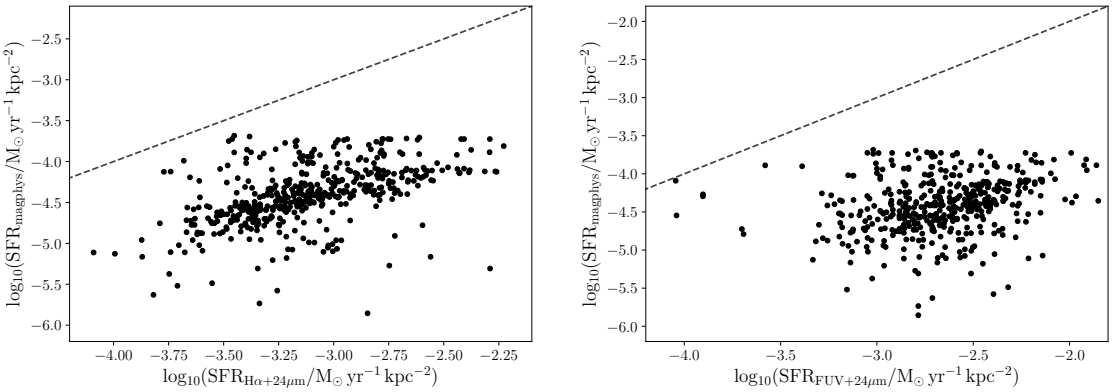

Figure 3.7.2: A bin-by-bin comparison between SFRs derived with MAGPHYS and the ones based on the Hα+24μm (left-hand panel) and FUV+24μm tracers (right-hand hand). The black dotted line shows the 1:1 relation.

regions of the galaxy. The inner ring and the spiral structure of Arm 1 are quite visible while Arm 2 has been washed out.

Fig. 3.7.2 presents a bin-by-bin comparison between the SFR surface density derived with the aforementioned tracers and the one from MAGPHYS. We find that the FUV+24μm tracer tends to give significantly higher SFR surface density values than MAGPHYS, with a median offset of 1.86 $\pm$ 0.0075 dex. It must be noted that MAGPHYS enforces an energy balance, a feature needed to model the whole galaxy (Smith and Hayward 2015) which may not be suitable for sub-kpc regions, since the emission from neighboring areas can affect the flux of a given pixel. Here, we resolve sub-kpc regions of the galaxy where this energy balance may not hold true and star formation is likely to vary over a time-scale of few Myr (Relaño and Kennicutt 2009; Boselli et al. 2009).

In addition, we find that the SFR derived based on the Hα+24μm tracer returns higher SFR surface density values than MAGPHYS with a median offset of 1.23 $\pm$ 0.011 dex. The observed differences are likely due to the parametrization of the star formation history in the MAGPHYS models, which average it in steps of 0.1 Gyr over the last 1 Gyr. Thus, these models likely underestimate the star formation rate of the current burst that gives rise to the observed Hα and 24μm emission. As noted above, the assumption of a constant SFR could break down on the sub-kpc scales.

We note that the SFR surface densities based on FUV+24μm and Hα+24μm are calculated assuming a Kroupa (2001) IMF, while MAGPHYS uses a Chabrier (2003) IMF to derive the SFR. Since the Chabrier (2003) IMF is similar to the one of Kroupa (2001), we do not need to scale the IMFs and the SFR surface density (Davé 2008; Driver et al. 2013). Thus, the discrepancy of the derived SFRs based on the different indicators is not due to the influence of the different IMFs used.

3.8 Discussion and conclusions

In this chapter, we present a new study of the lopsidedness in the distribution of the young star clusters along the two main spiral arms of NGC 3344. We observed that one spiral arm (the southern one, Arm 1) has a higher number density of the young star clusters (≈ 2 times more) than the other arm (the eastern one, Arm 2). In order to address the question of the possible correlation between the asymmetric distribution of the star clusters with the galaxy's physical properties (e.g., stellar mass and SFR), we built up an accurate spatially resolved SFR and stellar mass surface density maps of the galaxy. To do so, we assembled a multi-wavelength imaging data set from UV to IR to construct the observed SEDs of sub-kpc regions and modeled them with MAGPHYS on a pixel-by-pixel basis. Furthermore, we checked whether the derived physical properties depend on the choice of optical filters and observed that using SDSS optical filters gives a higher luminosity density than HST images due to the recovered diffuse emission in the SDSS photometry. Therefore, we used SDSS optical images to perform our analysis.

Our results show that the spiral arms of NGC 3344 is significantly reduced and smoothed out in the stellar mass surface density map. We did not find any significant lopsidedness in the distribution of the stellar mass among the two main spiral arms. This suggests that the two spiral arms might have a very similar integrated star formation history. Another possible explanation is that the differences in their past star formation history are not large enough to be reflected in their present-day stellar mass surface density map. In addition, we found that the derived spatially resolved SFR surface density map of NGC 3344 clearly traces Arm 1, the lower part of Arm 2, and the inner ring of the galaxy. Although our results do not show any clear evidence of the lopsidedness in the SFR distribution in the two arms, we note that Arm 1 hosts regions with higher SFR values.

In addition, we studied the radial profile of the averaged SFR and stellar mass surface density in NGC 3344. Our results indicate that the SFR and stellar mass surface density decline with increasing galacto-centric distance, while the sSFR increases with the radius being consistent with the inside-out scenario of galaxy formation.

We have also compared the derived SFR surface density map with MAGPHYS with those calculated with the FUV+24μm and Hα+24μm tracers. A bin-by-bin comparison among the derived SFR surface density maps shows that they are all tracing similar star-forming regions of the galaxy. However, MAGPHYS gives a lower value of the SFR surface density for a given bin than FUV+24μm and Hα+24μm. The observed discrepancy could be due to the assumption of a constant SFR over 100 Myr in MAGPHYS which may break down on sub-kpc scales and also to different time-scales for star formation (about 10 Myr for Hα and 100 Myr for MAGPHYS).

Further, we divided the galaxy into its eastern (dominated by Arm 1) and western (dominated by Arm 2) regions to study the radial dependence of the stellar mass and SFR surface density in the two sides of the galaxy. We did not observe any obvious asymmetry in the stellar mass distribution of the eastern and western regions of the galaxy, while our results show some degrees of lopsidedness in the distribution of SFR. The eastern part has a higher SFR

in comparison to the western part. Verdes-Montenegro et al. (2000) studied the formation of the inner and outer ring of NGC 3344 and found that the atomic gas is more extended to the east side of the galaxy than to the west. They suggest that this galaxy has experienced a recent accretion event, which may have changed the gas distribution in this galaxy. It might be possible that the asymmetric distribution of the gas is the main driver of the observed asymmetry in the distribution of recent and on-going star formation.

The main limiting factor to investigate whether the two arms are different in terms of their star formation is the lack of high-resolution HI and CO observations of the galaxy. Although the Berkeley Illinois Maryland Association Survey of Nearby Galaxies (BIMA SONG Helfer et al. 2003, with typical spatial resolution of 6″) and the Westerbork Synthesis Radio Telescope (WSRT, with spatial resolution of 20″), have provided CO and HI maps of NGC 3344, respectively, these data do not have enough resolution to be compared with the multi-wavelength images used in our study.

4

A Spatially-resolved, Multi-wavelength Study of Three LEGUS Disk Galaxies

In this chapter, we expand the previous study to three more spiral galaxies, NGC 1566, NGC 628, and M51a to explore the possible correlation between the distribution of star clusters along the primary two spiral arms of the host galaxy with its SFR and stellar mass surface density on sub-kpc scales.

4.1 Data

As we discussed in the previous chapter, we used images in two bands (FUV and NUV) from GALEX, and five bands (3.6μm, 4.5μm, 5.8μm, 8μm, and 24 μm) from Spitzer for NGC 1566, NGC 628, and M51a. As we showed in the previous chapter, the HST filters give a lower luminosity density in comparison with ground-based optical images (e.g., SDSS) due to the high angular resolution of HST and thus lower sensitivity to faint diffuse emission. For this reason, we made use of SDSS optical images (u, g, i, r, and z) when available (for NGC 628 and M51a). In the case of NGC 1566, we took optical filters (NUV, UV, B, V, and I) from HST/LEGUS since it is not in the SDSS sample.

4.2 Spatial Distribution of Star Clusters

In this Section, we investigate the spatial distribution of the star clusters with different ages along the two main spiral arms of NGC 1566, NGC 628, and M51a. We first defined the location of the spiral arms using the same method as we used in the previous chapter. Briefly, we

Table 4.2.1: The number density of the young, intermediate-age, and old star clusters in different regions of NGC 1566, NGC 628, and M51a.

Galaxy	Young		Intermediate-age		Old	
	Arm 1	Arm 2	Arm 1	Arm 2	Arm 1	Arm 2
NGC 1566	7.35	4.82	10.69	13.08	1.01	1.65
NGC 628	1.40	1.60	3.95	1.0	8.41	2.53
M51a (LEGUS)	3.53	2.30	4.71	2.32	10.70	7.07
M51a (Chandar et al. 2016)	3.49	1.93	0.70	0.71	2.76	4.59

used a Gaussian kernel with a 10 pixel sigma to blur the LEGUS B-band image and enhance the spiral arms, which we then traced according to their optical brightness. The location of the so-defined spiral arms of NGC 1566, NGC 628, and M51a is shown in Fig. 4.2.1, 4.2.2, and 4.2.3, respectively.

Subsequently, we divided star clusters into three different groups: star clusters younger than 10 Myr ("Young" clusters), clusters with ages between 10 and 50 Myr ("Intermediate-age" clusters), and clusters older than 50 Myr ("Old" clusters). In Fig. 4.2.1, 4.2.2, and 4.2.3 we plot the spatial distribution of the young (blue circles), intermediate-age (green circles), and old star clusters (red circles) in NGC 1566, NGC 628, and M51a, respectively.

In Fig. 4.2.1, we observe that the young star clusters mostly populate the two spiral arms of NGC 1566 rather than the inter-arm regions. This is particularly obvious in Arm 1 where the number density of the young clusters is larger than in Arm 2 (see Tab. 4.2.1). The intermediate-age star clusters are predominantly located along the two spiral arms and they tend to clump together. There are also more inter-arm clusters at intermediate-age than young clusters. The star clusters in the oldest bin appear more dispersed and less concentrated compared to the younger ones. In addition, the young and intermediate-age star clusters can clearly trace the two spiral arms of NGC 1566 while old clusters show very weak spiral arms.

Fig. 4.2.2 shows that young star clusters are mainly located along the two spiral arms of NGC 628. This is evident in the western side of Arm 2, where star clusters are highly clustered. There are too few clusters in the 1-10 Myr bin to determine if they can trace the spiral structures. The scarcity of the young clusters is due to the mass cut of $5000 M_{\odot}$ (for the reasons for the mass cut, see Section 2.3) which removes a significant number of low-mass young clusters. The intermediate-age star clusters are still concentrated in the spiral arms and clearly trace the spiral arms. Moving toward star clusters older than 50 Myr, we observe that they are both in the arms and inter-arm regions and widely spread compared to the young and intermediate-age star cluster samples.

Fig. 4.2.3 suggests that the youngest clusters are very concentrated in the two arms of M51a where they delineate very strong spiral arms. As clusters age, they have a higher chance to be scattered and thus they can be observed in the inter-arm regions of the galaxy in addition to the spiral arms.

In Fig. 4.2.4, we quantify and compare the distribution in age (left-hand panels) and

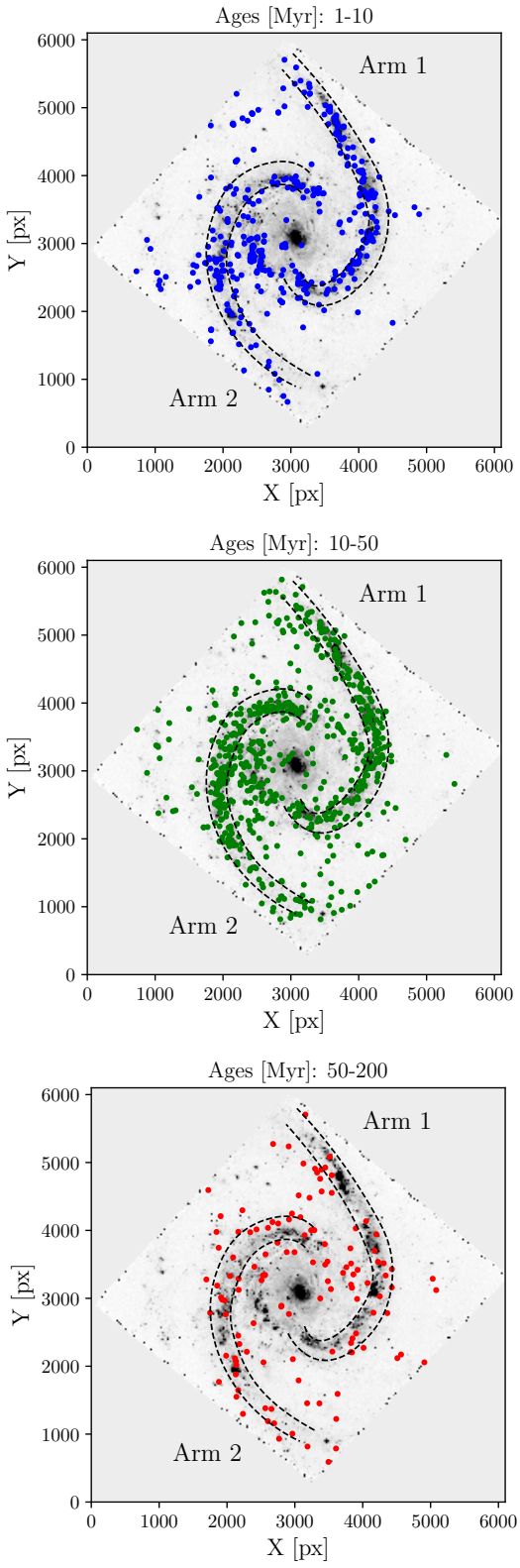

Figure 4.2.1: The spatial distribution of star clusters in NGC 1566 with different ages on the LEGUS B-band image. The blue, green, and red circles (from top to bottom) show the young (age [Myr] < 10), the intermediate-age (10 < age [Myr] < 50), and old star clusters (age [Myr] > 50), respectively. The location of the defined spiral arms is shown with black dashed lines.

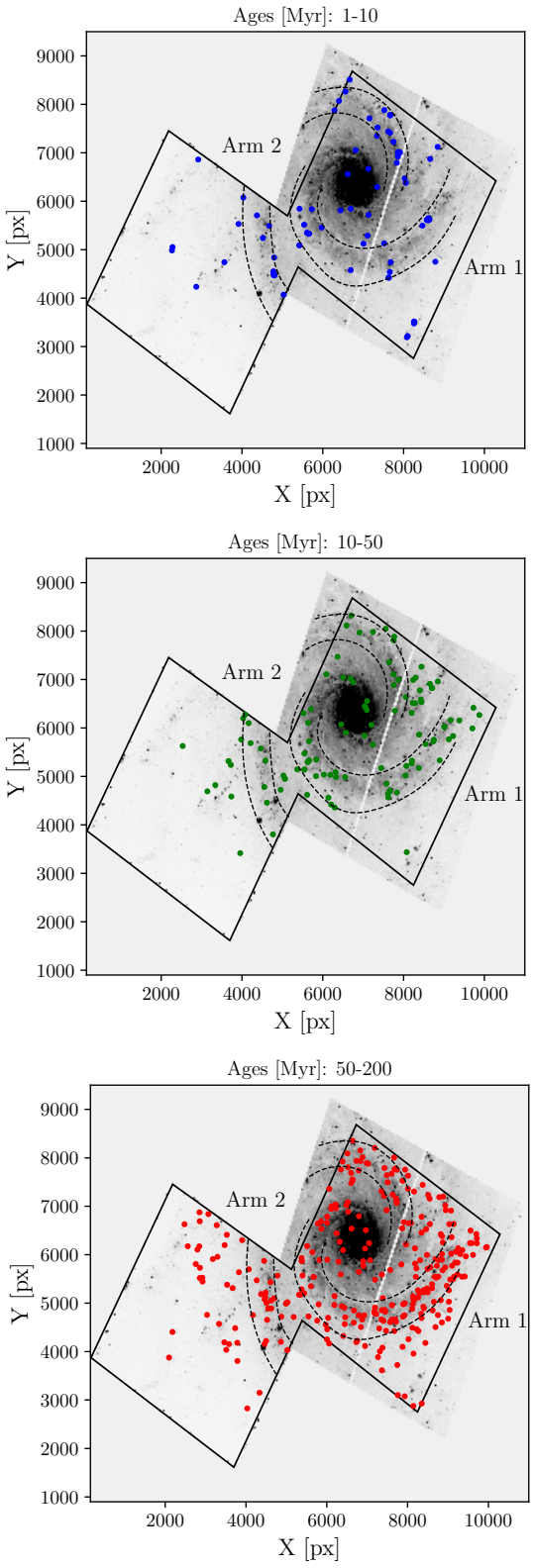

Figure 4.2.2: Same as Fig. 4.2.1 but for NGC 628.

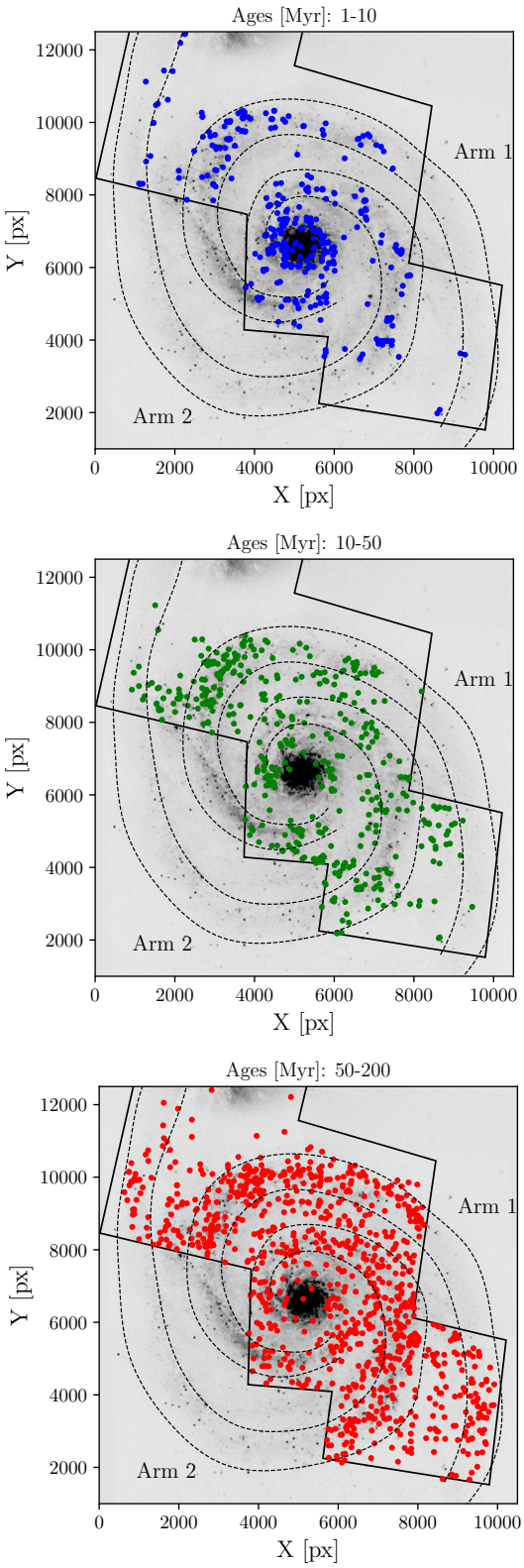

Figure 4.2.3: Same as Fig. 4.2.1 but for M51a.

Table 4.2.2: The median values of age and mass of star clusters associated with Arm 1 and Arm 2 in NGC 1566, NGC 628, and M51a.

Galaxy	Age [Myr]		Mass [$M_\odot$]	
	Arm 1	Arm 2	Arm 1	Arm 2
NGC 1566	13 ± 1.78	15 ± 2.24	$(1.5 \pm 0.31) \times 10^4$	$(1.6 \pm 0.24) \times 10^4$
NGC 628	70.0 ± 8.12	40 ± 9.52	$(1.0 \pm 0.38) \times 10^4$	$(8.74 \pm 4.16) \times 10^3$
M51a (LEGUS)	50.0 ± 3.92	60.0 ± 4.38	$(1.15 \pm 0.15) \times 10^4$	$(1.18 \pm 0.14) \times 10^4$

mass (right-hand panels) of star clusters associated with Arm 1 and Arm 2 in NGC 1566, NGC 628, and M51a (from top to bottom, respectively). In the case of NGC 1566 (top row), we observe that Arm 1 contains a larger number of young clusters than Arm 2, while moving toward older clusters, Arm 2 hosts more intermediate-age and old star clusters. The median age of star clusters located in the two spiral arms can be found in Tab. 4.2.2. Despite the similar distribution of star clusters in age in the two spiral arms of NGC 1566, the results of a two-sample K-S test with a p-value of 1.15×10^{-4} suggest that the age distributions of the clusters in Arm 1 and Arm 2 are unlikely to be drawn from the same population. The top right-hand histogram of Fig. 4.2.4 shows a fairly similar mass distribution of the star clusters located along Arm 1 and Arm 2. The K-S test with a p-value of 0.25 does not show any significant difference between the two distributions.

The middle left-hand histogram of Fig. 4.2.4 indicates that the two main spiral arms of NGC 628 accommodate approximately the same number of young star clusters. Further, we observe that Arm 1 contains a higher number of older star clusters in comparison with Arm 2 (also see Tab. 4.2.1). The normalized mass distribution of the star clusters located along the two arms shows that Arm 1 encompasses more massive star clusters than Arm 2. The results of a K-S tests suggest that the age distribution of the star clusters associated with Arm 1 and Arm 2 differ (with a p-value of 7.9×10^{-3}), while their mass distributions are likely drawn from the same distribution (derived p-value of 0.77).

What we can see in the bottom panels of Fig. 4.2.4 is that Arm 1 of M51a is characterized by higher number density of star clusters in the three defined samples than Arm 2. The age and mass distributions of the star clusters in the two arms of M51a appear relatively similar. The derived p-values of our K-S test (0.88 and 0.70 for the age and mass, respectively) confirm that there is no notable difference in the cluster age and mass between the two arms. We stress that the LEGUS/UVIS observations of M51a do not cover the whole galaxy and thus our findings on its spatial distribution of star clusters might be biased due to the missing clusters. To examine this, we used the star cluster catalog from Chandar et al. (2016) (see Section 2.7 for more detail) and found that Arm 1 of M51a has higher number density of young star clusters than Arm 2, while Arm 2 exhibits a higher number density of old star clusters. The derived p-values of 7.9×10^{-8} for the age indicate that the distributions in age of the star clusters in the two arms differ (Fig. 4.2.5). For the rest of this chapter, we will use the results obtained with the star cluster catalog of Chandar et al. (2016) due to its complete spatial coverage of M51a.

In this study, we try to understand whether the observed lopsidedness in the distribution of the young star clusters in NGC 1566 and M51a, or the asymmetry in the distribution of the older star clusters and the cluster mass in NGC 628 and also M51a originate from a lopsidedness in the SFR or from the stellar mass distribution of the galaxy.

4.3 Methodology

In order to examine the connection between the observed lopsidedness in the distribution of star clusters and the distribution of SFR and stellar mass of the host galaxy on sub-kpc scales, we applied a method called "pixel-by-pixel SED fitting", which is the same method we described in detail in the previous chapter of this thesis. Briefly, the method can be divided into three main steps: (1) PSF matching, image registration, and flux calibration, (2) pixel binning, and (3) fitting photometric SED to each of bins with a set of modeled SEDs to extract the physical properties.

First, the images from GALEX-FUV to IRAC-8μm of our three galaxies were convolved with a Gaussian kernel (using **psfmatch** task in IRAF) to match their PSFs to that of the MIPS-24μm image with a FWHM of 6″. Afterwards, all the images were registered to GALEX and MIPS-24μm sampling (1.5″ per pixel). Then, we aligned all the images to the LEGUS ones, which cover the inner area and the main spiral arms of the galaxies. The FWHM and pixel scale of the used images can be found in Tab. 3.4.1 of the previous chapter.

The flux and flux uncertainty in each filter associated with each pixel were calculated by converting from pixel values into units of Jansky (Jy) after removing background sources in the background-subtracted images. In Chapter. 3, we provided a detailed description of the conversion factors for the different surveys. Subsequently, we corrected the calculated fluxes for Galactic foreground extinction with A_V = 0.025, 0.192, and 0.095 mag for NGC 1566, NGC 628, and M51a, respectively, as derived by Schlafly and Finkbeiner (2011) based on the extinction curve of Cardelli et al. (1989) between 0.1μm and 3.3μm. For the wavelengths between 3.6μm and 24μm, we applied the mid-infrared extinction law of Chapman et al. (2009). In Fig. 4.3.1, 4.3.2, and 4.3.3, we show three examples of the imaging data of each galaxy used in this study before and after image processing.

The second step is the pixel binning to increase the S/N ratio. This was done by spatially grouping pixels to reach a threshold S/N value of 10 for NGC 1566 and NGC 628, and of 30 for NGC 628 due to its originally high S/N. To do so, we implemented the Voronoi two-dimensional binning method of Cappellari and Copin (2003). In the case of M51a, we masked the central region of the galaxy containing pixels with S/N > 10 in order to decrease the final number of bins and computational time. The above procedure left us with a minimum number of 478, 479, and 715 bins in the IRAC-5.8μm, LEGUS-B, and IRAC-4.5μm filters in NGC 1566, NGC 628, and M51a, respectively. We show the Voronoi 2D binned maps and the corresponding area of each bin (in units of pc^2) of our sample galaxies in Fig. 4.3.4.

Finally, we took the median of the flux and the corresponding error on the median flux in each bin of each galaxy for the 12 bands from FUV to 24μm to run the MAGPHYS SED

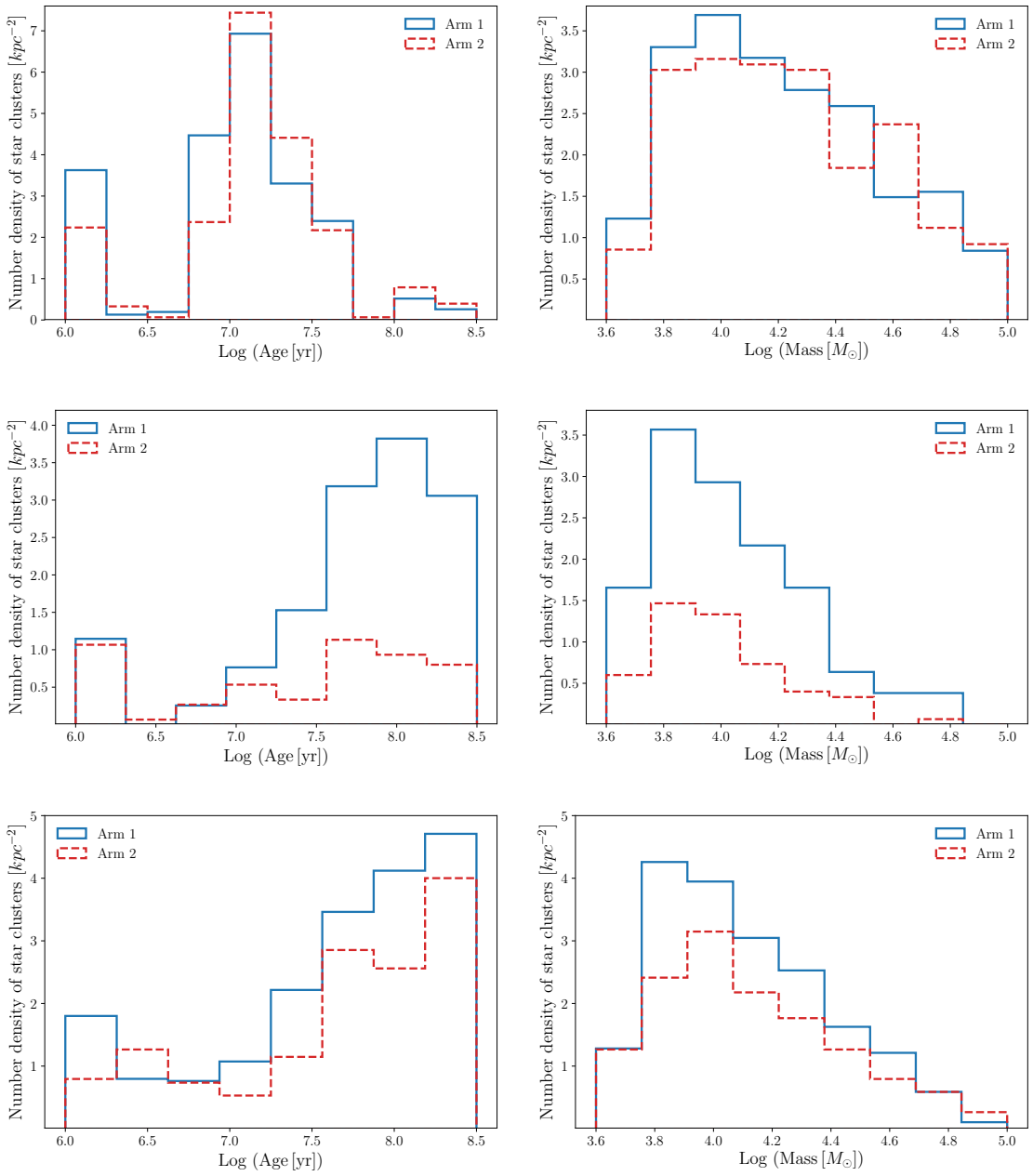

Figure 4.2.4: The age (left-hand panel) and mass (right-hand panel) distributions of star clusters associated with Arm 1 (blue line) and Arm 2 (red dashed-line) normalized by the area of the two arms in NGC 1566, NGC 628, and M51a, from top to bottom, respectively.

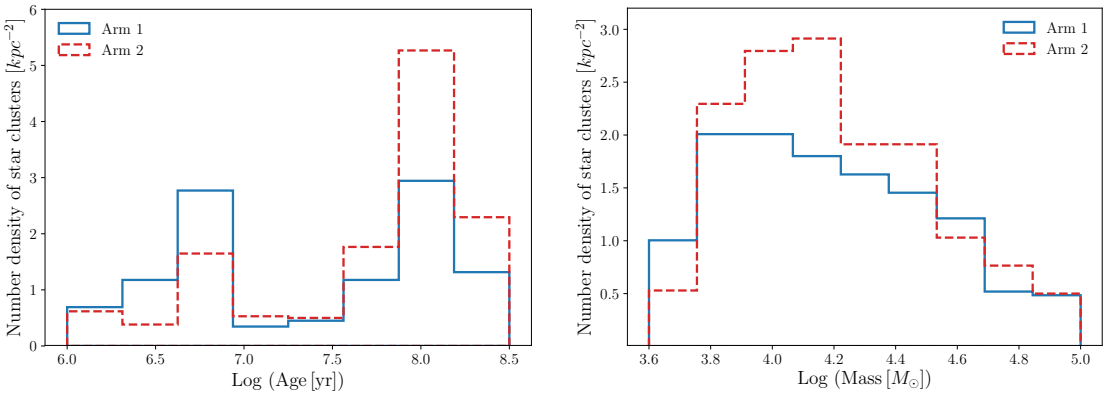

Figure 4.2.5: Same as Fig. 4.2.4 but for M51a using star clusters from Chandar et al. (2016) catalog.

fitting code to derive the SFR and stellar mass per pixel in each individual bin.

As we discussed in the previous chapter, before constructing the spatially resolved maps of the physical parameters we need to check the quality of the fits to omit bins with poorly constrained SEDs. Following Viaene et al. (2014), we removed bins with a mean relative error on SFR and stellar mass surface density larger than 30%. Implementing this criterion, we excluded 99, 43, and 22 bins from NGC 1566, NGC 628, and M51a, respectively. Subsequently, we set the SFR and stellar mass values of those bins to zero in the surface density maps. In Fig. 4.3.5, we present examples of the observed, either well or poorly fitted, SEDs for our target galaxies.

4.4 Galaxies SFR and Stellar Mass Maps

In this Section, we show the resulting SFR and stellar mass surface density maps of our sample galaxies derived from the MAGPHYS SED fitting. We will mainly compare the variation of these parameters in the two spiral arms located on the two different sides of each host galaxy.

4.4.1 NGC 1566

Fig. 4.4.1 shows the 2D spatially resolved SFR surface density map and its corresponding uncertainty map for NGC 1566. The error was calculated in each individual bin as follows:

$$\sigma_r = 0.5 \times (p_{84} - p_{16})/p_{50} \tag{4.1}$$

where p_{84}, p_{16}, and p_{50} are the 84th, 16th, and 50th percentile of the SFR (stellar mass) parameters derived from the MAGPHYS output.

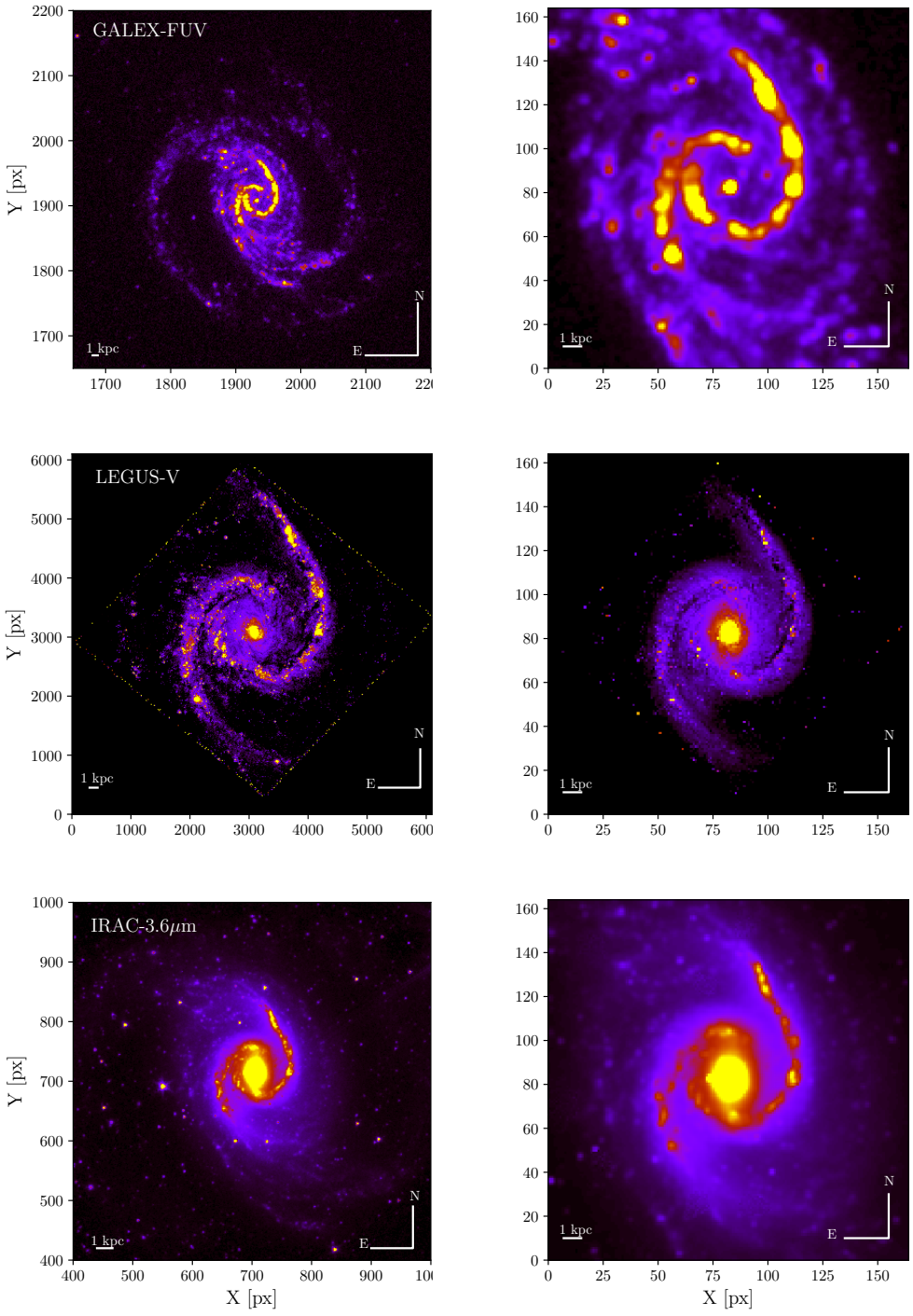

Figure 4.3.1: Three examples of the images collected for NGC 1566 and used in this work. The left-hand and right-hand panels show the images before and after image proccesing. The white horizontal bar in the lower left denotes the length scale of 1 kpc at the distance of the galaxy.

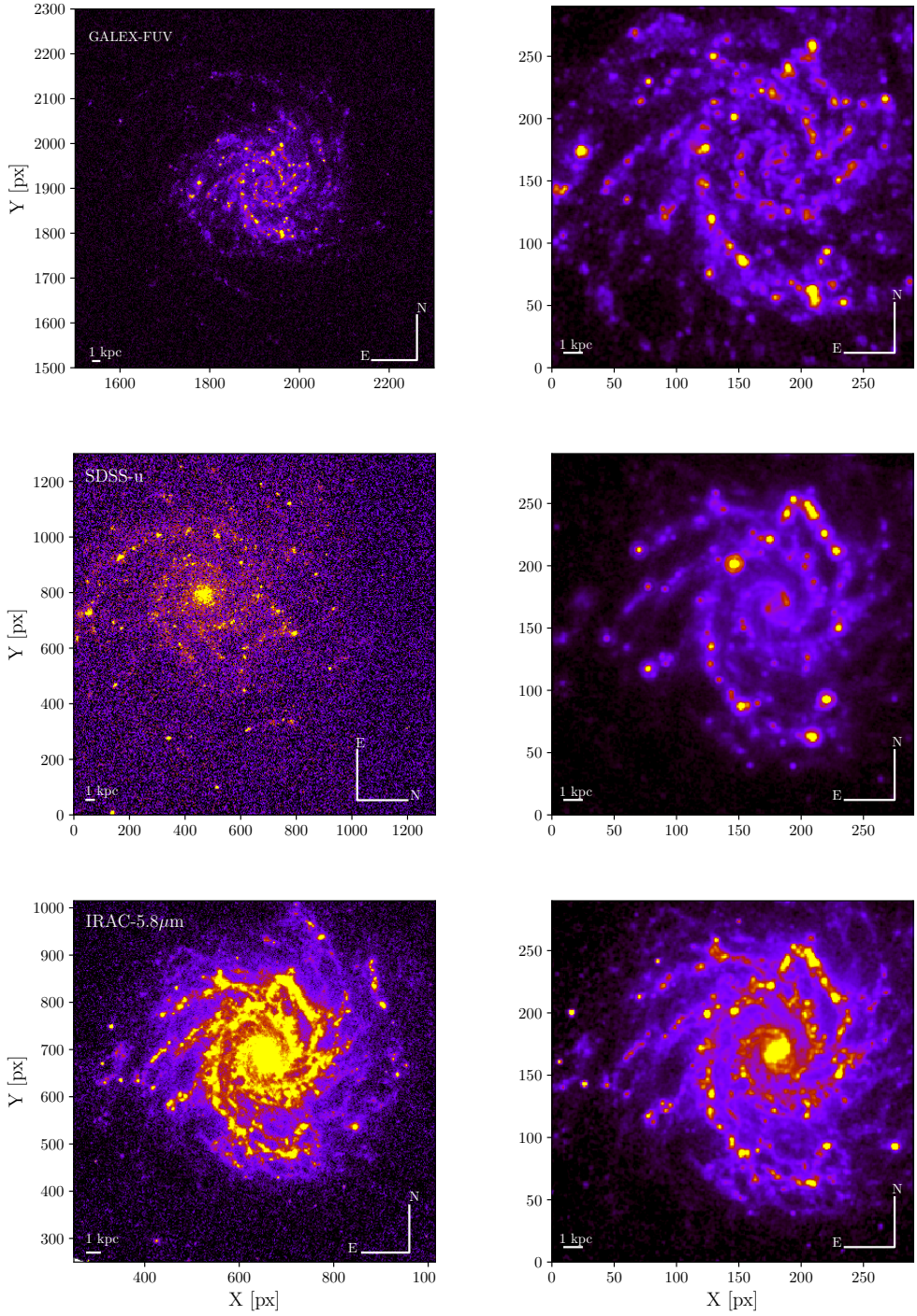

Figure 4.3.2: Same as Fig. 4.3.1, but for NGC 628.

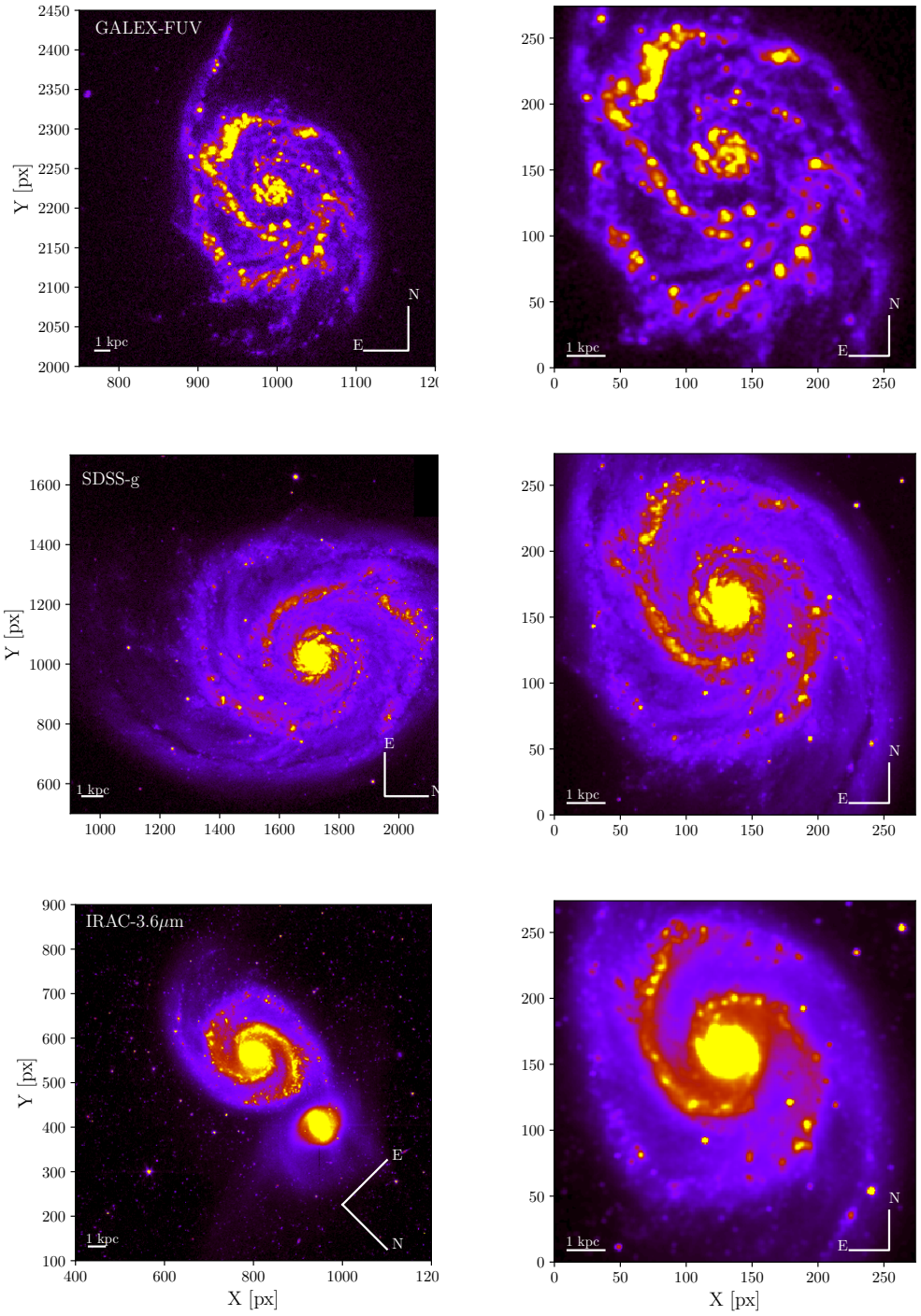

Figure 4.3.3: Same as Fig. 4.3.1, but for M51a.

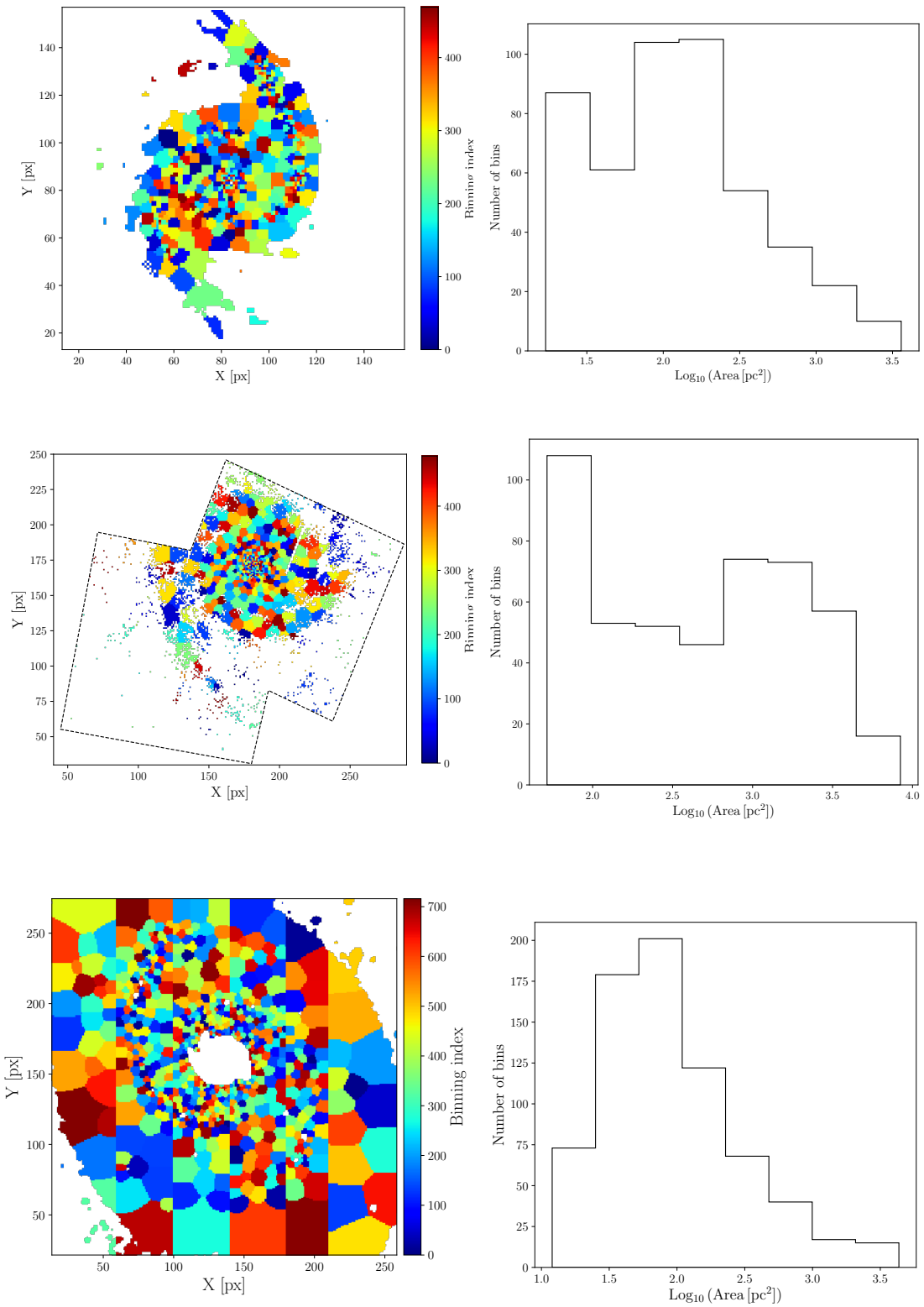

Figure 4.3.4: Left-hand panels: The Voronoi binning map of NGC 1566, NGC 628, and M51a from top to bottom, respectively. The colour bar shows the index number of each bin. Right-hand panels: The distribution of the adopted bins in area in units of pc^2 for each galaxy.

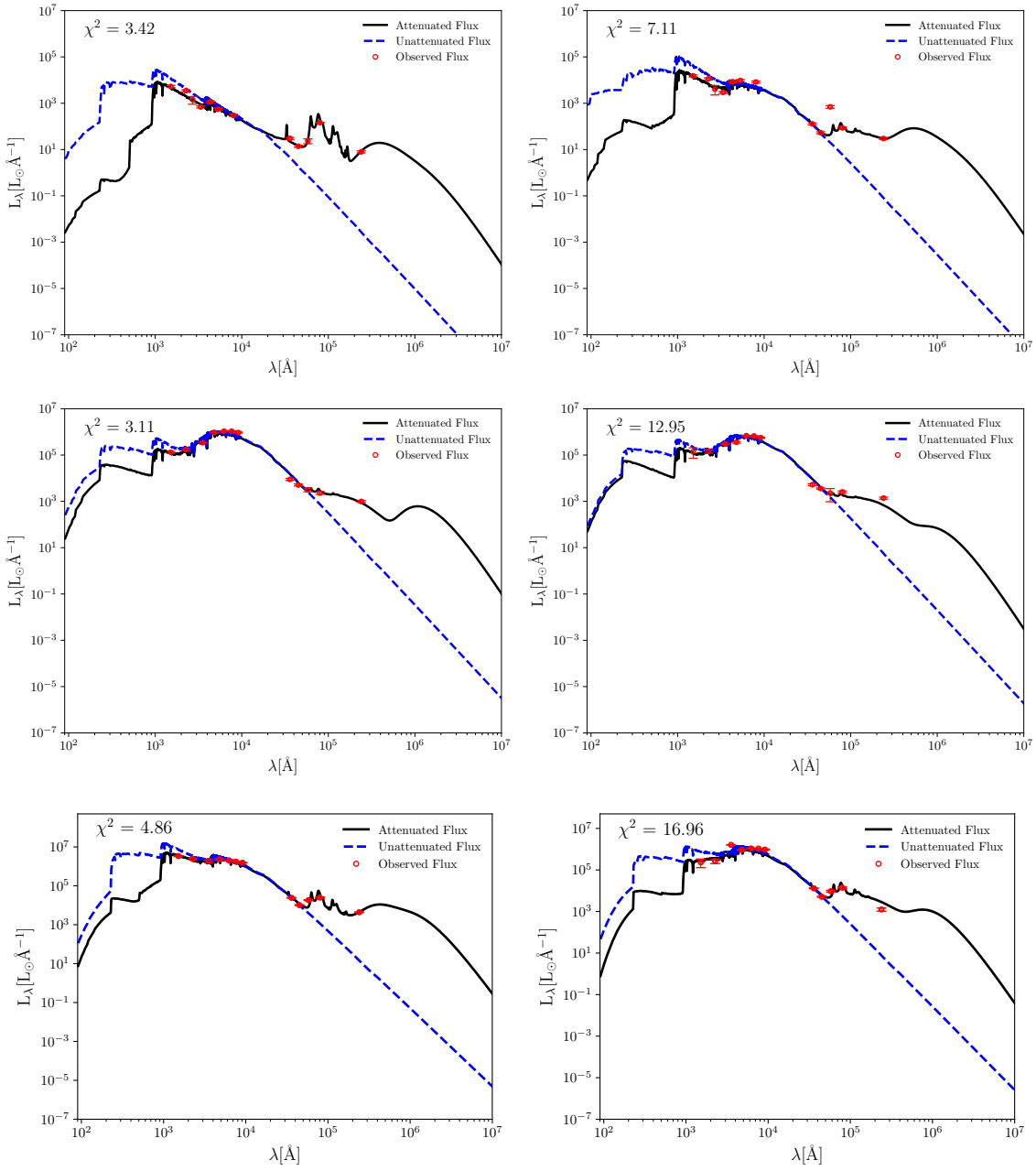

Figure 4.3.5: Example of observed SEDs and MAGPHYS good (left-hand column) and poor fits (right-hand column) for NGC 1566, NGC 628, and M51a (from top to bottom, respectively). The black solid and red dashed lines represent the attenuated and unattenuated SEDs, respectively. The observed SED data points are shown as red circles.

This map highlights the lopsidedness in the distribution of the SFR surface density in the western and eastern parts of the galaxy. The SFR is intensely concentrated along the western arm (Arm 1) while it barely traces the eastern arm (Arm 2). However, we detect some bright bins with a high SFR surface density value in the inter-arm region located in the eastern part of the galaxy and close to Arm 2, where the young star clusters tend to clump together (refer to Fig. 4.2.1). Furthermore, we note that Arm 2 is significantly shorter and less extended in the SFR surface density map in comparison to Arm 1.

The quantitative comparison of SFR surface density in the two prominent spiral arms of NGC 1566 is shown in the top left-hand panel of Fig. 4.4.3. The histogram illustrates that Arm 1 has a relatively higher SFR surface density than Arm 2. This is particularly evident for SFR surface density higher than 6.76×10^{-5} $\mathrm{M_{\odot}\,yr^{-1}\,kpc^{-2}}$. These regions encompass 44% of the SFR surface density bins associated with Arm 1, and only 9.46% in Arm 2. The result of our K-S test with a derived p-value of 1.92×10^{-5} confirms that the two spiral arms are significantly different in their SFR surface density distribution.

Fig. 4.4.2 presents the spatially resolved map of the stellar mass surface density and its error map for NGC 1566. The stellar mass surface density in this galaxy is higher in the nucleus and gradually decreases toward the outer regions. Although the two main spiral arms are smoothed out in their stellar mass surface density distribution, they can be still distinguished from their neighboring inter-arm regions due to their higher stellar mass surface densities.

The top left-hand histogram of Fig. 4.4.3 suggests that the two spiral arms have a somewhat similar distribution in their stellar mass surface density. The derived p-value of our two-sample K-S test (0.39) is more significant than the test's significance level (0.05) of the null hypothesis, meaning that the two spiral arms are likely drawn from the same distribution.

4.4.2 NGC 628

The derived SFR surface density map together with the uncertainty map of NGC 628 is shown in the top panel of Fig. 4.4.4. This map traces some star-forming regions along Arm 1 and the northern part of Arm 2. We do not observe any significant difference in the SFR surface density between these two regions. The SFR surface density decreases in the eastern part of the Arm 2 and then sharply increases in the southern region. Additionally, some of the spurs associated with the inner spiral arms, which are visible in the optical images, can be detected in the SFR surface density map.

To examine the discrepancy in the SFR surface density in the two main spiral arms, we quantify the distribution of the SFR surface density along Arm 1 and Arm 2 (middle left-hand panel of Fig. 4.4.3). Our results do not show any lopsidedness in the distribution of the SFR surface density. The two distributions are quite analogous. The main difference between the distributions of SFR surface density in the two arms is that Arm 2 has regions with higher SFR surface density in its southern outskirts. The two-sample K-S test with the p-value of 0.39 indicates that these two distributions are likely drawn from the same population.

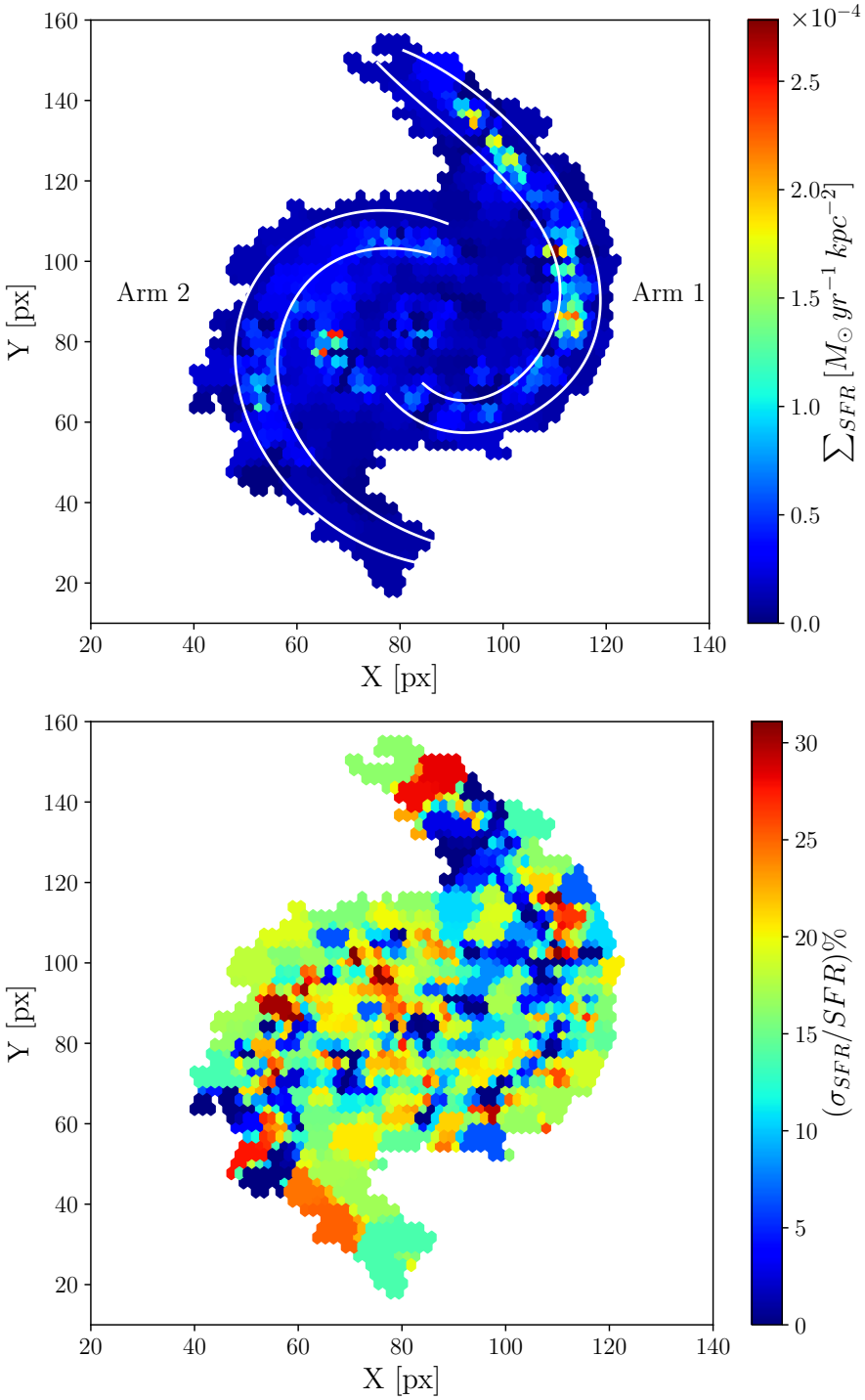

Figure 4.4.1: The SFR surface density (upper panel) and the uncertainty of SFR surface density map (bottom panel) resulting from pixel-by-pixel SED fitting. Different SFR surface densities are encoded with different colours, as given in the bar on the right. The spiral arms are overplotted on the SFR surface density map. North is up and east is to the left.

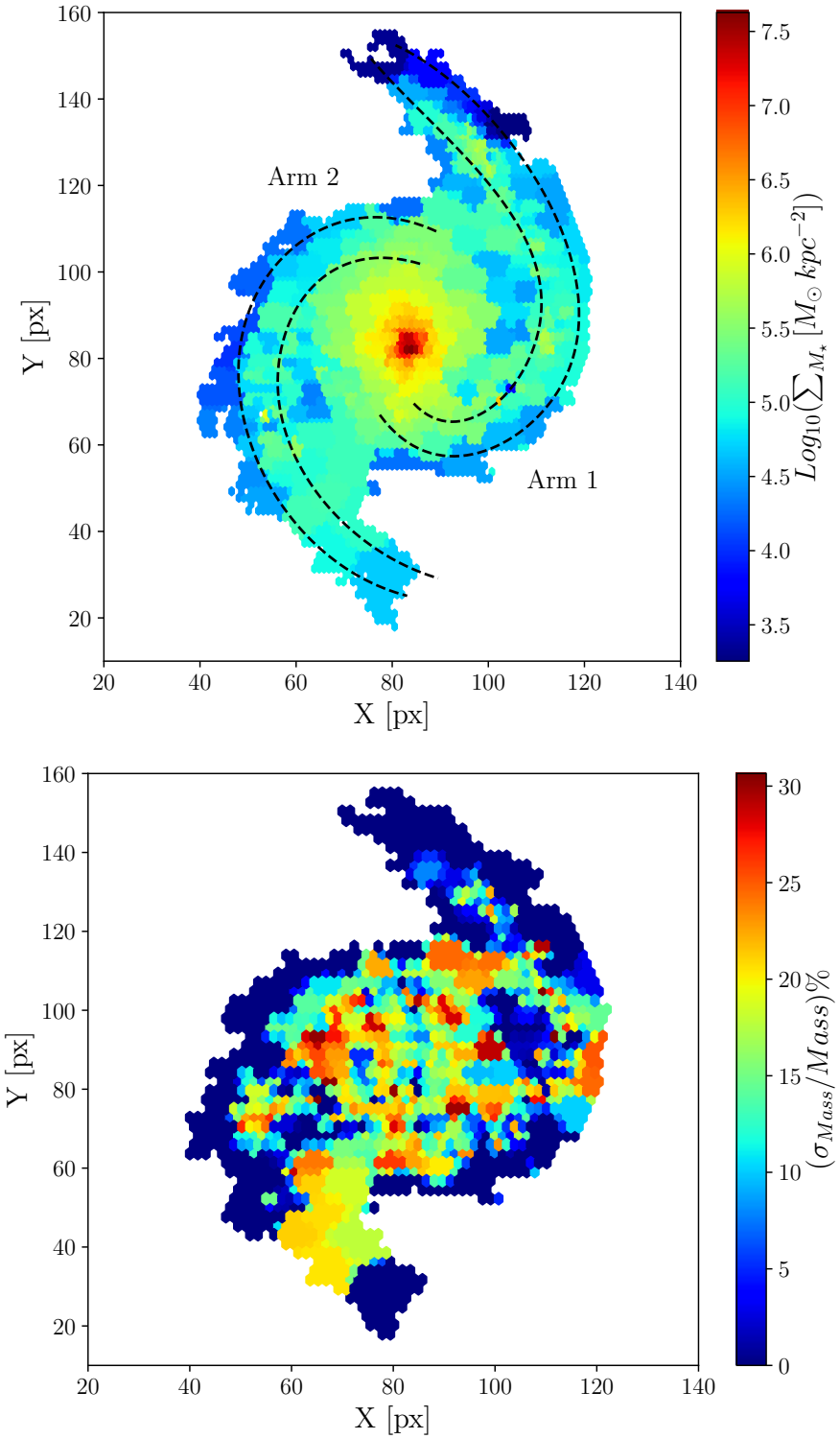

Figure 4.4.2: Same as Fig. 4.4.1 but for the stellar mass parameter.

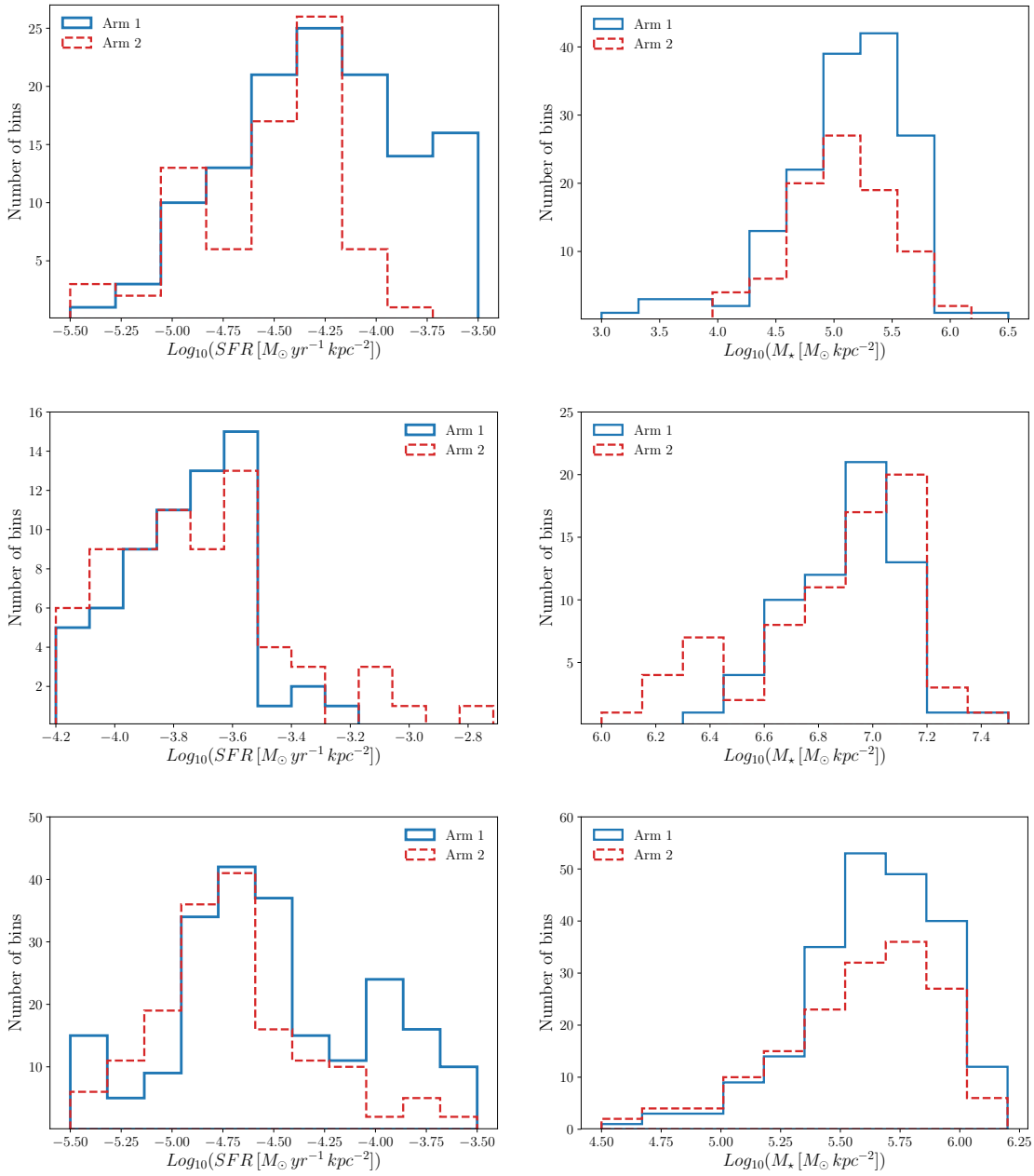

Figure 4.4.3: The distribution of the SFR (left-hand panels) and stellar mass (right-hand panels) surface density in Arm 1 (blue solid line) and Arm 2 (red dashed line) of NGC 1566, NGC 628, and M51a (from top to bottom, respectively).

In Fig. 4.4.5, we present the spatially resolved stellar mass surface density map of NGC 628. Similar to the case of NGC 1566, the stellar mass surface density map shows a very smooth distribution, which peaks in the center of the galaxy and declines outwards. Further, we do not detect any star-forming spiral patterns in the stellar mass surface density map. The quantitative distribution in stellar mass surface density along Arm 1 and Arm 2 (middle right-hand panel of Fig. 4.4.3) shows that two arms have a very similar distribution of the stellar mass surface density. The derived p-value of 0.30 confirms that the distribution of mass surface density is similar in both arms.

4.4.3 M51a

Fig. 4.4.6 shows the derived SFR surface density map (upper panel) and its corresponding uncertainty map (lower panel) for M51a. This map indicates that the SFR surface density along the two spiral arms in the inner regions of the galaxy (R $<$ 9 kpc) is higher than in the outer regions. This is particularly noticeable for Arm 1, which can be clearly traced in the SFR surface density map. As we move along the two arms toward their outskirts, the SFR surface density decreases, and the arms fade and become invisible in their SFR surface density distribution. We also observe some high star-forming regions connected to the northern part of Arm 1. The left-hand panel of the bottom row in Fig. 4.4.3 quantifies the distribution of the SFR surface density along the two arms of M51a. As we discussed before, we visually removed the bins with more than 50% of their area outside the spiral arms and considered them to belong to inter-arm regions. The histogram shows that the SFR surface density distribution along Arm 1 peaks at high ($\sim 10^{-4}$) and low ($\sim 1.78\times10^{-5}$) SFR surface density values in units of $\mathrm{M_\odot\,yr^{-1}\,kpc^{-2}}$ corresponding to the SFR surface density peaks in the inner and outer regions, respectively. In addition, we observe that Arm 1 has a higher number of bins with a SFR value higher than 10^{-4} $\mathrm{M_\odot\,yr^{-1}\,kpc^{-2}}$ ($\sim$ 23% of the total bins) in comparison with Arm 2 ($\sim$ 6% of the total bins). The derived p-value of the two sample K-S (3.36 $\times10^{-6}$) confirms that these two arms are different in their SFR surface density distribution.

The derived stellar mass surface density map of M51a and its error map are shown in Fig. 4.4.7. Although we have masked the central regions of the galaxy in order to decrease the number of Voronoi bins, it is still evident that the stellar mass surface density is higher in the center of the galaxy and decreasing toward the outskirts. It is worth noting that the spiral arms in the inner regions of the galaxy can be distinctly detected in the stellar mass surface density map. The right-hand panel of the bottom row in Fig. 4.4.3 and the K-S test do not show any significant discrepancy between the stellar mass surface density distribution along the two arms (with a p-value of 0.23).

4.5 Discussion and conclusions

In this chapter, we perform a new study of the asymmetry present in the distribution of star clusters along the main spiral arms of the investigated galaxies and its possible connection to

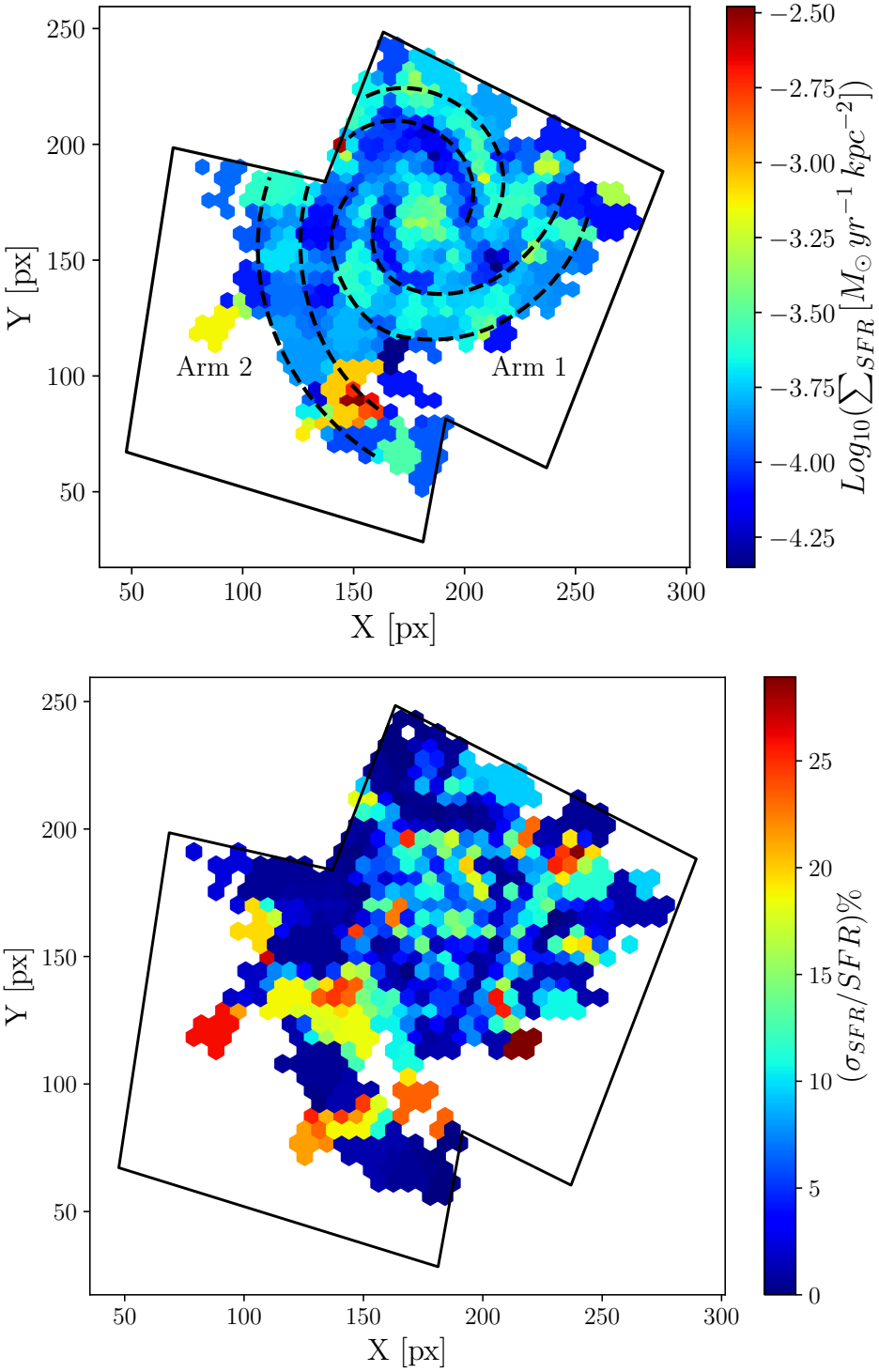

Figure 4.4.4: Same as Fig. 4.4.1 but for NGC 628.

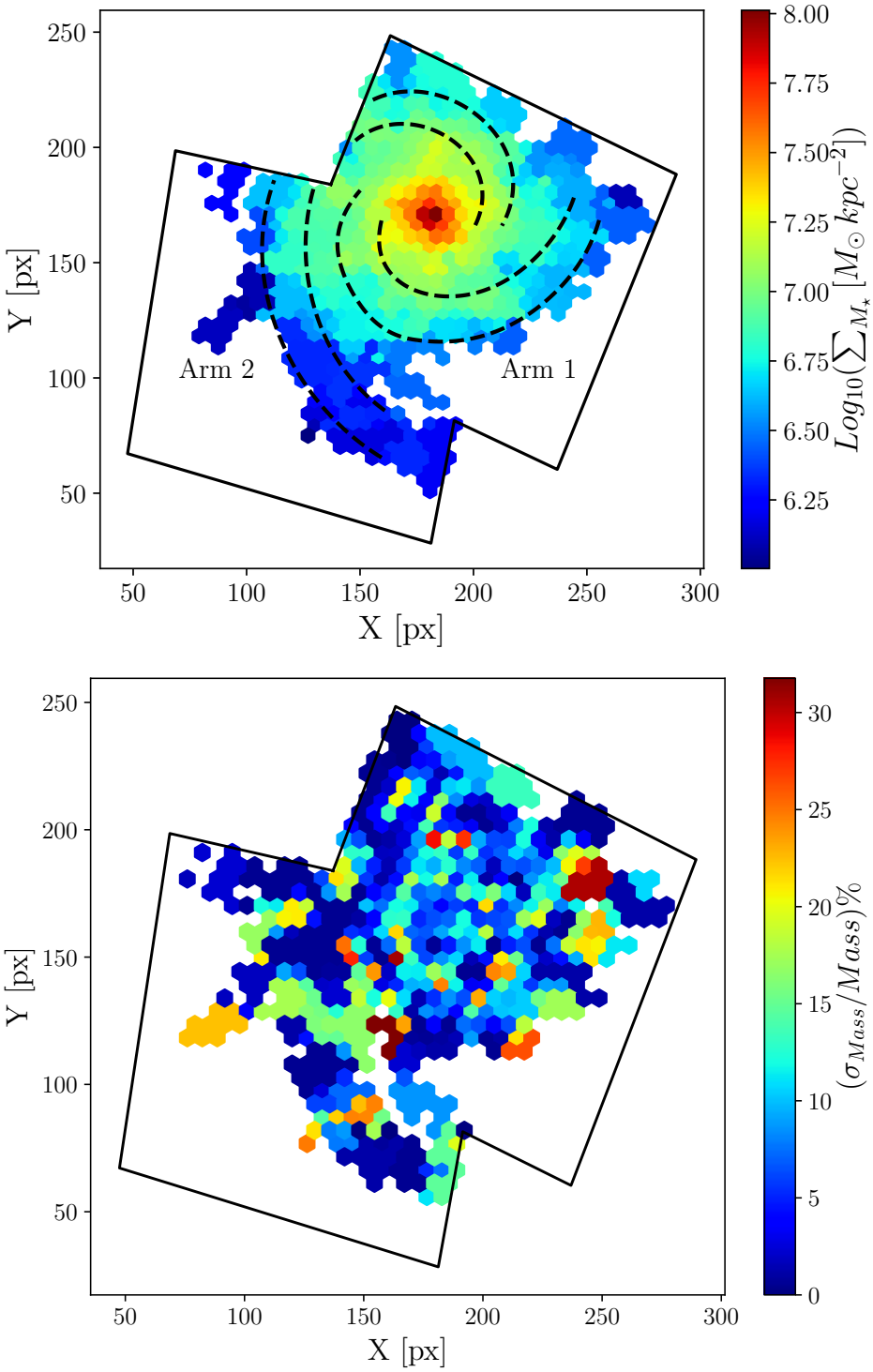

Figure 4.4.5: Same as Fig. 4.4.2 but for NGC 628.

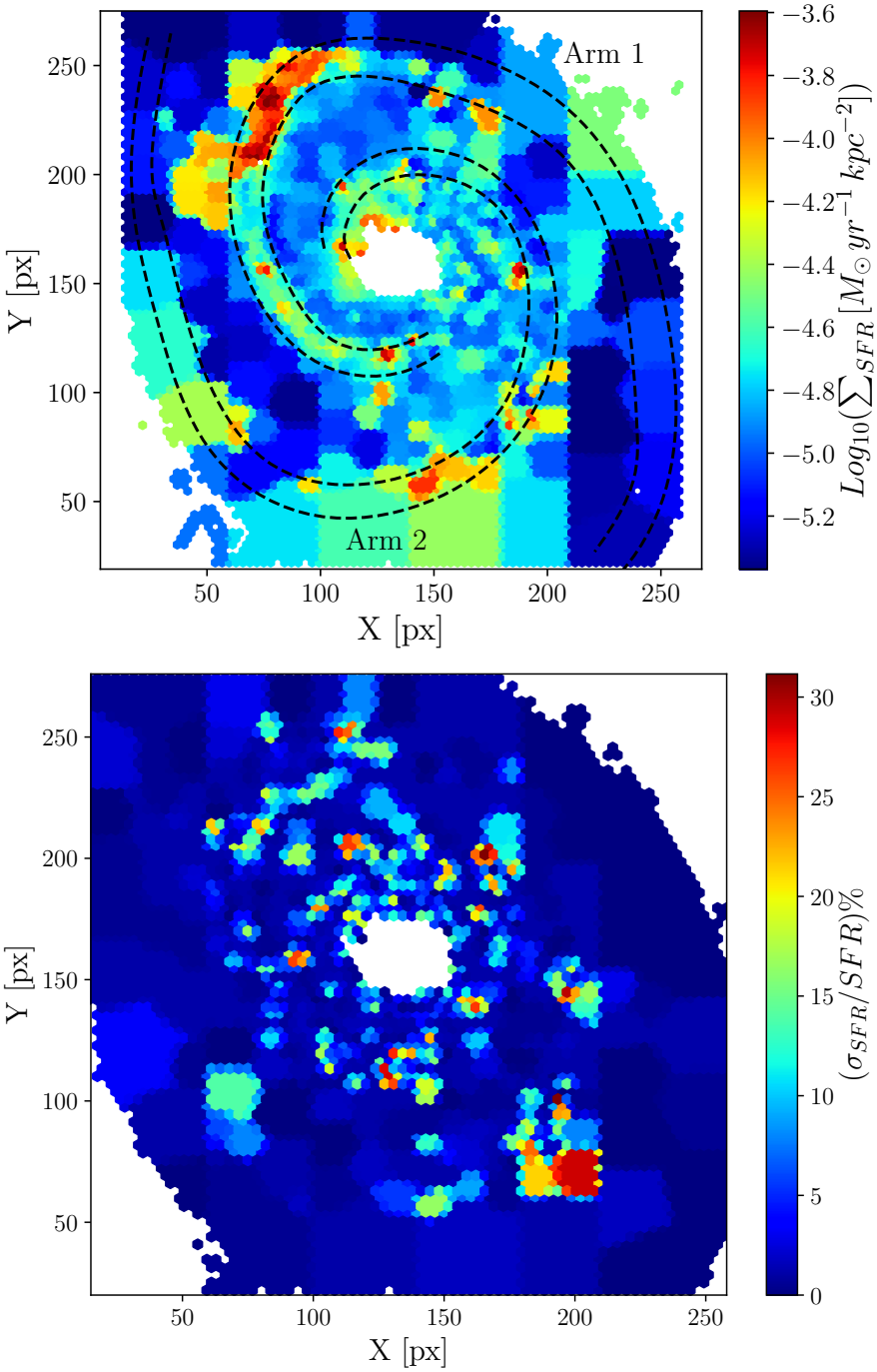

Figure 4.4.6: Same as Fig. 4.4.1 but for M51a.

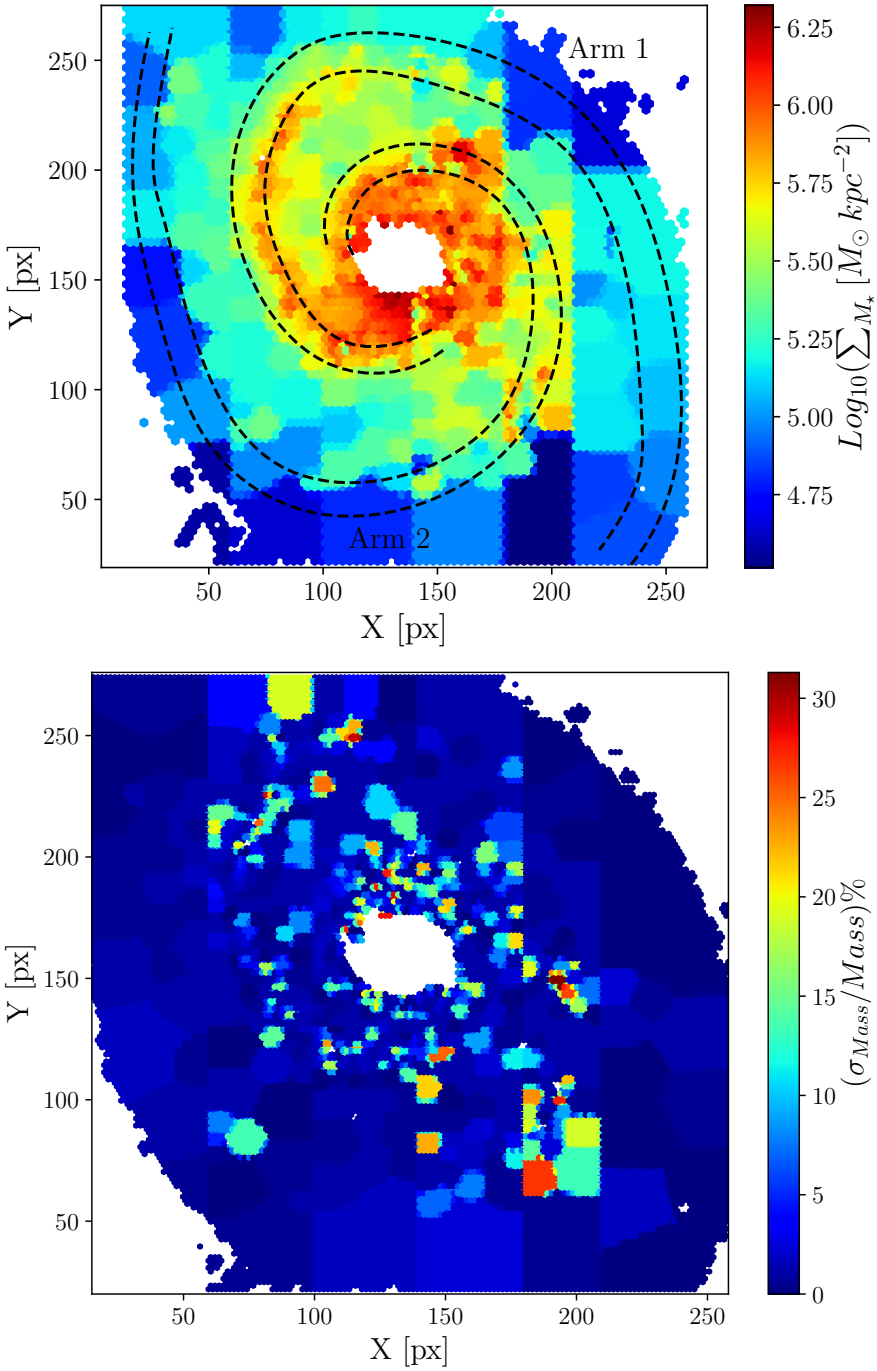

Figure 4.4.7: Same as Fig. 4.4.2 but for M 51.

the underlying SFR and stellar mass surface density distribution on sub-kpc scales. In order to construct the spatially resolved SFR and stellar mass surface density maps, we made use of multi-wavelength images (from UV to IR) of the host galaxy and modeled the observed SEDs with the MAGPHYS code on a pixel-by-pixel basis. Our main results and conclusions are as follows:

NGC 1566: We observed that young star clusters are highly concentrated along the western inner arm of NGC 1566 than along its eastern arm. The prominent spiral arms of the galaxy are slightly smoothed out in the derived stellar mass surface density map, and we do not find any obvious sign of lopsidedness in their stellar mass surface density distribution. On the contrary, our 2D resolved SFR surface density map highlights the presence of lopsidedness between the western and eastern arm in a similar fashion to the distribution of the young star clusters.

Recently, Elagali et al. (2019) presented a detailed study of the HI gas in NGC 1566 using the Australian Square Kilometer Array Pathfinder (ASKAP) radio telescope. They found that the HI gas is mainly located in the inner arms, and its surface density smoothly declines toward the outer regions. Furthermore, their results indicate the existence of a significant lopsidedness in the HI gas distribution between the eastern and western sides of the galaxy. As can be seen in Fig.4.5.1, the HI gas density column contours appear denser on the eastern side of the galaxy than in its western part, where the HI contours are dispersed and spread out up to 50 kpc. In addition, the distribution of the HI gas in the inner region of the galaxy (which is covered by the LEGUS observations) looks quite symmetric. This is not surprising since the HI disks are usually more extended and spread than the optical disks and thus can more easily be affected by external effects such as interactions with the neighboring galaxies (Braun and Thilker 2004; Michel-Dansac et al. 2010; Elagali et al. 2019). As a result, the lopsidedness appears stronger in the outer regions (Rix and Zaritsky 1995).

As we discussed in Section 1.3, lopsidedness might be a signature of interaction or merger with a companion, of gas accretion from outside the galaxy, and/or of ram pressure interactions with the inter-galactic medium. Elagali et al. (2019) examined these scenarios to understand the main mechanism responsible for the lopsidedness seen in the HI gas of NGC 1566.

NGC 1566 is a member of the Dorado Group, with its nearest candidate for tidal interaction being interacting pair NGC 1596 (SA0 spiral galaxy) and NGC 1602 (dwarf irregular galaxy) (Chung et al. 2006) located at a projected distance of 700 kpc. Elagali et al. (2019) did not detect any HI tail/bridge structure in the column density map of the NGC 1566 mosaic that might have been a result of a possible interaction between NGC 1566 and its two neighboring galaxies. Elagali et al. (2019) also used a deep optical image of NGC 1566 taken at the Australian Astronomical Observatory to search for possible faint stellar sub-structures or streams around NGC 1566. Such structures might be a result of tidal interactions or a minor merger with a neighboring galaxy and can form on a time-scale of 10^8 years and survive for few Gyr (Hernquist and Quinn 1989). However, Elagali et al. (2019) did not find any sign for the presence of the faint structures, and thus, concluded that a recent interaction is not likely to cause the observed lopsidedness in the distribution of HI in NGC 1566.

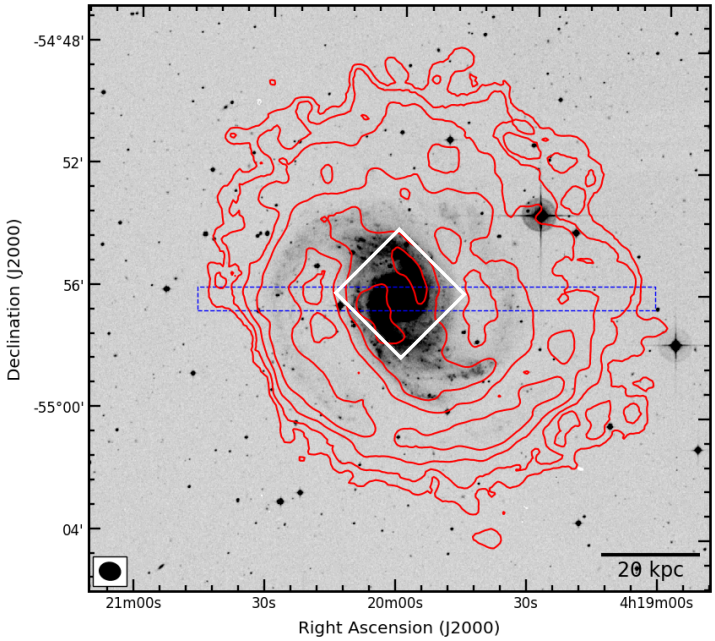

Figure 4.5.1: The HI column density contours from ASKAP observations overplotted on the DSS blue image of NGC 1566. We have added the LEGUS WFC3 footprint to the figure (the white box). North is up and East is to the left. Figure credit: Fig. 7 in Elagali et al. (2019).

Alternatively, the existence of cold gas filaments that get accreted on to galaxies has also been proposed as a possible mechanism for the origin of lopsidedness (Bournaud et al. 2005a; de Blok et al. 2014). In the case of NGC 1566, Elagali et al. (2019) did not identify any filaments related to the HI disk or in its vicinity as a signature for gas accretion. However, they stressed that their results could not completely rule out gas accretion as a possible scenario for the lopsidedness of NGC 1566 due to the low sensitivity of ASKAP at HI column densities below 10^{18} cm^{-2}. Further, Elagali et al. (2019) investigated the hypothesis that lopsidedness in the outer gaseous disk of NGC 1566 is induced by ram pressure stripping. They implemented a simple analytical model proposed by Gunn and Gott (1972), varying the density of IGM and the relative velocity of the galaxy, and showed that ram pressure stripping as a consequence of its interaction with the IGM can possibly cause the lopsidedness in the gas morphology of NGC 1566.

Mapelli et al. (2008) carried out a simulation study of the three potential scenarios responsible for the lopsidedness of spiral galaxies and discussed the asymmetry in their gaseous and stellar components. They found that different mechanisms produce different degrees of lopsidedness. For instance, in the case of gas accretion, the observed asymmetry in the distribution of gas is significantly higher than in the other two scenarios (top panel of Fig. 4.5.2). Further, the young stellar component with an age < 100 Myr seems to be clearly lopsided (bottom panel of Fig. 4.5.2), while the total stellar population does not appear asymmetric (the middle panel of Fig. 4.5.2). They claimed that this might be due to the fact that gas

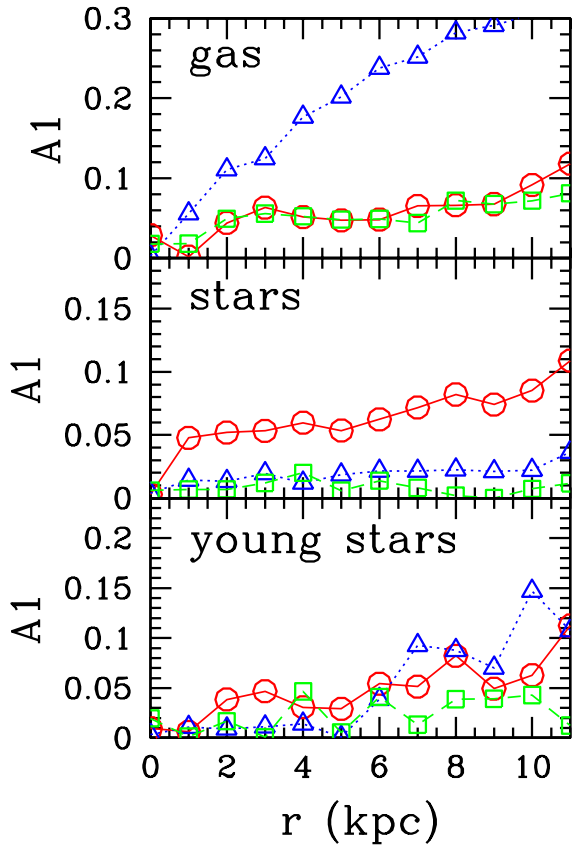

Figure 4.5.2: The degree of lopsidedness as a function of radius for gas (top panel), total stellar component (middle panel), and young stellar content (bottom panel). The red open circles, the blue open triangles, and the green open squares correspond to three different simulated processes, flyby interaction, gas accretion, and ram pressure mechanisms, respectively. Figure credit: Fig. 10 in Mapelli et al. (2008).

accretion only affects the gas distribution in the galaxy and leads to its lopsidedness. Subsequently, new stars form along the lopsided gas distribution and give rise to an asymmetric spatial distribution of the young stellar population. Therefore, the asymmetry in the young stellar population distribution can be considered as a consequence of the pre-existing lopsidedness in the gas component. In addition, their simulations indicate that ram pressure stripping is not able to induce asymmetry in the global and young stellar contents.

As we discussed, our results indicate the existence of lopsidedness in the distribution of the young star clusters (age < 10 Myr) and SFR surface density in the western and eastern sides of NGC 1566. However, it is interesting to look at the distribution of the global and young (age < 100 Myr) stellar contents along the two spiral arms and compare it with the simulations of Mapelli et al. (2008). We do not observe any significant asymmetry between the number density of all stellar clusters and the young ones along the two spiral arms of

the galaxy. Therefore, our finding is similar to the simulated lopsidedness induced by ram pressure.

NGC 628: Our observational study of the spatial distribution of star clusters along the two inner arms of NGC 628 shows evidence of the presence of lopsidedness in the distribution of intermediate-age and old star clusters. However, we stress that the LEGUS observations do not cover the whole inner region of the galaxy and our results might be biased due to the missing star clusters or the low number statistics of the young clusters. Lopsidedness in the distribution of the old stellar populations was observed in a pioneering study by Block et al. (1994). They detected an asymmetry in the distribution of the old stars by mapping NGC 2997 and NGC 1637 in the near-IR. The dust extinction does not significantly affect the emission in the near-IR, and hence it can be used as a good tracer of the underlying old stellar population, which dominates the stellar mass budget of the disk. Later on, Rix and Zaritsky (1995) quantified the lopsidedness in the near-IR emission for a sample of 18 galaxies and found that at least 30% of the galaxies are asymmetric in the distribution of their stellar mass.

Our results of the derived 2D spatially resolved SFR and stellar mass surface density maps of NGC 628 show a fairly analogous distribution along the two arms. The main difference in the SFR and stellar mass surface density among the two arms of NGC 628 is seen in the southern region in Arm 2, which leads to a very weak lopsidedness in the galaxy. Our finding may support the results of the Zaritsky et al. (2013) who found that there is a correlation between lopsidedness and the character of the spiral arms, meaning that moving from grand-design spiral galaxies (with the strongest arms) toward flocculent galaxies (with the weakest arms) lopsidedness become weaker. While asymmetry in the distribution of the old star clusters has been observed in NGC 628, we do not find any clear connection between the observed lopsidedness and galaxy's physical properties such as SFR and stellar mass surface density.

M51a: Interaction with a companion galaxy has been proposed as a mechanism that can induce lopsidedness in disk galaxies. For instance, the stellar disk of M51a was found to be lopsided due to the interaction with its companion (Rix and Rieke 1993). Later, Odewahn (1994) carried out an observational study of a sample of 75 lopsided Magellanic spirals and found 71 of them to have a nearby companion. Walker et al. (1996) showed that a minor merger with a companion galaxy produces disk lopsidedness in their simulations lasting over a time-scale of 1 Gyr. Later on, Wilcots and Prescott (2004) examined the distribution of the HI gas in 13 galaxies from the Odewahn (1994) sample with apparent optical companions and observed that only four of them have HI-detected companions with a minimum gas mass of $10^7 M_\odot$. Their detailed observational study of those four galaxies suggests that the ongoing interaction with companions might be responsible for the lopsided structure of the galaxy in only two cases, NGC 3664 and NGC 3995, while the detected nearby companions are not affecting the morphology of the other two galaxies, NGC 2537 and UGC 5391. Furthermore, Wilcots and Prescott (2004) did not detect any noticeable difference in the HI distribution of the galaxies with and without nearby companions leading them to conclude that either the asymmetric morphology is not correlated with the current interactions or the lopsidedness

induced by interactions are long-lived phenomenon surviving even after the companion is disrupted.

We investigated the spatial distribution of star clusters with different ages along the two prominent spiral arms of M51a. Our results show that Arm 1 (the non-interacting arm) exhibits a larger number density of the young star clusters in comparison with Arm 2 (the interacting arm). In contrast, Arm 2 is characterized by a higher number density of old star clusters than Arm 1. M51a is interacting with its companion, M51b, and thus it is interesting to examine whether the expected lopsidedness in SFR surface density (due to the interaction) is linked with the observed asymmetry in the distribution of star clusters along the two main spiral arms.

The derived SFR surface density map indicates that the two spiral arms of M51a are different. This is particularly evident in the inner regions of the galaxy ($R < 9$ kpc), where Arm 1 has a higher SFR surface density than Arm 2. Our results support the results of a high-resolution simulation of tidal encounters of a disc galaxy with a small companion done by Pettitt et al. (2017). They studied the induced spiral arm features due to the tidal encounters and found that the SFR surface density decreases towards the edge of the disk similar to the gas surface density. Further, Pettitt et al. (2017) observed that the two spiral arms appear different in their star formation histories and structure. The bridge arm (interacting arm) appears deficient in star-forming gas in comparison with the tail arm (non-interacting arm), which leads to asymmetric star formation. Also, Di Matteo et al. (2007) showed that strong interactions could excite and moderate star formation on a galactic scale due to gas stripping by the companion.

The two spiral arms of M51a seem fairly similar in the distribution of stellar mass surface density derived in this work, and we do not detect any connection between the lopsidedness in the distribution of star clusters and stellar mass surface density distribution of the galaxy.

However, as we discussed in Section 1.3, lopsidedness in galaxies has been observed to be linked with different parameters such as tracers and the environment. In this work, we do not find any clear trend between the lopsidedness in the distribution of star clusters with different ages and the physical properties of our galaxies, and our results vary from galaxy to galaxy.

5

Summary

In this thesis, we performed a study of the structure of spiral patterns in four LEGUS disk galaxies, namely NGC 1566, NGC 628, NGC 3344, and M51a, which have different morphologies. LEGUS is a Cycle 21 HST Treasury program that has observed 50 local spiral and dwarf galaxies at the distance range of $\approx$ 3.5-12 Mpc. The high-resolution images of these galaxies were collected in five broad-band filters (NUV, U, B, V, and I) with the UVIS channel of the Wide Field Camera Three (WFC3), supplemented with archival Advanced Camera for Surveys (ACS) imaging when available.

In Chapter 2, we used the age and position of the star clusters, identified and measured by the LEGUS team in the sample galaxies, within the LEGUS team, as a tool to examine whether the spiral patterns in the galaxies NGC 1566, M51a, and NGC 628 are are consistent with the predictions of the stationary density wave theory. The spiral density wave theory is one of the leading theories for explaining the generation of spiral patterns in disk galaxies and predicts the existence of an age gradient across the arms. To test for the possible existence of an age sequence across the spiral arms, we quantified the azimuthal offset between star clusters of different ages in our target galaxies. We found that NGC 1566, a grand-design spiral galaxy with bisymmetric arms and a strong bar, shows a significant age gradient across the spiral arms that appears to be consistent with the predictions of the stationary density wave theory. In contrast, M51a with its two well-defined spiral arms and a weaker bar does not show an age gradient across the arms. In addition, a comparison with non-LEGUS star cluster catalogs for M51a yields similar results. We believe that the spiral structure of M51a is not the result of a stationary density wave with a fixed pattern speed. Instead, tidal interactions could be the dominant mechanism for the formation of the spiral arms in this galaxy. We also found no offset in the azimuthal distribution of star clusters with different ages across the weak spiral arms of the multi-armed galaxy NGC 628.

In Chapter 3, we present a new study of the lopsidedness in the distribution of the young star clusters (age < 10 Myr) along the two primary arms of NGC 3344. We observed that one spiral arm (the southern one, Arm 1) has a higher number density of young star clusters ($\approx$ 2 times more) than the other arm (the eastern one, Arm 2). We investigated whether there is a connection between the asymmetric distribution of the star clusters with the galaxy's physical properties (e.g., stellar mass and SFR). For this purpose, we applied a pixel-by-pixel spectral energy distribution (SED) fitting technique using broad-band photometry from UV to IR images. We used the SED fitting tool, MAGPHYS, which fits an observed SED with an extensive library of optical to infrared model SEDs. Also, we studied the impact of the chosen filters on the derived physical properties. We find that the spiral structure of the galaxy is considerably smoothed out in the stellar mass surface density map, where the arms are no longer visible and distinguishable. We do not observe any significant difference between the stellar mass surface density distribution of the two spiral arms. Furthermore, we see that the SFR surface density distribution of the young star cluster-rich arm extends to higher values, and the eastern part of the galaxy has higher SFR surface density than the western region and thus indicating lopsidedness in the SFR surface density. However, a limiting factor in understanding whether this difference is due to a different recent star formation history or a different gas content is the scarcity of public high-resolution HI and CO observations of the galaxy.

In Chapter 4, we extended the study of lopsidedness in the distribution of star clusters and its possible link with the stellar mass and SFR surface density to three LEGUS disk galaxies, NGC 1566, NGC 628, and M51a. We found that young star clusters are mainly located along the western inner arm of NGC 1566 as opposed to its eastern arm. The grand-design spiral arms of the galaxy are slightly smoothed out in the derived spatially resolved stellar mass surface density map, and we do not observe any clue to lopsidedness in their stellar mass surface density distribution. In contrast, the resolved SFR surface density map indicates the presence of lopsidedness between the western and eastern arm in a similar fashion to the distribution of the young star clusters. Therefore, our results suggest that there is a connection between the asymmetry in the distribution of young star clusters and lopsidedness in the SFR surface density in the grand-design spiral galaxy, NGC 1566. In the case of NGC 628, we found that the distribution of the old star clusters (age > 100 Myr) among the two primary inner arms is asymmetric. It is important to note that the LEGUS observations do not cover the whole inner region of NGC 628, and our results might be biased due to the missing star clusters. The distribution of the stellar mass and SFR surface density in the derived 2D spatially resolved maps show a somewhat analogous distribution along the two arms. We did not find any obvious trend between the observed lopsidedness in the distribution of old star clusters and the stellar mass and/or SFR surface density. Our observations of the spatial distribution of star clusters in M51a shows that the number density of young star clusters in the non-interacting spiral arm (Arm 1) is higher than in the interacting one (Arm 2). The derived SFR surface density map of M51a shows that the two spiral arms are different in their on-going star formation activity. This is particularly obvious in the inner regions of the galaxy (R < 9 kpc), where Arm 1 has a higher SFR surface density than Arm 2. As we discussed in Chapter 1, the interaction with a companion galaxy might be the main mechanism

to generate lopsidedness in SFR in interacting systems such as M51a. In addition, the two spiral arms of M51a seem fairly similar in the distribution of stellar mass surface density. We did not detect any connection between the lopsidedness in the distribution of star clusters and stellar mass surface density of the galaxy.

In order to search for the correlation between the possible lopsidedness in the distribution of star clusters with different ages and the physical properties in different galaxies, one would need a larger sample of galaxies with different morphologies, or in different environments (e.g., isolated field spiral galaxies, the galaxy groups, or the outskirts of Virgo cluster). The physical properties of galaxies (e.g., SFR and stellar mass surface density) can be constructed using multi-wavelength images from GALXEX, SDSS, HST, Large Synoptic Survey Telescope (LSST), The UKIRT InfraRed Deep Sky Surveys (UKIDSS), and Spitzer. And finally, the derived stellar mass and SFR surface density maps can be compared with the simulations such as IllustrisTNG to study the properties of spiral arms as a function of their star formation history, mass assembly, and environment since they are clearly well known in the simulations.

Acknowledgments

I would like to dedicate the final note to my thesis to all the wonderful people who have accompanied me for the past three years.

First of all, I would like to thank my supervisor, Eva Grebel. Thank you for giving me the opportunity to experience my PhD time in your research group at ARI and for granting me enough freedom to work on the projects according to my interests. I am incredibly grateful to all your support, encouragement, and guidance during my PhD and for your fruitful comments on the draft of my papers and thesis.

I would like to express my deepest appreciation to my advisor, Anna Pasquali, who guided me through every step from the beginning to the end. Words can not describe how grateful I am for your scientifically and personally outstanding support and encouragement during my PhD and for always trying to make me see what is important. I always enjoyed the interesting scientific and non-scientific discussions we have had. Thank you for always listening, understanding, sharing your personal experiences, and for your advice.

I would like to extend my sincere thanks to Jay Gallagher, who gave interesting thoughts on my projects, as well as being a member of my thesis committee. A special thanks go to the LEGUS team, this thesis would not be possible without the valuable work from all of its members. I want to especially thank Daniela Calzetti, Bruce Elmegreen, and Angela Adamo for their fruitful discussions and comments on my projects. I am also thankful to Sabine Reffert for kindly agreeing to be the second referee of this thesis, and to Joachim Wambsganß and Mario Trieloff for agreeing to be part of the examination committee. Thanks to Christian Fendt for all his efforts in coordinating the International Max Planck Research School (IMPRS) and for his support.

My warmest thanks go to Bahar Bidaran and Michael Hanke. Thank you for the great friendships, help, funny moments, and every single memory. I would also like to express my gratitude to Ali Dariush. Thank you for your continuous support, encouragement, and very constructive and helpful feedback and advice over the past five years.

Many thanks to all my beloved friends, who always supported me and with whom I have had a lot of cheerful moments. Especially, I would like to thank Parinaz Mosadeghi, Maryam Saberi, Reyhaneh Zandian, Sina Batebi, Tahere Naderi, Mohammad Fallahi, and Laleh Mollazadeh.

I would also like to thank my friends here in Heidelberg for being part of my PhD life. I am grateful, in particular, to Maria Cordero, Carolin Wittmann, Peter Zeidler, Reza Moetaze-

dian, Clio Bertelli Motta, Sara Rezaei Khoshbakht, Melanie Chevance, Maya Petkova, Josefina Michea, Sarah Jeffreson, Marta Reina-Campos, Alex Hygate, Daniel Haydon, Matteo Mazzarini, Jonas Klüter, Thomas Jackson, and Gustavo Medina Toledo.

This journey would have not been possible without the support of the ones I once left. I am deeply indebted to my parents and my beloved sisters, Marziyeh and Raziyeh. Your comfort and love have guided me through this journey. Thanks for all your encouragement, kindness, and sacrifices. My dear Zdeněk, thank you for being by my side in the most stressful phases of the PhD, and for your endless support and patience.

This work is based on observations made with the NASA/ESA Hubble Space Telescope, obtained at the Space Telescope Science Institute, which is operated by the Association of Universities for Research in Astronomy, Inc., under NASA contract NAS 5-26555. These observations are associated with program 13364. Support for Program 13364 was provided by NASA through a grant from the Space Telescope Science Institute. This research has made use of the NASA/IPAC Extragalactic Database (NED), which is operated by the Jet Propulsion Laboratory, California Institute of Technology, under contract with the National Aeronautics and Space Administration.

References

Abdurro'uf and Akiyama, M. (2017). Understanding the scatter in the spatially resolved star formation main sequence of local massive spiral galaxies. *MNRAS*, 469, 2806.

Abdurro'uf, Masayuki, A. (2018). Evolution of spatially resolved star formation main sequence and surface density profiles in massive disc galaxies at 0 z 1: inside-out stellar mass buildup and quenching. *MNRAS*, 479, 5083.

Abraham, R. G., Ellis, R. S., Fabian, A. C., Tanvir, N. R., and Glazebrook, K. (1999). The star formation history of the Hubble sequence: spatially resolved colour distributions of intermediate-redshift galaxies in the Hubble Deep Field. *MNRAS*, 303, 641.

Acreman, D. M., Stevens, I. R., Ponman, T. J., and Sakelliou, I. (2003). Simulations of the effects of stripping and accretion on galaxy haloes in clusters. *MNRAS*, 341, 1333.

Adamo, A., Östlin, G., and Zackrisson, E. (2011). Probing cluster formation under extreme conditions: massive star clusters in blue compact galaxies. *MNRAS*, 417, 1904.

Adamo, A., Ryon, J. E., Messa, M., Kim, H., Grasha, K., Cook, D. O., Calzetti, D., Lee, J. C., Whitmore, B. C., Elmegreen, B. G., Ubeda, L., Smith, L. J., Bright, S. N., Runnholm, A., Andrews, J. E., Fumagalli, M., Goulier-mis, D. A., Kahre, L., Nair, P., Thilker, D., Walterbos, R., Wofford, A., Aloisi, A., Ashworth, G., Brown, T. M., Chandar, R., Christian, C., Cignoni, M., Clayton, G. C., Dale, D. A., de Mink, S. E., Dobbs, C., Elmegreen, D. M., Evans, A. S., Gallagher, III, J. S., Grebel, E. K., Herrero, A., Hunter, D. A., Johnson, K. E., Kennicutt, R. C., Krumholz, M. R., Lennon, D., Levay, K., Martin, C., Nota, A., Östlin, G., Pellerin, A., Prieto, J., Regan, M. W., Sabbi, E., Sacchi, E., Schaerer, D., Schiminovich, D., Shabani, F., Tosi, M., Van Dyk, S. D., and Zackrisson, E. (2017). Legacy ExtraGalactic UV Survey with The Hubble Space Telescope: Stellar Cluster Catalogs and First Insights Into Cluster Formation and Evolution in NGC 628. *ApJ*, 841, 131.

Agüero, E. L., Díaz, R. J., and Bajaja, E. (2004). <ASTROBJ>NGC 1566</ASTROBJ>: Spectroscopy of a symmetric system with Seyfert nucleus. *A&A*, 414, 453.

Alam, S., Albareti, F. D., Allende Prieto, C., Anders, F., Anderson, S. F., Anderton, T., Andrews, B. H., Armengaud, E., Aubourg, É., Bailey, S., and et al. (2015). The Eleventh and Twelfth Data Releases of the Sloan Digital Sky Survey: Final Data from SDSS-III. *ApJS*, 219, 12.

Angiras, R. A., Jog, C. J., Dwarakanath, K. S., and Verheijen, M. A. W. (2007). Spatial and kinematical lopsid-edness of atomic hydrogen in the Ursa Major group of galaxies. *MNRAS*, 378, 276.

Angiras, R. A., Jog, C. J., Omar, A., and Dwarakanath, K. S. (2006). Origin of disc lopsidedness in the Eridanus group of galaxies. *MNRAS*, 369, 1849.

Athanassoula, E. (1992). The existence and shapes of dust lanes in galactic bars. *MNRAS*, 259, 345.

Athanassoula, E. (2012). Manifold-driven spirals in N-body barred galaxy simulations. *MNRAS*, 426, L46.

Athanassoula, E., Romero-Gómez, M., Bosma, A., and Masdemont, J. J. (2009a). Rings and spirals in barred galaxies - II. Ring and spiral morphology. *MNRAS*, 400, 1706.

Athanassoula, E., Romero-Gómez, M., Bosma, A., and Masdemont, J. J. (2010). Rings and spirals in barred galaxies - III. Further comparisons and links to observations. *MNRAS*, 407, 1433.

Athanassoula, E., Romero-Gómez, M., and Masdemont, J. J. (2009b). Rings and spirals in barred galaxies - I. Building blocks. *MNRAS*, 394, 67.

Baba, J. (2015). Short-term dynamical evolution of grand-design spirals in barred galaxies. *MNRAS*, 454, 2954.

Baba, J., Asaki, Y., Makino, J., Miyoshi, M., Saitoh, T. R., and Wada, K. (2009). The Origin of Large Peculiar Motions of Star-Forming Regions and Spiral Structures of Our Galaxy. *ApJ*, 706, 471.

Baba, J., Saitoh, T. R., and Wada, K. (2013). Dynamics of Non-steady Spiral Arms in Disk Galaxies. *ApJ*, 763, 46.

Baldwin, J. E., Lynden-Bell, D., and Sancisi, R. (1980). Lopsided galaxies. *MNRAS*, 193, 313.

Barnes, J. E. (1998). Dynamics of Galaxy Interactions. In Kennicutt, Jr., R. C., Schweizer, F., Barnes, J. E., Friedli, D., Martinet, L., and Pfenniger, D., editors, *Saas-Fee Advanced Course 26: Galaxies: Interactions and Induced Star Formation*, page 275.

Beale, J. S. and Davies, R. D. (1969). Neutral Hydrogen Asymmetry in the Galaxy M101 as Evidence for Tidal Effects. *Nature*, 221, 531.

Bendo, G. J., Joseph, R. D., Wells, M., Gallais, P., Haas, M., Heras, A. M., Klaas, U., Laureijs, R. J., Leech, K., Lemke, D., Metcalfe, L., Rowan-Robinson, M., Schulz, B., and Telesco, C. (2003). Dust Temperatures in the Infrared Space Observatory Atlas of Bright Spiral Galaxies. *AJ*, 125, 2361.

Berta, S., Lutz, D., Santini, P., Wuyts, S., Rosario, D., Brisbin, D., Cooray, A., Franceschini, A., Gruppioni, C., Hatziminaoglou, E., Hwang, H. S., Le Floc'h, E., Magnelli, B., Nordon, R., Oliver, S., Page, M. J., Popesso, P., Pozzetti, L., Pozzi, F., Riguccini, L., Rodighiero, G., Roseboom, I., Scott, D., Symeonidis, M., Valtchanov, I., Viero, M., and Wang, L. (2013). Panchromatic spectral energy distributions of Herschel sources. *A&A*, 551, A100.

Bertin, E. and Arnouts, S. (1996). SExtractor: Software for source extraction. *A&AS*, 117, 393.

Bertin, G. and Lin, C. C. (1996). *Spiral structure in galaxies a density wave theory*.

Block, D. L., Bertin, G., Stockton, A., Grosbol, P., Moorwood, A. F. M., and Peletier, R. F. (1994). 2.1 μm images of the evolved stellar disk and the morphological classification of spiral galaxies. *A&A*, 288, 365.

Block, D. L., Bournaud, F., Combes, F., Puerari, I., and Buta, R. (2002). Gravitational torques in spiral galaxies: Gas accretion as a driving mechanism of galactic evolution. *A&A*, 394, L35.

Block, D. L., Buta, R., Knapen, J. H., Elmegreen, D. M., Elmegreen, B. G., and Puerari, I. (2004). Gravitational Bar and Spiral Arm Torques from K_s-band Observations and Implications for the Pattern Speeds. *AJ*, 128, 183.

Boselli, A., Boissier, S., Cortese, L., Buat, V., Hughes, T. M., and Gavazzi, G. (2009). High-mass Star Formation in Normal Late-type Galaxies: Observational Constraints to the Initial Mass Function. *ApJ*, 706, 1527.

Bothun, G. D. (1986). Two-color CCD mapping of the luminous Type I irregular galaxy NGC 4449. *AJ*, 91, 507.

Bothwell, M. S., Kennicutt, R. C., and Lee, J. C. (2009). On the interstellar medium and star formation demographics of galaxies in the local universe. *MNRAS*, 400, 154.

Bottema, R. (2003). Simulations of normal spiral galaxies. *MNRAS*, 344, 358.

Bournaud, F. and Combes, F. (2002). Gas accretion on spiral galaxies: Bar formation and renewal. *A&A*, 392, 83.

Bournaud, F., Combes, F., Jog, C. J., and Puerari, I. (2005a). Lopsided spiral galaxies: evidence for gas accretion. *A&A*.

Bournaud, F., Jog, C. J., and Combes, F. (2005b). Galaxy mergers with various mass ratios: Properties of remnants. *A&A*, 437, 69.

Braun, R. and Thilker, D. A. (2004). The WSRT wide-field H I survey. II. Local Group features. *A&A*, 417, 421.

Bruzual, G. and Charlot, S. (2003). Stellar population synthesis at the resolution of 2003. *MNRAS*, 344, 1000.

Calzetti, D., Armus, L., Bohlin, R. C., Kinney, A. L., Koornneef, J., and Storchi-Bergmann, T. (2000). The Dust Content and Opacity of Actively Star-forming Galaxies. *ApJ*, 533, 682.

Calzetti, D., Kennicutt, R. C., Engelbracht, C. W., Leitherer, C., Draine, B. T., Kewley, L., Moustakas, J., Sosey, M., Dale, D. A., Gordon, K. D., Helou, G. X., Hollenbach, D. J., Armus, L., Bendo, G., Bot, C., Buckalew, B., Jarrett, T., Li, A., Meyer, M., Murphy, E. J., Prescott, M., Regan, M. W., Rieke, G. H., Roussel, H., Sheth, K., Smith, J. D. T., Thornley, M. D., and Walter, F. (2007). The Calibration of Mid-Infrared Star Formation Rate Indicators. *ApJ*, 666, 870.

Calzetti, D., Kennicutt, Jr. R. C., Bianchi, L., Thilker, D. A., Dale, D. A., Engelbracht, C. W., Leitherer, C., Meyer, M. J., Sosey, M. L., Mutchler, M., Regan, M. W., Thornley, M. D., Armus, L., Bendo, G. J., Boissier, S., Boselli, A., Draine, B. T., Gordon, K. D., Helou, G., Hollenbach, D. J., Kewley, L., Madore, B. F., Martin, D. C., Murphy, E. J., Rieke, G. H., Rieke, M. J., Roussel, H., Sheth, K., Smith, J. D., Walter, F., White, B. A., Yi, S., Scoville, N. Z., Polletta, M., and Lindler, D. (2005). Star Formation in NGC 5194 (M51a): The Panchromatic View from GALEX to Spitzer. *ApJ*, 633, 871.

Calzetti, D., Lee, J. C., Sabbi, E., Adamo, A., Smith, L. J., Andrews, J. E., Ubeda, L., Bright, S. N., Thilker, D., Aloisi, A., Brown, T. M., Chandar, R., Christian, C., Cignoni, M., Clayton, G. C., da Silva, R., de Mink, S. E., Dobbs, C., Elmegreen, B. G., Elmegreen, D. M., Evans, A. S., Fumagalli, M., Gallagher, III, J. S., Gouliermis, D. A., Grebel, E. K., Herrero, A., Hunter, D. A., Johnson, K. E., Kennicutt, R. C., Kim, H., Krumholz, M. R., Lennon, D., Levay, K., Martin, C., Nair, P., Nota, A., Östlin, G., Pellerin, A., Prieto, J., Regan, M. W., Ryon, J. E., Schaerer, D., Schiminovich, D., Tosi, M., Van Dyk, S. D., Walterbos, R., Whitmore, B. C., and Wofford, A. (2015). Legacy Extragalactic UV Survey (LEGUS) With the Hubble Space Telescope. I. Survey Description. *AJ*, 149, 51.

Cappellari, M. and Copin, Y. (2003). Adaptive spatial binning of integral-field spectroscopic data using Voronoi tessellations. *MNRAS*, 342, 345.

Cardelli, J. A., Clayton, G. C., and Mathis, J. S. (1989). The relationship between infrared, optical, and ultraviolet extinction. *ApJ*, 345, 245.

Carlberg, R. G. and Freedman, W. L. (1985). Dissipative models of spiral galaxies. *ApJ*, 298, 486.

Carroll, B. W. and Ostlie, D. A. (2006). *An introduction to modern astrophysics and cosmology*.

Chabrier, G. (2003). Galactic Stellar and Substellar Initial Mass Function. *PASP*, 115, 763.

Chandar, R., Chien, L.-H., Meidt, S., Querejeta, M., Dobbs, C., Schinnerer, E., Whitmore, B. C., Calzetti, D., Dinino, D., Kennicutt, R. C., and Regan, M. (2017). Clues to the Formation of Spiral Structure in M51 from the Ages and Locations of Star Clusters. *ApJ*, 845, 78.

Chandar, R., Whitmore, B. C., Dinino, D., Kennicutt, R. C., Chien, L.-H., Schinnerer, E., and Meidt, S. (2016). The Age, Mass, and Size Distributions of Star Clusters in M51. *ApJ*, 824, 71.

Chapman, N. L., Mundy, L. G., Lai, S.-P., and Evans, II, N. J. (2009). The Mid-Infrared Extinction Law in the Ophiuchus, Perseus, and Serpens Molecular Clouds. *ApJ*, 690, 496.

Charlot, S. and Fall, S. M. (2000). A Simple Model for the Absorption of Starlight by Dust in Galaxies. *ApJ*, 539, 718.

Chung, A., Koribalski, B., Bureau, M., and van Gorkom, J. H. (2006). Origin of the counterrotating gas in NGC 1596. *MNRAS*, 370, 1565.

Chung, A., van Gorkom, J. H., Kenney, J. D. P., and Vollmer, B. (2007). Virgo Galaxies with Long One-sided H I Tails. *ApJL*, 659, L115.

Cole, S., Lacey, C. G., Baugh, C. M., and Frenk, C. S. (2000). Hierarchical galaxy formation. *MNRAS*, 319, 168.

Combes, F. and Becquaert, J.-F. (1997). Vertical equilibrium of molecular gas in galaxies. *A&A*, 326, 554.

Combes, F., García-Burillo, S., Casasola, V., Hunt, L. K., Krips, M., Baker, A. J., Boone, F., Eckart, A., Marquez, I., Neri, R., Schinnerer, E., and Tacconi, L. J. (2014). ALMA reveals the feeding of the Seyfert 1 nucleus in NGC 1566. *A&A*, 565, A97.

Contopoulos, G. and Papayannopoulos, T. (1980). Orbits in weak and strong bars. *A&A*, 92, 33.

Cornett, R. H., O'Connell, R. W., Greason, M. R., Offenberg, J. D., Angione, R. J., Bohlin, R. C., Cheng, K. P., Roberts, M. S., Smith, A. M., Smith, E. P., Talbert, F. D., and Stecher, T. P. (1994). UIT: Ultraviolet surface photometry of the spiral galaxy M74 (NGC 628). *ApJ*, 426, 553.

da Cunha, E., Charlot, S., and Elbaz, D. (2008). A simple model to interpret the ultraviolet, optical and infrared emission from galaxies. *MNRAS*, 388, 1595.

da Cunha, E., Charmandaris, V., Díaz-Santos, T., Armus, L., Marshall, J. A., and Elbaz, D. (2010). Exploring the physical properties of local star-forming ULIRGs from the ultraviolet to the infrared. *A&A*, 523, A78.

da Silva, R. L., Fumagalli, M., and Krumholz, M. (2012). SLUGStochastically Lighting Up Galaxies. I. Methods and Validating Tests. *ApJ*, 745, 145.

Dale, D. A., Cohen, S. A., Johnson, L. C., Schuster, M. D., Calzetti, D., Engelbracht, C. W., Gil de Paz, A., Kennicutt, R. C., Lee, J. C., Begum, A., Block, M., Dalcanton, J. J., Funes, J. G., Gordon, K. D., Johnson, B. D., Marble, A. R., Sakai, S., Skillman, E. D., van Zee, L., Walter, F., Weisz, D. R., Williams, B., Wu, S.-Y., and Wu, Y. (2009). The Spitzer Local Volume Legacy: Survey Description and Infrared Photometry. *ApJ*, 703, 517.

Dale, D. A., Gil de Paz, A., Gordon, K. D., Hanson, H. M., Armus, L., Bendo, G. J., Bianchi, L., Block, M., Boissier, S., Boselli, A., Buckalew, B. A., Buat, V., Burgarella, D., Calzetti, D., Cannon, J. M., Engelbracht, C. W., Helou, G., Hollenbach, D. J., Jarrett, T. H., Kennicutt, R. C., Leitherer, C., Li, A., Madore, B. F., Martin, D. C., Meyer, M. J., Murphy, E. J., Regan, M. W., Roussel, H., Smith, J. D. T., Sosey, M. L., Thilker, D. A., and Walter, F. (2007). An Ultraviolet-to-Radio Broadband Spectral Atlas of Nearby Galaxies. *ApJ*, 655, 863.

Davé, R. (2008). The galaxy stellar mass-star formation rate relation: evidence for an evolving stellar initial mass function? *MNRAS*, 385, 147.

Davies, L. J. M., Robotham, A. S. G., Driver, S. P., Alpaslan, M., Baldry, I. K., Bland-Hawthorn, J., Brough, S., Brown, M. J. I., Cluver, M. E., Drinkwater, M. J., Foster, C., Grootes, M. W., Konstantopoulos, I. S., Lara-López, M. A., López-Sánchez, Á. R., Loveday, J., Meyer, M. J., Moffett, A. J., Norberg, P., Owers, M. S., Popescu, C. C., De Propris, R., Sharp, R., Tuffs, R. J., Wang, L., Wilkins, S. M., Dunne, L., Bourne, N., and Smith, M. W. L. (2015). Galaxy And Mass Assembly (GAMA): the effect of close interactions on star formation in galaxies. *MNRAS*, 452, 616.

de Blok, W. J. G., Keating, K. M., Pisano, D. J., Fraternali, F., Walter, F., Oosterloo, T., Brinks, E., Bigiel, F., and Leroy, A. (2014). A low H I column density filament in NGC 2403: signature of interaction or accretion. *A&A*, 569, A68.

de Vaucouleurs, G. (1959). Classification and Morphology of External Galaxies. *Handbuch der Physik*, 53, 275.

Dénes, H., Kilborn, V. A., Koribalski, B. S., and Wong, O. I. (2016). H I-deficient galaxies in intermediate-density environments. *MNRAS*, 455, 1294.

Di Matteo, P., Combes, F., Melchior, A.-L., and Semelin, B. (2007). Star formation efficiency in galaxy interactions and mergers: a statistical study. *A&A*, 468, 61.

Dobbs, C. and Baba, J. (2014). Dawes Review 4: Spiral Structures in Disc Galaxies. *PASA*, 31, e035.

Dobbs, C. L., Adamo, A., Few, C. G., Calzetti, D., Dale, D. A., Elmegreen, B. G., Evans, A. S., Gouliermis, D. A., Grasha, K., Grebel, E. K., Johnson, K. E., Kim, H., Lee, J. C., Messa, M., Ryon, J. E., Smith, L. J., Thilker, D., Ubeda, L., and Whitmore, B. (2017). The properties, origin and evolution of stellar clusters in galaxy simulations and observations. *MNRAS*, 464, 3580.

Dobbs, C. L. and Pringle, J. E. (2010). Age distributions of star clusters in spiral and barred galaxies as a test for theories of spiral structure. *MNRAS*, 409, 396.

Dobbs, C. L., Theis, C., Pringle, J. E., and Bate, M. R. (2010). Simulations of the grand design galaxy M51: a case study for analysing tidally induced spiral structure. *MNRAS*, 403, 625.

D'Onghia, E. (2015). Disk-stability Constraints on the Number of Arms in Spiral Galaxies. *ApJL*, 808, L8.

D'Onghia, E., Madau, P., Vera-Ciro, C., Quillen, A., and Hernquist, L. (2016). Excitation of Coupled Stellar Motions in the Galactic Disk by Orbiting Satellites. *ApJ*, 823, 4.

D'Onghia, E., Vogelsberger, M., and Hernquist, L. (2013). Self-perpetuating Spiral Arms in Disk Galaxies. *ApJ*, 766, 34.

Driver, S. P., Robotham, A. S. G., Bland-Hawthorn, J., Brown, M., Hopkins, A., Liske, J., Phillipps, S., and Wilkins, S. (2013). Two-phase galaxy evolution: the cosmic star formation histories of spheroids and discs. *MNRAS*, 430, 2622.

Dupuy, J. L., Heitsch, F., and Cecil, G. (2019). Lopsided gas discs arising from mass inflow in barred spiral galaxies. *MNRAS*, 486, 2020.

Durbala, A., Buta, R., Sulentic, J. W., and Verdes-Montenegro, L. (2009). Fourier photometric analysis of isolated galaxies in the context of the AMIGA project. *MNRAS*, 397, 1756.

Dutton, A. A. and van den Bosch, F. C. (2009). The impact of feedback on disc galaxy scaling relations. *MNRAS*, 396, 141.

Efremov, Y. N. (1995). Star Complexes and Associations: Fundamental and Elementary Cells of Star Formation. *AJ*, 110, 2757.

Efremov, Y. N. and Elmegreen, B. G. (1998). Hierarchical star formation from the time-space distribution of star clusters in the Large Magellanic Cloud. *MNRAS*, 299, 588.

Efthymiopoulos, C., Kyziropoulos, P. E., Páez, R. I., Zouloumi, K., and Gravvanis, G. A. (2019). Manifold spirals, disc-halo interactions, and the secular evolution in N-body models of barred galaxies. *MNRAS*, 484, 1487.

Egusa, F., Kohno, K., Sofue, Y., Nakanishi, H., and Komugi, S. (2009). Determining Star Formation Timescale and Pattern Speed in Nearby Spiral Galaxies. *ApJ*, 697, 1870.

Egusa, F., Mentuch Cooper, E., Koda, J., and Baba, J. (2017). Gas and stellar spiral arms and their offsets in the grand-design spiral galaxy M51. *MNRAS*, 465, 460.

Elagali, A., Staveley-Smith, L., Rhee, J., Wong, O. I., Bosma, A., Westmeier, T., Koribalski, B. S., Heald, G., For, B.-Q., Kleiner, D., Lee-Waddell, K., Madrid, J. P., Popping, A., Reynolds, T. N., Meyer, M. J., Allison, J. R., Lagos, C. D. P., Voronkov, M. A., Serra, P., Shao, L., Wang, J., Anderson, C. S., Bunton, J. D., Bekiaris, G., Walsh, W. M., Kilborn, V. A., Kamphuis, P., and Oh, S.-H. (2019). WALLABY early science - III. An H I study of the spiral galaxy NGC 1566. *MNRAS*, 487, 2797.

Elmegreen, B. G. (2011). Gravitational Instabilities in Two-component Galaxy Disks with Gas Dissipation. *ApJ*, 737, 10.

Elmegreen, B. G. and Elmegreen, D. M. (1986). Do density waves trigger star formation? *ApJ*, 311, 554.

Elmegreen, D. M. and Elmegreen, B. G. (1982). Flocculent and grand design spiral structure in field, binary and group galaxies. *MNRAS*, 201, 1021.

Elmegreen, D. M. and Elmegreen, B. G. (1987). Arm classifications for spiral galaxies. *ApJ*, 314, 3.

Elmegreen, D. M., Elmegreen, B. G., Erroz-Ferrer, S., Knapen, J. H., Teich, Y., Popinchalk, M., Athanassoula, E., Bosma, A., Comerón, S., Efremov, Y. N., Gadotti, D. A., Gil de Paz, A., Hinz, J. L., Ho, L. C., Holwerda, B., Kim, T., Laine, J., Laurikainen, E., Menéndez-Delmestre, K., Mizusawa, T., Muñoz-Mateos, J.-C., Regan, M. W., Salo, H., Seibert, M., and Sheth, K. (2014). Embedded Star Formation in S^4G Galaxy Dust Lanes. *ApJ*,

780, 32.

Elmegreen, D. M., Elmegreen, B. G., Yau, A., Athanassoula, E., Bosma, A., Buta, R. J., Helou, G., Ho, L. C., Gadotti, D. A., Knapen, J. H., Laurikainen, E., Madore, B. F., Masters, K. L., Meidt, S. E., Menéndez-Delmestre, K., Regan, M. W., Salo, H., Sheth, K., Zaritsky, D., Aravena, M., Skibba, R., Hinz, J. L., Laine, J., Gil de Paz, A., Muñoz-Mateos, J.-C., Seibert, M., Mizusawa, T., Kim, T., and Erroz Ferrer, S. (2011). Grand Design and Flocculent Spirals in the Spitzer Survey of Stellar Structure in Galaxies (S^4G). *ApJ*, 737, 32.

Elmegreen, D. M., Sundin, M., Elmegreen, B., and Sundelius, B. (1991). Properties and simulations of interacting spiral galaxies with transient 'ocular' shapes. *A&A*, 244, 52.

Fall, S. M. (2004). Mass, Age, and Space Distributions of Star Clusters. In Lamers, H. J. G. L. M., Smith, L. J., and Nota, A., editors, *The Formation and Evolution of Massive Young Star Clusters*, volume 322 of *Astronomical Society of the Pacific Conference Series*, page 399.

Fazio, G. G., Hora, J. L., Allen, L. E., Ashby, M. L. N., Barmby, P., Deutsch, L. K., Huang, J.-S., Kleiner, S., Marengo, M., Megeath, S. T., Melnick, G. J., Pahre, M. A., Patten, B. M., Polizotti, J., Smith, H. A., Taylor, R. S., Wang, Z., Willner, S. P., Hoffmann, W. F., Pipher, J. L., Forrest, W. J., McMurty, C. W., McCreight, C. R., McKelvey, M. E., McMurray, R. E., Koch, D. G., Moseley, S. H., Arendt, R. G., Mentzell, J. E., Marx, C. T., Losch, P., Mayman, P., Eichhorn, W., Krebs, D., Jhabvala, M., Gezari, D. Y., Fixsen, D. J., Flores, J., Shakoorzadeh, K., Jungo, R., Hakun, C., Workman, L., Karpati, G., Kichak, R., Whitley, R., Mann, S., Tollestrup, E. V., Eisenhardt, P., Stern, D., Gorjian, V., Bhattacharya, B., Carey, S., Nelson, B. O., Glaccum, W. J., Lacy, M., Lowrance, P. J., Laine, S., Reach, W. T., Stauffer, J. A., Surace, J. A., Wilson, G., Wright, E. L., Hoffman, A., Domingo, G., and Cohen, M. (2004). The Infrared Array Camera (IRAC) for the Spitzer Space Telescope. *ApJS*, 154, 10.

Ferreras, I., Cropper, M., Kawata, D., Page, M., and Hoversten, E. A. (2012). The Swift/UVOT catalogue of NGC 4321 star-forming sources: a case against density wave theory. *MNRAS*, 424, 1636.

Foyle, K., Rix, H.-W., Dobbs, C. L., Leroy, A. K., and Walter, F. (2011). Observational Evidence Against Long-lived Spiral Arms in Galaxies. *ApJ*, 735, 101.

Freeland, E., Sengupta, C., and Croston, J. H. (2010). Quantifying the importance of ram-pressure stripping in a galaxy group at 100 Mpc. *MNRAS*, 409, 1518.

Fujii, M. S., Baba, J., Saitoh, T. R., Makino, J., Kokubo, E., and Wada, K. (2011). The Dynamics of Spiral Arms in Pure Stellar Disks. *ApJ*, 730, 109.

Fux, R. (1997). 3D self-consistent N-body barred models of the Milky Way. I. Stellar dynamics. *A&A*, 327, 983.

García-Benito, R., González Delgado, R. M., Pérez, E., Cid Fernandes, R., Cortijo-Ferrero, C., López Fernández, R., de Amorim, A. L., Lacerda, E. A. D., Vale Asari, N., and Sánchez, S. F. (2017). The spatially resolved star formation history of CALIFA galaxies. Cosmic time scales. *A&A*, 608, A27.

Gauthier, J.-R., Dubinski, J., and Widrow, L. M. (2006). Substructure around M31: Evolution and Effects. *ApJ*, 653, 1180.

Goddard, Q. E., Bastian, N., and Kennicutt, R. C. (2010). On the fraction of star clusters surviving the embedded phase. *MNRAS*, 405, 857.

Goldreich, P. and Lynden-Bell, D. (1965). II. Spiral arms as sheared gravitational instabilities. *MNRAS*, 130, 125.

Goldreich, P. and Tremaine, S. (1978). The excitation and evolution of density waves. *ApJ*, 222, 850.

Gomes, J. M., Papaderos, P., Vílchez, J. M., Kehrig, C., Iglesias-Páramo, J., Breda, I., Lehnert, M. D., Sánchez, S. F., Ziegler, B., Dos Reis, S. N., Bland-Hawthorn, J., Galbany, L., Bomans, D. J., Rosales-Ortega, F. F., Walcher, C. J., García-Benito, R., Márquez, I., Del Olmo, A., Mollá, M., Marino, R. A., Catalán-Torrecilla, C., González Delgado, R. M., López-Sánchez, Á. R., and Califa Collaboration (2016). Spectroscopic aperture biases in inside-out evolving early-type galaxies from CALIFA. *A&A*, 586, A22.

Gouliermis, D. A., Elmegreen, B. G., Elmegreen, D. M., Calzetti, D., Cignoni, M., Gallagher, III, J. S., Kennicutt, R. C., Klessen, R. S., Sabbi, E., Thilker, D., Ubeda, L., Aloisi, A., Adamo, A., Cook, D. O., Dale, D., Grasha, K., Grebel, E. K., Johnson, K. E., Sacchi, E., Shabani, F., Smith, L. J., and Wofford, A. (2017). Hierarchical star formation across the grand-design spiral NGC 1566. *MNRAS*, 468, 509.

Gouliermis, D. A., Thilker, D., Elmegreen, B. G., Elmegreen, D. M., Calzetti, D., Lee, J. C., Adamo, A., Aloisi, A., Cignoni, M., Cook, D. O., Dale, D. A., Gallagher, J. S., Grasha, K., Grebel, E. K., Davó, A. H., Hunter, D. A., Johnson, K. E., Kim, H., Nair, P., Nota, A., Pellerin, A., Ryon, J., Sabbi, E., Sacchi, E., Smith, L. J., Tosi, M., Ubeda, L., and Whitmore, B. (2015). Hierarchical star formation across the ring galaxy NGC 6503. *MNRAS*, 452, 3508.

Grand, R. J. J., Kawata, D., and Cropper, M. (2012a). Dynamics of stars around spiral arms in an N-body/SPH simulated barred spiral galaxy. *MNRAS*, 426, 167.

Grand, R. J. J., Kawata, D., and Cropper, M. (2012b). The dynamics of stars around spiral arms. *MNRAS*, 421, 1529.

Grasha, K., Calzetti, D., Adamo, A., Kim, H., Elmegreen, B. G., Gouliermis, D. A., Aloisi, A., Bright, S. N., Christian, C., Cignoni, M., Dale, D. A., Dobbs, C., Elmegreen, D. M., Fumagalli, M., Gallagher, III, J. S., Grebel, E. K., Johnson, K. E., Lee, J. C., Messa, M., Smith, L. J., Ryon, J. E., Thilker, D., Ubeda, L., and Wofford, A. (2015). The Spatial Distribution of the Young Stellar Clusters in the Star-forming Galaxy NGC 628. *ApJ*, 815, 93.

Grasha, K., Calzetti, D., Adamo, A., Kim, H., Elmegreen, B. G., Gouliermis, D. A., Dale, D. A., Fumagalli, M., Grebel, E. K., Johnson, K. E., Kahre, L., Kennicutt, R. C., Messa, M., Pellerin, A., Ryon, J. E., Smith, L. J., Shabani, F., Thilker, D., and Ubeda, L. (2017a). The Hierarchical Distribution of the Young Stellar Clusters in Six Local Star-forming Galaxies. *ApJ*, 840, 113.

Grasha, K., Elmegreen, B. G., Calzetti, D., Adamo, A., Aloisi, A., Bright, S. N., Cook, D. O., Dale, D. A., Fumagalli, M., Gallagher, III, J. S., Gouliermis, D. A., Grebel, E. K., Kahre, L., Kim, H., Krumholz, M. R., Lee, J. C., Messa, M., Ryon, J. E., and Ubeda, L. (2017b). Hierarchical Star Formation in Turbulent Media: Evidence from Young Star Clusters. *ApJ*, 842, 25.

Grosbøl, P., Patsis, P. A., and Pompei, E. (2004). Spiral galaxies observed in the near-infrared K band. I. Data analysis and structural parameters. *A&A*, 423, 849.

Gunn, J. E. and Gott, III, J. R. (1972). On the Infall of Matter Into Clusters of Galaxies and Some Effects on Their Evolution. *ApJ*, 176, 1.

Haynes, M. P., Hogg, D. E., Maddalena, R. J., Roberts, M. S., and van Zee, L. (1998). Asymmetry in high-precision global H I profiles of isolated spiral galaxies. *AJ*, 115, 62.

Hayward, C. C. and Smith, D. J. B. (2015). Should we believe the results of ultraviolet-millimetre galaxy spectral energy distribution modelling? *MNRAS*, 446, 1512.

Heald, G., de Blok, W. J. G., Lucero, D., Carignan, C., Jarrett, T., Elson, E., Oozeer, N., Randriamampandry, T. H., and van Zee, L. (2016). Neutral hydrogen and magnetic fields in M83 observed with the SKA Pathfinder KAT-7. *MNRAS*, 462, 1238.

Helfer, T. T., Thornley, M. D., Regan, M. W., Wong, T., Sheth, K., Vogel, S. N., Blitz, L., and Bock, D. C.-J. (2003). The BIMA Survey of Nearby Galaxies (BIMA SONG). II. The CO Data. *ApJS*, 145, 259.

Hernquist, L. (1990). *Dynamical status of M51.*, pages 108–117.

Hernquist, L. and Quinn, P. J. (1989). Formation of shell galaxies. II - Nonspherical potentials. *ApJ*, 342, 1.

Howard, S. and Byrd, G. G. (1990). A self-gravitating simulation of the M51 system. *AJ*, 99, 1798.

Hubble, E. P. (1926). Extragalactic nebulae. *ApJ*, 64.

Hunt, L. K., De Looze, I., Boquien, M., Nikutta, R., Rossi, A., Bianchi, S., Dale, D. A., Granato, G. L., Kennicutt, R. C., Silva, L., Ciesla, L., Relaño, M., Viaene, S., Brandl, B., Calzetti, D., Croxall, K. V., Draine, B. T., Galametz,

M., Gordon, K. D., Groves, B. A., Helou, G., Herrera-Camus, R., Hinz, J. L., Koda, J., Salim, S., Sandstrom, K. M., Smith, J. D., Wilson, C. D., and Zibetti, S. (2019). Comprehensive comparison of models for spectral energy distributions from 0.1 μm to 1 mm of nearby star-forming galaxies. *A&A*, 621, A51.

Jarrett, T. H., Chester, T., Cutri, R., Schneider, S., Skrutskie, M., and Huchra, J. P. (2000). 2MASS Extended Source Catalog: Overview and Algorithms. *AJ*, 119, 2498.

Jog, C. J. (1997). Dynamics of Orbits and Local Gas Stability in a Lopsided Galaxy. *ApJ*, 488, 642.

Jog, C. J. (2002). Large-scale asymmetry of rotation curves in lopsided spiral galaxies. *A&A*, 391, 471.

Jog, C. J. and Combes, F. (2009). Lopsided spiral galaxies. *PhR*, 471, 75.

Johnson, B. D., Schiminovich, D., Seibert, M., Treyer, M., Martin, D. C., Barlow, T. A., Forster, K., Friedman, P. G., Morrissey, P., Neff, S. G., Small, T., Wyder, T. K., Bianchi, L., Donas, J., Heckman, T. M., Lee, Y.-W., Madore, B. F., Milliard, B., Rich, R. M., Szalay, A. S., Welsh, B. Y., and Yi, S. K. (2007). Ultraviolet through Infrared Spectral Energy Distributions from 1000 SDSS Galaxies: Dust Attenuation. *ApJS*, 173, 392.

Johnson, L. C., Seth, A. C., Dalcanton, J. J., Beerman, L. C., Fouesneau, M., Lewis, A. R., Weisz, D. R., Williams, B. F., Bell, E. F., Dolphin, A. E., Larsen, S. S., Sandstrom, K., and Skillman, E. D. (2016). Panchromatic Hubble Andromeda Treasury. XVI. Star Cluster Formation Efficiency and the Clustered Fraction of Young Stars. *ApJ*, 827, 33.

Julian, W. H. and Toomre, A. (1966). Non-Axisymmetric Responses of Differentially Rotating Disks of Stars. *ApJ*, 146, 810.

Kaleida, C. and Scowen, P. A. (2010). Mapping the Recent Star Formation History of the Disk of M51. *AJ*, 140, 379.

Kamphuis, J., Sancisi, R., and van der Hulst, T. (1991). An H I superbubble in the spiral galaxy M 101. *A&A*, 244, L29.

Kamphuis, J. J. (1993). PhD thesis, PhD Thesis, University of Groningen, (1993).

Keel, W. C., Kennicutt, Jr., R. C., Hummel, E., and van der Hulst, J. M. (1985). The effects of interactions on spiral galaxies. I - Nuclear activity and star formation. *AJ*, 90, 708.

Kendall, S., Kennicutt, R. C., and Clarke, C. (2011). Spiral structure in nearby galaxies - I. Sample, data analysis and overview of results. *MNRAS*, 414, 538.

Kennicutt, R. C., Roettiger, K. A., Keel, W. C., van der Hulst, J. M., and Hummel, E. (1987). Induced star formation in interacting galaxies. In Lonsdale Persson, C. J., editor, *NASA Conference Publication*, volume 2466 of *NASA Conference Publication*.

Kennicutt, Jr., R. C. (1998). Star Formation in Galaxies Along the Hubble Sequence. *ARA&A*, 36, 189.

Kennicutt, Jr., R. C., Calzetti, D., Walter, F., Helou, G., Hollenbach, D. J., Armus, L., Bendo, G., Dale, D. A., Draine, B. T., Engelbracht, C. W., Gordon, K. D., Prescott, M. K. M., Regan, M. W., Thornley, M. D., Bot, C., Brinks, E., de Blok, E., de Mello, D., Meyer, M., Moustakas, J., Murphy, E. J., Sheth, K., and Smith, J. D. T. (2007). Star Formation in NGC 5194 (M51a). II. The Spatially Resolved Star Formation Law. *ApJ*, 671, 333.

Kennicutt, Jr., R. C., Lee, J. C., Funes, J. G., J., S., Sakai, S., and Akiyama, S. (2008). An Hα Imaging Survey of Galaxies in the Local 11 Mpc Volume. *ApJS*, 178, 247.

Korchagin, V., Kikuchi, N., Miyama, S. M., Orlova, N., and Peterson, B. A. (2000). Global Spiral Modes in NGC 1566: Observations and Theory. *ApJ*, 541, 565.

Kormendy, J. and Norman, C. A. (1979). Observational constraints on driving mechanisms for spiral density waves. *ApJ*, 233, 539.

Kornreich, D. A., Haynes, M. P., and Lovelace, R. V. E. (1998). A Photometric Method for Quantifying Asymmetries in Disk Galaxies. *AJ*, 116, 2154.

Kroupa, P. (2001). On the variation of the initial mass function. *MNRAS*, 322, 231.

Krumholz, M. R., Adamo, A., Fumagalli, M., Wofford, A., Calzetti, D., Lee, J. C., Whitmore, B. C., Bright, S. N., Grasha, K., Gouliermis, D. A., Kim, H., Nair, P., Ryon, J. E., Smith, L. J., Thilker, D., Ubeda, L., and Zackrisson, E. (2015). Star Cluster Properties in Two LEGUS Galaxies Computed with Stochastic Stellar Population Synthesis Models. *ApJ*, 812, 147.

Lada, C. J. and Lada, E. A. (2003). Embedded Clusters in Molecular Clouds. *ARA&A*, 41, 57.

Landy, S. D. and Szalay, A. S. (1993). Bias and variance of angular correlation functions. *ApJ*, 412, 64.

Lee, J. C., Gil de Paz, A., Tremonti, C., Kennicutt, Jr., R. C., Salim, S., Bothwell, M., Calzetti, D., Dalcanton, J., Dale, D., Engelbracht, C., Funes, S. J. J. G., Johnson, B., Sakai, S., Skillman, E., van Zee, L., Walter, F., and Weisz, D. (2009). Comparison of Hα and UV Star Formation Rates in the Local Volume: Systematic Discrepancies for Dwarf Galaxies. *ApJ*, 706, 599.

Leitherer, C., Schaerer, D., Goldader, J. D., Delgado, R. M. G., Robert, C., Kune, D. F., de Mello, D. F., Devost, D., and Heckman, T. M. (1999). Starburst99: Synthesis Models for Galaxies with Active Star Formation. *ApJS*, 123, 3.

Leroy, A. K., Walter, F., Brinks, E., Bigiel, F., de Blok, W. J. G., Madore, B., and Thornley, M. D. (2008). The Star Formation Efficiency in Nearby Galaxies: Measuring Where Gas Forms Stars Effectively. *AJ*, 136, 2782.

Lianou, S., Barmby, P., Rémy-Ruyer, A., Madden, S. C., Galliano, F., and Lebouteiller, V. (2014). Probing the interstellar medium of NGC 1569 with Herschel. *MNRAS*, 445, 1003.

Lin, C. C. and Shu, F. H. (1964). On the Spiral Structure of Disk Galaxies. *ApJ*, 140, 646.

Lindblad, B. (1963). On the possibility of a quasi-stationary spiral structure in galaxies. *Stockholms Observatoriums Annaler*, 22.

Louie, M., Koda, J., and Egusa, F. (2013). Geometric Offsets across Spiral Arms in M51: Nature of Gas and Star Formation Tracers. *ApJ*, 763, 94.

Mapelli, M., Moore, B., and Bland-Hawthorn, J. (2008). Lopsided galaxies: the case of NGC 891. *MNRAS*, 388, 697.

Martínez-García, E. E. (2012). Testing Theories in Barred-spiral Galaxies. *ApJ*, 744, 92.

Martínez-García, E. E., González-López lira, R. A., and Bruzual-A, G. (2009). Spiral Density Wave Triggering of Star Formation in SA and SAB Galaxies. *ApJ*, 694, 512.

Matthews, L. D., van Driel, W., and Gallagher, III, J. S. (1998). High-Resolution, High Signal-to-Noise, Global H i Spectra of Southern, Extreme Late-Type Spiral Galaxies. *AJ*, 116, 1169.

McConnachie, A. W., Venn, K. A., Irwin, M. J., Young, L. M., and Geehan, J. J. (2007). Ram Pressure Stripping of an Isolated Local Group Dwarf Galaxy: Evidence for an Intragroup Medium. *ApJL*, 671, L33.

Messa, M., Adamo, A., Östlin, G., Calzetti, D., Grasha, K., Grebel, E. K., Shabani, F., Chandar, R., Dale, D. A., Dobbs, C. L., Elmegreen, B. G., Fumagalli, M., Gouliermis, D. A., Kim, H., Smith, L. J., Thilker, D. A., Tosi, M., Ubeda, L., Walterbos, R., Whitmore, B. C., Fedorenko, K., Mahadevan, S., Andrews, J. E., Bright, S. N., Cook, D. O., Kahre, L., Nair, P., Pellerin, A., Ryon, J. E., Ahmad, S. D., Beale, L. P., Brown, K., Clarkson, D. A., Guidarelli, G. C., Parziale, R., Turner, J., and Weber, M. (2018). The young star cluster population of M51 with LEGUS - I. A comprehensive study of cluster formation and evolution. *MNRAS*, 473, 996.

Michel-Dansac, L., Duc, P.-A., Bournaud, F., Cuillandre, J.-C., Emsellem, E., Oosterloo, T., Morganti, R., Serra, P., and Ibata, R. (2010). A Collisional Origin for the Leo Ring. *ApJL*, 717, L143.

Morrissey, P., Conrow, T., Barlow, T. A., Small, T., Seibert, M., Wyder, T. K., Budavári, T., Arnouts, S., Friedman, P. G., Forster, K., Martin, D. C., Neff, S. G., Schiminovich, D., Bianchi, L., Donas, J., Heckman, T. M., Lee, Y.-W., Madore, B. F., Milliard, B., Rich, R. M., Szalay, A. S., Welsh, B. Y., and Yi, S. K. (2007). The Calibration

and Data Products of GALEX. *ApJS*, 173, 682.

Odewahn, S. C. (1994). Properties of the Magellanic type spirals. 2: The frequency of companion galaxies. *AJ*, 107, 1320.

Oh, S. H., Kim, W.-T., Lee, H. M., and Kim, J. (2008). Physical Properties of Tidal Features in Interacting Disk Galaxies. *ApJ*, 683, 94.

Olivares E., F., Hamuy, M., Pignata, G., Maza, J., Bersten, M., Phillips, M. M., Suntzeff, N. B., Filippenko, A. V., Morrel, N. I., Kirshner, R. P., and Matheson, T. (2010). The Standardized Candle Method for Type II Plateau Supernovae. *ApJ*, 715, 833.

Pardy, S. A., D'Onghia, E., Athanassoula, E., Wilcots, E. M., and Sheth, K. (2016). Tidally Induced Offset Disks in Magellanic Spiral Galaxies. *ApJ*, 827, 149.

Peebles, P. J. E. (1980). Statistics of the distribution of galaxies. In Ehlers, J., Perry, J. J., and Walker, M., editors, *Ninth Texas Symposium on Relativistic Astrophysics*, volume 336 of *Annals of the New York Academy of Sciences*, pages 161–171.

Pérez-González, P. G., Kennicutt, Jr., R. C., Gordon, K. D., Misselt, K. A., Gil de Paz, A., Engelbracht, C. W., Rieke, G. H., Bendo, G. J., Bianchi, L., Boissier, S., Calzetti, D., Dale, D. A., Draine, B. T., Jarrett, T. H., Hollenbach, D., and Prescott, M. K. M. (2006). Ultraviolet through Far-Infrared Spatially Resolved Analysis of the Recent Star Formation in M81 (NGC 3031). *ApJ*, 648, 987.

Pettitt, A. R., Tasker, E. J., and Wadsley, J. W. (2016). Gas and stellar spiral structures in tidally perturbed disc galaxies. *MNRAS*, 458, 3990.

Pettitt, A. R., Tasker, E. J., Wadsley, J. W., Keller, B. W., and Benincasa, S. M. (2017). Star formation and ISM morphology in tidally induced spiral structures. *MNRAS*, 468, 4189.

Portegies Zwart, S. F., McMillan, S. L. W., and Gieles, M. (2010). Young Massive Star Clusters. *ARA&A*, 48, 431.

Pour-Imani, H., Kennefick, D., Kennefick, J., Davis, B. L., Shields, D. W., and Shameer Abdeen, M. (2016). Strong Evidence for the Density-wave Theory of Spiral Structure in Disk Galaxies. *ApJL*, 827, L2.

Quilis, V., Moore, B., and Bower, R. (2000). Gone with the Wind: The Origin of S0 Galaxies in Clusters. *Science*, 288, 1617.

Rand, R. J. (1995). Berkeley-Illinois-Maryland Array Observations of Molecular Spiral Structure in M100 (NGC 4321). *AJ*, 109, 2444.

Rautiainen, P. and Salo, H. (1999). Multiple pattern speeds in barred galaxies. I. Two-dimensional models. *A&A*, 348, 737.

Reichard, T. A., Heckman, T. M., Rudnick, G., Brinchmann, J., and Kauffmann, G. (2008). The Lopsidedness of Present-Day Galaxies: Results from the Sloan Digital Sky Survey. *ApJ*, 677, 186.

Relaño, M. and Kennicutt, Jr., R. C. (2009). Star Formation in Luminous H II Regions in M33. *ApJ*, 699, 1125.

Richter, O.-G. and Sancisi, R. (1994). Asymmetries in disk galaxies. How often? How strong? *A&A*, 290.

Rieke, G. H., Young, E. T., Engelbracht, C. W., Kelly, D. M., Low, F. J., Haller, E. E., Beeman, J. W., Gordon, K. D., Stansberry, J. A., Misselt, K. A., Cadien, J., Morrison, J. E., Rivlis, G., Latter, W. B., Noriega-Crespo, A., Padgett, D. L., Stapelfeldt, K. R., Hines, D. C., Egami, E., Muzerolle, J., Alonso-Herrero, A., Blaylock, M., Dole, H., Hinz, J. L., Le Floc'h, E., Papovich, C., Pérez-González, P. G., Smith, P. S., Su, K. Y. L., Bennett, L., Frayer, D. T., Henderson, D., Lu, N., Masci, F., Pesenson, M., Rebull, L., Rho, J., Keene, J., Stolovy, S., Wachter, S., Wheaton, W., Werner, M. W., and Richards, P. L. (2004). The Multiband Imaging Photometer for Spitzer (MIPS). *ApJS*, 154, 25.

Rix, H.-W. and Rieke, M. J. (1993). Tracing the Stellar Mass in M51. *ApJ*, 418, 123.

Rix, H.-W. and Zaritsky, D. (1995). Nonaxisymmetric Structures in the Stellar Disks of Galaxies. *ApJ*, 447, 82.

Roberts, W. W. (1969). Large-Scale Shock Formation in Spiral Galaxies and its Implications on Star Formation. *ApJ*, 158, 123.

Roca-Fàbrega, S., Valenzuela, O., Figueras, F., Romero-Gómez, M., Velázquez, H., Antoja, T., and Pichardo, B. (2013). On galaxy spiral arms' nature as revealed by rotation frequencies. *MNRAS*, 432, 2878.

Romero-Gómez, M., Athanassoula, E., Masdemont, J. J., and García-Gómez, C. (2007). The formation of spiral arms and rings in barred galaxies. *A&A*, 472, 63.

Romero-Gómez, M., Masdemont, J. J., Athanassoula, E., and García-Gómez, C. (2006). The origin of rR_1 ring structures in barred galaxies. *A&A*, 453, 39.

Rudnick, G. and Rix, H.-W. (1998). Lopsidedness in Early-Type Disk Galaxies. *AJ*, 116, 1163.

Rudnick, G., Rix, H.-W., and Kennicutt, Jr., R. C. (2000). Lopsided Galaxies, Weak Interactions, and Boosting the Star Formation Rate. *ApJ*, 538, 569.

Ruggiero, R. and Lima Neto, G. B. (2017). The fate of the gaseous discs of galaxies that fall into clusters. *MNRAS*, 468, 4107.

Sabbi, E., Calzetti, D., Ubeda, L., Adamo, A., Cignoni, M., Thilker, D., Aloisi, A., Elmegreen, B. G., Elmegreen, D. M., Gouliermis, D. A., Grebel, E. K., Messa, M., Smith, L. J., Tosi, M., Dolphin, A., Andrews, J. E., Ashworth, G., Bright, S. N., Brown, T. M., Chandar, R., Christian, C., Clayton, G. C., Cook, D. O., Dale, D. A., de Mink, S. E., Dobbs, C., Evans, A. S., Fumagalli, M., Gallagher, III, J. S., Grasha, K., Herrero, A., Hunter, D. A., Johnson, K. E., Kahre, L., Kennicutt, R. C., Kim, H., Krumholz, M. R., Lee, J. C., Lennon, D., Martin, C., Nair, P., Nota, A., Östlin, G., Pellerin, A., Prieto, J., Regan, M. W., Ryon, J. E., Sacchi, E., Schaerer, D., Schiminovich, D., Shabani, F., Van Dyk, S. D., Walterbos, R., Whitmore, B. C., and Wofford, A. (2018). The Resolved Stellar Populations in the LEGUS Galaxies1. *ApJS*, 235, 23.

Sakhibov, F. K. and Smirnov, M. A. (2004). Star Formation and the Kinematics of Gas in the Disk of NGC 628. *Astronomy Reports*, 48, 995.

Salim, S., Rich, R. M., Charlot, S., Brinchmann, J., Johnson, B. D., Schiminovich, D., Seibert, M., Mallery, R., Heckman, T. M., Forster, K., Friedman, P. G., Martin, D. C., Morrissey, P., Neff, S. G., Small, T., Wyder, T. K., Bianchi, L., Donas, J., Lee, Y.-W., Madore, B. F., Milliard, B., Szalay, A. S., Welsh, B. Y., and Yi, S. K. (2007). UV Star Formation Rates in the Local Universe. *ApJS*, 173, 267.

Salo, H. and Laurikainen, E. (2000a). N-body model for M51 - I. Multiple encounter versus single passage? *MNRAS*, 319, 377.

Salo, H. and Laurikainen, E. (2000b). N-body model for M51 - II. Inner structure. *MNRAS*, 319, 393.

Salo, H., Laurikainen, E., Buta, R., and Knapen, J. H. (2010). Bars do Drive Spiral Density Waves. *ApJL*, 715, L56.

Sánchez-Gil, M. C., Jones, D. H., Pérez, E., Bland-Hawthorn, J., Alfaro, E. J., and O'Byrne, J. (2011). Age patterns in a sample of spiral galaxies. *MNRAS*, 415, 753.

Sancisi, R., Fraternali, F., Oosterloo, T., and van der Hulst, T. (2008). Cold gas accretion in galaxies. *A&A Rv*, 15, 189.

Sanders, R. H. and Huntley, J. M. (1976). Gas response to oval distortions in disk galaxies. *ApJ*, 209, 53.

Scheepmaker, R. A., Lamers, H. J. G. L. M., Anders, P., and Larsen, S. S. (2009). The spatial distribution of star and cluster formation in M 51. *A&A*, 494, 81.

Schinnerer, E., Meidt, S. E., Colombo, D., Chandar, R., Dobbs, C. L., García-Burillo, S., Hughes, A., Leroy, A. K., Pety, J., Querejeta, M., Kramer, C., and Schuster, K. F. (2017). The PdBI Arcsecond Whirlpool Survey (PAWS): The Role of Spiral Arms in Cloud and Star Formation. *ApJ*, 836, 62.

Schlafly, E. F. and Finkbeiner, D. P. (2011). Measuring Reddening with Sloan Digital Sky Survey Stellar Spectra

and Recalibrating SFD. *ApJ*, 737, 103.

Schoenmakers, R. H. M., Franx, M., and de Zeeuw, P. T. (1997). Measuring non-axisymmetry in spiral galaxies. *MNRAS*, 292, 349.

Seigar, M. S. and James, P. A. (1998). The structure of spiral galaxies - II. Near-infrared properties of spiral arms. *MNRAS*, 299, 685.

Sellwood, J. A. (2011). The lifetimes of spiral patterns in disc galaxies. *MNRAS*, 410, 1637.

Sellwood, J. A. and Carlberg, R. G. (1984). Spiral instabilities provoked by accretion and star formation. *ApJ*, 282, 61.

Sellwood, J. A. and Sparke, L. S. (1988). Pattern speeds in barred spiral galaxies. *MNRAS*, 231, 25P.

Sengupta, C. and Balasubramanyam, R. (2006). HI content in galaxies in loose groups. *MNRAS*, 369, 360.

Sengupta, C., Balasubramanyam, R., and Dwarakanath, K. S. (2007). HI imaging of galaxies in X-ray bright groups. *MNRAS*, 378, 137.

Shabani, F., Grebel, E. K., Pasquali, A., D'Onghia, E., Gallagher, J. S., Adamo, A., Messa, M., Elmegreen, B. G., Dobbs, C., Gouliermis, D. A., Calzetti, D., Grasha, K., Elmegreen, D. M., Cignoni, M., Dale, D. A., Aloisi, A., Smith, L. J., Tosi, M., Thilker, D. A., Lee, J. C., Sabbi, E., Kim, H., and Pellerin, A. (2018). Search for star cluster age gradients across spiral arms of three LEGUS disc galaxies. *MNRAS*, 478.

Shabani, F., Pasquali, A., A., D., CalzettiD., Grebel, E. K., Gallagher, J. S., Adamo, A., Dale, D. A., Cook, D. O., Elmegreen, B. G., Elmegreen, D. M., Fumagalli, M., Gouliermis, D. A., Grasha, K., Cignoni, M., Tosi, M., Aloisi, A., Evans, A. S., Wofford, A., Sabbi, E., Johnson, K. E., Smith, L. J., and Messa, M. (2019). A Spatially-resolved, Multi-wavelength Study of the Spiral galaxy NGC 3344. *Submitted to MNRAS*.

Sheen, Y.-K., Smith, R., Jaffé, Y., Kim, M., Yi, S. K., Duc, P.-A., Nantais, J., Candlish, G., Demarco, R., and Treister, E. (2017). Discovery of Ram-pressure Stripped Gas around an Elliptical Galaxy in Abell 2670. *ApJL*, 840, L7.

Sheth, K., Regan, M., Hinz, J. L., Gil de Paz, A., Menéndez-Delmestre, K., Muñoz-Mateos, J.-C., Seibert, M., Kim, T., Laurikainen, E., Salo, H., Gadotti, D. A., Laine, J., Mizusawa, T., Armus, L., Athanassoula, E., Bosma, A., Buta, R. J., Capak, P., Jarrett, T. H., Elmegreen, D. M., Elmegreen, B. G., Knapen, J. H., Koda, J., Helou, G., Ho, L. C., Madore, B. F., Masters, K. L., Mobasher, B., Ogle, P., Peng, C. Y., Schinnerer, E., Surace, J. A., Zaritsky, D., Comerón, S., de Swardt, B., Meidt, S. E., Kasliwal, M., and Aravena, M. (2010). The Spitzer Survey of Stellar Structure in Galaxies (S4G). *PASP*, 122, 1397.

Shu, F. H. (2016). Six Decades of Spiral Density Wave Theory. *ARA&A*, 54, 667.

Smajić, S., Moser, L., Eckart, A., Busch, G., Combes, F., García-Burillo, S., Valencia-S., M., and Horrobin, M. (2015). The nuclear gas disk of NGC 1566 dissected by SINFONI and ALMA. *A&A*, 583, A104.

Smith, D. J. B., Dunne, L., da Cunha, E., Rowlands, K., Maddox, S. J., Gomez, H. L., Bonfield, D. G., Charlot, S., Driver, S. P., Popescu, C. C., Tuffs, R. J., Dunlop, J. S., Jarvis, M. J., Seymour, N., Symeonidis, M., Baes, M., Bourne, N., Clements, D. L., Cooray, A., De Zotti, G., Dye, S., Eales, S., Scott, D., Verma, A., van der Werf, P., Andrae, E., Auld, R., Buttiglione, S., Cava, A., Dariush, A., Fritz, J., Hopwood, R., Ibar, E., Ivison, R. J., Kelvin, L., Madore, B. F., Pohlen, M., Rigby, E. E., Robotham, A., Seibert, M., and Temi, P. (2012). Herschel-ATLAS: multi-wavelength SEDs and physical properties of 250 μm selected galaxies at z 0.5. *MNRAS*, 427, 703.

Smith, D. J. B. and Hayward, C. C. (2015). Deriving star formation histories from photometry using energy balance spectral energy distribution modelling. *MNRAS*, 453, 1597.

Smith, D. J. B. and Hayward, C. C. (2018). Panchromatic SED modelling of spatially resolved galaxies. *MNRAS*, 476, 1705.

Sofue, Y. (1996). The Most Completely Sampled Rotation Curves for Galaxies. *ApJ*, 458, 120.

Sofue, Y. (1997). Nuclear-to-Outer Rotation Curves of Galaxies in the CO and HI Lines. *PASJ*, 49, 17.

Sorba, R. and Sawicki, M. (2015). Missing stellar mass in SED fitting: spatially unresolved photometry can underestimate galaxy masses. *MNRAS*, 452, 235.

Sorba, R. and Sawicki, M. (2018). Spatially unresolved SED fitting can underestimate galaxy masses: a solution to the missing mass problem. *MNRAS*, 476, 1532.

Struck, C., Dobbs, C. L., and Hwang, J.-S. (2011). Slowly breaking waves: the longevity of tidally induced spiral structure. *MNRAS*, 414, 2498.

Swaters, R. A., Schoenmakers, R. H. M., Sancisi, R., and van Albada, T. S. (1999). Kinematically lopsided spiral galaxies. *MNRAS*, 304, 330.

Tamburro, D., Rix, H.-W., Walter, F., Brinks, E., de Blok, W. J. G., Kennicutt, R. C., and Mac Low, M.-M. (2008). Geometrically Derived Timescales for Star Formation in Spiral Galaxies. *AJ*, 136, 2872.

Temi, P., Brighenti, F., and Mathews, W. G. (2005). Mid-Infrared Emission from Elliptical Galaxies: Sensitivity to Stellar Age. *ApJL*, 635, L25.

Tonry, J. L., Dressler, A., Blakeslee, J. P., Ajhar, E. A., Fletcher, A. B., Luppino, G. A., Metzger, M. R., and Moore, C. B. (2001). The SBF Survey of Galaxy Distances. IV. SBF Magnitudes, Colors, and Distances. *ApJ*, 546, 681.

Toomre, A. (1981). What amplifies the spirals. In Fall, S. M. and Lynden-Bell, D., editors, *Structure and Evolution of Normal Galaxies*, pages 111–136.

Toomre, A. and Toomre, J. (1972). Galactic Bridges and Tails. *ApJ*, 178, 623.

Tsoutsis, P., Kalapotharakos, C., Efthymiopoulos, C., and Contopoulos, G. (2009). Invariant manifolds and the response of spiral arms in barred galaxies. *A&A*, 495, 743.

van den Bosch, F. C. (2002). The impact of cooling and feedback on disc galaxies. *MNRAS*, 332, 456.

van Eymeren, J., Jütte, E., Jog, C. J., Stein, Y., and Dettmar, R.-J. (2011). Lopsidedness in WHISP galaxies. II. Morphological lopsidedness. *A&A*, 530, A30.

Vázquez, G. A. and Leitherer, C. (2005). Optimization of Starburst99 for Intermediate-Age and Old Stellar Populations. *ApJ*, 621, 695.

Verdes-Montenegro, L., Bosma, A., and Athanassoula, E. (2000). A detailed study of the ringed galaxy NGC 3344. *A&A*, 356, 827.

Viaene, S., Baes, M., Bendo, G., Boquien, M., Boselli, A., Ciesla, L., Cortese, L., De Looze, I., Eales, S., Fritz, J., Karczewski, O. Ł., Madden, S., Smith, M. W. L., and Spinoglio, L. (2016). The bolometric and UV attenuation in normal spiral galaxies of the Herschel Reference Survey. *A&A*, 586, A13.

Viaene, S., Fritz, J., Baes, M., Bendo, G. J., Blommaert, J. A. D. L., Boquien, M., Boselli, A., Ciesla, L., Cortese, L., De Looze, I., Gear, W. K., Gentile, G., Hughes, T. M., Jarrett, T., Karczewski, O. Ł., Smith, M. W. L., Spinoglio, L., Tamm, A., Tempel, E., Thilker, D., and Verstappen, J. (2014). The Herschel Exploitation of Local Galaxy Andromeda (HELGA). IV. Dust scaling relations at sub-kpc resolution. *A&A*, 567, A71.

Vogel, S. N., Kulkarni, S. R., and Scoville, N. Z. (1988). Star formation in giant molecular associations synchronized by a spiral density wave. *Nature*, 334, 402.

Voglis, N., Tsoutsis, P., and Efthymiopoulos, C. (2006). Invariant manifolds, phase correlations of chaotic orbits and the spiral structure of galaxies. *MNRAS*, 373, 280.

Vollmer, B. (2009). A holistic view on ram pressure stripping in the Virgo cluster. The first complete model-based time sequence. *A&A*, 502, 427.

Vulcani, B., Poggianti, B. M., Jaffé, Y. L., Moretti, A., Fritz, J., Gullieuszik, M., Bettoni, D., Fasano, G., Tonnesen, S., and McGee, S. (2018). GASP - XII. The variety of physical processes occurring in a single galaxy group in formation. *MNRAS*, 480, 3152.

Wada, K., Baba, J., and Saitoh, T. R. (2011). Interplay between Stellar Spirals and the Interstellar Medium in Galactic Disks. *ApJ*, 735, 1.

Walker, I. R., Mihos, J. C., and Hernquist, L. (1996). Quantifying the Fragility of Galactic Disks in Minor Mergers. *ApJ*, 460, 121.

Weinberg, M. D. (1995). Production of Milky Way Structure by the Magellanic Clouds. *ApJL*, 455, L31.

Welikala, N., Connolly, A. J., Hopkins, A. M., Scranton, R., and Conti, A. (2008). Spatially Resolved Galaxy Star Formation and Its Environmental Dependence. I. *ApJ*, 677, 970.

Westmeier, T., Braun, R., and Koribalski, B. S. (2011). Gas and dark matter in the Sculptor group: NGC 300. *MNRAS*, 410, 2217.

White, D. A., Fabian, A. C., Forman, W., Jones, C., and Stern, C. (1991). Ram-pressure stripping of the multiphase interstellar medium of the Virgo cluster elliptical galaxy M86 (NGC 4406). *ApJ*, 375, 35.

Wilcots, E. M. and Prescott, M. K. M. (2004). H I Observations of Barred Magellanic Spirals. II. The Frequency and Impact of Companions. *AJ*, 127, 1900.

Williams, T. G., Gear, W. K., and Smith, M. W. L. (2018). The star formation law at GMC scales in M33, the Triangulum galaxy. *MNRAS*, 479, 297.

Wuyts, S., Förster Schreiber, N. M., Genzel, R., Guo, Y., Barro, G., Bell, E. F., Dekel, A., Faber, S. M., Ferguson, H. C., Giavalisco, M., Grogin, N. A., Hathi, N. P., Huang, K.-H., Kocevski, D. D., Koekemoer, A. M., Koo, D. C., Lotz, J., Lutz, D., McGrath, E., Newman, J. A., Rosario, D., Saintonge, A., Tacconi, L. J., Weiner, B. J., and van der Wel, A. (2012). Smooth(er) Stellar Mass Maps in CANDELS: Constraints on the Longevity of Clumps in High-redshift Star-forming Galaxies. *ApJ*, 753, 114.

Yoon, H., Chung, A., Smith, R., and Jaffé, Y. L. (2017). A History of H I Stripping in Virgo: A Phase-space View of VIVA Galaxies. *ApJ*, 838, 81.

Yozin, C. and Bekki, K. (2014). Tidal-induced lopsidedness in Magellanic-type galaxies. *MNRAS*, 439, 1948.

Zackrisson, E., Rydberg, C.-E., Schaerer, D., Östlin, G., and Tuli, M. (2011). The Spectral Evolution of the First Galaxies. I. James Webb Space Telescope Detection Limits and Color Criteria for Population III Galaxies. *ApJ*, 740, 13.

Zaritsky, D. and Rix, H.-W. (1997). Lopsided Spiral Galaxies and a Limit on the Galaxy Accretion Rate. *ApJ*, 477, 118.

Zaritsky, D., Salo, H., Laurikainen, E., Elmegreen, D., Athanassoula, E., Bosma, A., Comerón, S., Erroz-Ferrer, S., Elmegreen, B., Gadotti, D. A., Gil de Paz, A., Hinz, J. L., Ho, L. C., Holwerda, B. W., Kim, T., Knapen, J. H., Laine, J., Laine, S., Madore, B. F., Meidt, S., Menendez-Delmestre, K., Mizusawa, T., Muñoz-Mateos, J. C., Regan, M. W., Seibert, M., and Sheth, K. (2013). On the Origin of Lopsidedness in Galaxies as Determined from the Spitzer Survey of Stellar Structure in Galaxies (S^4G). *ApJ*, 772, 135.

Zibetti, S., Charlot, S., and Rix, H.-W. (2009). Resolved stellar mass maps of galaxies - I. Method and implications for global mass estimates. *MNRAS*, 400, 1181.

Zimmer, P., Rand, R. J., and McGraw, J. T. (2004). The Pattern Speeds of M51, M83, and NGC 6946 Using CO and the Tremaine-Weinberg Method. *ApJ*, 607, 285.